Advances in self-sensing techniques for atomic force microscopy

THÈSE N^{O} 6992 (2016)

PRÉSENTÉE LE 20 MAI 2016

À LA FACULTÉ DES SCIENCES ET TECHNIQUES DE L'INGÉNIEUR
LABORATOIRE DE BIO- ET NANO-INSTRUMENTATION
PROGRAMME DOCTORAL EN MICROSYSTÈMES ET MICROÉLECTRONIQUE

ÉCOLE POLYTECHNIQUE FÉDÉRALE DE LAUSANNE

POUR L'OBTENTION DU GRADE DE DOCTEUR ÈS SCIENCES

PAR

Maja ĐUKIĆ PJANIĆ

acceptée sur proposition du jury:

Prof. Ph. Renaud, président du jury
Prof. G. Fantner, directeur de thèse
Prof. E. M. Meyer, rapporteur
Dr C. H. Schwalb, rapporteur
Prof. J. Brugger, rapporteur

ÉCOLE POLYTECHNIQUE
FÉDÉRALE DE LAUSANNE

Suisse
2016

Ideas are easy. Implementation is hard.
Guy Kawasaki

To my parents ...

Acknowledgements

A journey towards this thesis started about five years ago with an internship. During those years many people have helped me come where I am today.

I would like to thank my advisor Georg Fantner for giving me an opportunity to work in his laboratory and perform my thesis research with him. He was always full of understanding, always stood by us, expecting a lot but giving much more. Thank you Georg for showing immense patience when needed, pushing us to achieve more than expected. The decision to come and join your laboratory was one of the best I ever made. It was a great pleasure working with you!

It was my great pleasure to have, as the members of my thesis committee, Professor Philippe Renaud, Professor Ernst Meyer, Dr. Christian Schwalb and Professor Professor Jürgen Brugger. I am thankful to them for accepting to be in my PhD defence committee and for taking the time to read my thesis.

I would like to thank Professor Michael Huth and his group from Frankfurt am Main University for one of the nicest research collaborations that I have had. Specially, I would like to thank Marcel Winhold and Christian Schwalb for always being there to patiently answer my NTR related questions. Big thanks I owe to Vladimir Stavrov and Vencislav Todorov for providing me with the necessary instrumentation and advice, their expertise and advice enabled many research performed in this thesis. I would also like to thank Ernest Fantner for calmly and wisely leading us through projects, though the worst and the best of times.

I would like to thank Professor Zoran Djuric for giving me an opportunity to come to Lausanne and for introducing me into the field of MEMS and NEMS. I would also like to thank my mentor Professor Vujo Drndarevic for his guidance during my bachelor and master thesis and for passing to me his love for area of measurement and sensors.

I would like to thank Dr. Jonathan Adams and Dr. Blake Erickson for taking me under their wing and teaching me everything from CAD design to running an AFM. They were like a mother and father to me, always having patience to explain things to me, even at my most stubborn *"Yes, but..."* moments.

I would like to thank all of my colleagues from LBNI for great time and collaboration during all these years: Adrian, Pascal, Nahid, Oliver, Farnaz, Chen, Joëlle, Mélanie, Santiago, Soma and Alex thank you!

Great thank you I owe to my parents for giving me such a great support and often so much more! My dad is still getting the calls starting with *"Oh Dad, I've got this problem..."* and his advice is always priceless. I would like to thank my mum for always supporting me and telling me I could achieve anything I want! Big sis Iva, thank you for always cheering for me, always being there for me and for facing your greatest fears for me!

I would also like to thank my brother in law Igor for giving me many good advice and for always asking the tricky questions, forcing me to rethink my research deeper. Big thanks I also owe to Nina and Dana for letting me stay at their home at the beginning of my stay in Lausanne and for treating me like their own child!

Of course big thanks goes to my Lausanne crew, always ready to lift up my mood! Thanks to Ana, Maja, Azra, Danica, Mira, Marija, Natasa, Bilja and Kristina for all the support, all the crazy girl moments and the greatest trips! Thanks Adrian for all the hospitality and great *Le Poulet du Vandredi* parties, thanks Vasic and Irena for inspiring me everyday, thanks Darko for all the philosophical debates, thanks to the entire physicist crew (Luka, Deki, Zlatko and Steva) and Kaća for being such great friends in my first days in Lausanne, those moments are unforgettable! Finally, big thanks to *The Uncotrollables* (Zlatko, Raca and Sean) who were nice to listen to me shout every Wednesday!

Finally, I would like to thank my husband Petar. He was my biggest support, believing in me and giving me strength when everything was going down hill. Thank you Petar for all those presentations that you listened, for all the papers you've read, for all the patience that you had, for rejoicing my successes more than yours. There is no one I would rather go through life with.

Abstract

Atomic force microscope (AFM) is a tool that allows micro and nano scale imaging of samples ranging from solid state physics to biology. AFM uses mechanical forces to sense the sample and recreate a topography image with high spatial resolution. The biggest disadvantage of the standard AFMs is their scanning speed, as it typically takes up to several tens of minutes to capture an image. A lot of research was conducted to increase AFM scanning speed, which resulted in the development of high-speed AFMs (HS-AFMs), that can obtain an image in matter of seconds. Such increase in scanning speed enabled the study of various processes, ranging from functional mechanisms of proteins to cellular biology dynamics. Increasing the speed further, towards several tens of images per second would highly benefit many applications, from both material and life sciences.

The imaging speed of an AFM is limited by the speed of its components. While scanners and electronic systems are constantly being improved, there exists a certain hold-up in the development of cantilevers and deflection sensing techniques. The mechanical bandwidth of the cantilever can be increased by decreasing its size. While it is possible to fabricate sub-micron sized cantilevers it becomes very challenging to sense their deflection. Standard AFMs rely on the optical beam deflection (OBD) readout, which can sense cantilevers down to 2 µm in width. Novel sensing techniques are needed to increase AFM imaging speed further. Strain-sensing techniques are particularly interesting as they offer many advantages over OBD readout, like the ability to sense sub-micron sized cantilevers.

We investigated nanogranular tunneling resistors (NTRs) as strain-sensors for cantilever deflection sensing. With NTR ability to be deposited on various substrates and in arbitrary geometries, with lateral dimensions down to tens of nm and having reasonably high gauge factors, they are an interesting candidate for cantilever deflection sensing. We applied NTRs in AFM imaging for the first time, showing that their sensitivity is well suited for imaging of both solid state and biological samples. We also demonstrated that NTRs can be used for sensing of 500 nm wide cantilevers.

We performed a study of doped Si piezoresistive strain sensors and of an unexploited potential which can be reached with the miniaturization of the cantilever dimensions. We demonstrated both theoretically and experimentally that by decreasing the size of the piezoresistive cantilevers, one can reach the AFM imaging noise performance equal or better than the noise performance of the OBD readout. We showed that piezoresistive cantilevers are very well suited for nm and Å scale imaging of both solid state and biological samples in air.

In addition, we performed a research on an advancement of the AFM feedback controller. Most AFMs use digital signal processor (DSP) based feedback controllers. Digital implementation of the controller has some disadvantages, as it necessitates data converters which introduce additional delays in the feedback loop. We developed a fast digitally controlled analog proportional-integral-derivative (PID) controller. We successfully used this PID controller in AFM imaging, realizing several hundreds of Hz line rates. While the analog implementation of the controller provided large amplification and frequency bandwidth, digital control provided precise control of the system and reproducibility of parameter values.

Keywords: atomic force microscopy (AFM), high-speed AFM, cantilevers, self-sensing, strain-sensing, nanogranular tunneling resistor, piezoresistor, minimum detectable deflection (MDD), proportional-integral-derivative (PID) controller

Zusammenfassung

Rasterkraftmikroskopie (AFM) ist ein bildgebendes Verfahren das Messungen im Mikro- bis Nanometerbereich von einer Vielzahl an Proben aus der Festkörperphysik bis hin zur Biologie machen kann. AFM basiert auf der Messung mechanischer Kräfte zur Rekonstruierung der Topograhie einer Probe mit hoher räumlicher Auflösung. Der grösste Nachteil handelsüblicher AFMs ist die Geschwindigkeit der Messung, oft dauert eine solche mehrere zehn Minuten. Langjährige Forschung zur Verschnellerung der Messung resultierten schlussendlich in der Entwicklung der Hochgeschwindigkeitsrasterkraftmikroskopie (HS-AFM), die es innert Sekunden ermöglicht ein Bild aufzunehmen. Diese Verbesserung der Aqusitionsgeschwindigkeit ermöglichte die Erforschung verschiedenster Prozesse vom funktionalen Mechanismus einzelner Proteine bis hin zu zellulärer Biodynamik. Eine weitere Verbesserung der Geschwindigkeit wäre von grossem Nutzen für verschiedenste Anwendungen der Materialwissenschaft und der Biowissenschaften.

Die Bildgebungsgeschwindigkeit eines AFMs ist limitiert durch die Geschwindigkeit einzelner Komponenten. Wärend die Nanopositionierer und die elektronischen Systeme kontinuierlich verbessert werden, existiert eine gewisse Verzögerung in der Entwicklung der Kraftmesssonden und den Techniken zu deren Auslesung. Die mechanische Bandbreite der Messsonden kann kann durch reduzierung deren Grösse gesteigert werden. Es ist zwar möglich Biegebalken kleiner als ein Mikrometer herzustellen, jedoch ist es zunehmend schwieriger deren Auslenkung auszulesen. Konventionelle AFM beruhen auf der Auslesung mittels Lichtzeigerprinzip (OBD), welches für Biegebalken bis 2 µm Breite geeignet ist. Neuartige Ausleseverfahren werden benötigt um die Bildgebungsgeschwindigkeit weiter zu erhöhen. Von besonderem Interesse sind Dehnungsmesstechniken, die eine Reihe von Vorteilen gegenüber Auslesung per Lichtzeigerprinzip haben, unter anderem die Möglichkeit, Biegebalken mit Dimensionen unter einem Mikrometer auszulesen.

Wir haben nanogranuläre Tunnelwiderstände (NTRs) als Dehnungsmesssensoren für Biegebalkenauslenkungsmessung untersucht. NTRs eignen sich zur Abschichtung auf

eine Vielzahl von Oberflächen in frei wählbaren Geometrien mit lateralen Dimensionen bis hin zu wenigen Zehn nanometern unter Beibehaltung vernünftig hoher Dehnungsfaktoren. Wir haben NTRs erstmalig zur Bildgebung in AFM eingesetzt und dabei gezeigt dass deren Sensitivität bestens geeignet ist um sowohl Festkörper als auch biologische Proben abzubilden. Ferner haben wir gezeigt, dass NTRs zum Auslesen von Biegebalken mit einer Breite von nur 500 nm verwendet werden können.

Wir haben zudem eine Studie zu piezoresistiven Dehnungsmesssensoren auf Basis von dotierten Silizium durchgeführt und deren ungenutztes Potential durch die Miniaturisierung der Biegebalkendimensionen gezeigt. Wir haben theoretisch und experimentell demonstriert, dass durch Verkleinerung der Grösse der piezoresistiven Biegebalken ein AFM Rauschverhalten erzieltwerden kann das gleichwertig oder besser ist als dasjenige der Auslesung mittels Lichtzeigerprinzip. Wir haben gezeigt, dass piezoresitive Biegebalken sehr gut geeignet sind für Bildgebung im nm und Å Bereich sowohl auf Festkörpern wie auch biologischen Proben an der Luft.

Weiterhin haben wir Forschung zur Verbesserung der Regelkreise für AFM getätigt. Die meisten AFM verwenden geschlossene Regelkreise die auf digitaler Signalverarbeitung (DSP) basieren. Die digitale Implementierung der Regler hat gewisse Nachteile, da die benötigten Datenwandlungen zusätzliche Verzögerungen in den Regelkreis einbringen. Wir haben einen schnellen, digital gesteuerten proportional-integral-derivative (PID) Regler entwickelt. Wir haben diesen PID Regler erfolgreich für Bildgebung mittels AFM verwendet, und dabei Zeilenraten von mehreren hundert Hertz erreicht. Wärend die analoge implementierung des Reglers die grosse Verstärkung und Frequenzbandbreite ermöglicht, erlaubt die digitale Ansteuerung die präzise Steuerung des Systems und hohe Wiederholgenauigkeit der Parameterwerte.

Schlüsselwörter: Rasterkraftmikroskopie (AFM), Hochgeschwindigkeitsrasterkraftmikroskopie, Biegebalken, Selbstauslesung, Dehnungsmessung, Nanogranuläte Tunnelwiderstände, Piezowiderstände, minimal detektierbare Auslenkung (MDD), proportional-integral-derivative (PID) Regler

Contents

Acknowledgements iii

Abstract v

Zusammenfassung vii

List of Abbreviations xix

1 Atomic Force Microscopy 1

1.1 Introduction 2

1.2 High-Speed Atomic Force Microscopy 3

1.3 Speed limiting factors 5

1.3.1 Cantilever sensor 5

1.3.2 Scanner 6

1.3.3 Electronics 7

1.4 Deflection readout of AFM cantilevers 8

1.4.1 Optical Beam Deflection method 8

1.4.2 Strain-sensing readout methods 10

1.4.3 Deflection readout of small-sized cantilevers 11

2 Nanogranular Tunneling Resistors in AFM 15

2.1 Introduction 16

2.2 NTR deposition process 17

2.3 NTR functional principal . . . 18
2.4 A feasibility analysis: the NTR readout for AFM . . . 19
2.4.1 NTR sensor dimensions . . . 20
2.4.2 NTR sensor resistance and gauge factor . . . 21
2.4.3 Influence of parasitic resistances on the SNR . . . 24
2.5 Self-sensing NTR cantilevers for AFM . . . 27
2.5.1 AFM measurement setup and procedure . . . 29
2.5.2 AFM imaging . . . 31
2.5.3 High-speed AFM imaging . . . 34
2.6 Deflection sensing of the 500 nm wide NTR cantilevers . . . 36
2.6.1 Fabrication of locally released NTR cantilevers . . . 36
2.6.2 Deflection measurements . . . 37
2.6.3 Apparent gauge factor . . . 38
2.7 Conclusion . . . 39

3 Doped silicon piezoresistors in AFM **41**

3.1 Introduction . . . 42
3.2 Noise sources and achievable MDD in AFM imaging . . . 43
3.2.1 MDD in OBD readout . . . 44
3.2.2 MDD in piezoresistive readout . . . 47
3.3 Noise measurement in AFM imaging . . . 49
3.4 Low-noise AFM imaging with piezoresistive readout . . . 51
3.5 Impact of the cantilever dimensions on MDD . . . 53
3.5.1 Estimated parameter values for MDD calculations . . . 53
3.5.2 Calculated MDDs and noise terms . . . 55
3.5.3 Dependence of the cantilever dimensions on the spring constant . . . 57
3.5.4 Estimation of dissipation power in OBD and piezoresistive readout 58

3.6 Conclusion 58

4 Analog PID controller for HS-AFM 61

4.1 Introduction 62

4.2 Implementation 63

4.2.1 Proportional part 65

4.2.2 Integral part 65

4.2.3 Derivative part 66

4.2.4 User interface implementation 67

4.3 Characterization 67

4.4 Imaging results 69

4.5 Conclusion 70

5 Conclusion 73

5.1 Why self-sensing techniques? 73

5.1.1 Beyond Si/SiN cantilevers 75

5.2 The return to the analog electronics 76

5.3 AFM: future outlook 77

5.3.1 Novel imaging techniques 77

5.3.2 The next generation of HS-AFM 78

5.3.3 Novel AFM applications 78

5.4 A closing note 79

Bibliography 81

A Appendix 97

A.1 Relation between angle and free end deflection 97

A.2 Where NTRs outperform optical detection 98

List of Tables

2.1 Parameters used for calculation of the expected SNR performance of thin gold film sensor versus NTR sensor 27

3.1 Estimated OBD readout parameters 54

3.2 Estimated piezoresistive readout parameters 54

A.1 Parameters used in calculation of the expected relative SNR performance of NTR sensors versus OBD detection 100

List of Figures

1.1 A schematic presentation of an AFM system 4

1.2 A schematic representation of the OBD measurement setup and principal 9

1.3 A schematic representation of several strain-sensing measurement setups . 10

1.4 A schematic representation of a strain-sensing measurement principal . . . 11

1.5 Optics approaches proposed for deflection sensing of small-sized cantilevers 13

2.1 An illustration of the NTR electron beam induced deposition process . . . 17

2.2 NTR strain-sensing functional principal 18

2.3 Scalability of the NTR sensor in thickness and width 21

2.4 Scalability of the NTR sensor in length 22

2.5 Signal-to-noise ratio optimization of NTR sensors 23

2.6 Influence of parasitic resistances on the SNR. 25

2.7 SNR loss in NTR and thin gold film readout due to parasitic resistances . 28

2.8 NTR sensors deposited on a variety of custom made AFM cantilevers . . . 29

2.9 The AFM measurement setup for large self-sensing cantilevers 30

2.10 The AFM measurement setup for small self-sensing cantilevers 31

2.11 AFM cantilever incorporating NTR active readout 32

2.12 Selected AFM images obtained with the self-sensing NTR cantilevers in air 33

2.13 Noise of NTR sensor in air and fluid 34

2.14 Imaging speed performance of NTR cantilevers 34

2.15 Cross sectional profile lines taken at the same y position, for different scanning speeds using NTR sensing readout 35

2.16 Mechanical bandwidth of the NTR AFM cantilever 36

2.17 The process flow for locally released NTR cantilevers 37

2.18 Deflection measurement setup for the smallest NTR cantilevers 37

2.19 Static deflection sensing of a 500 nm wide NTR cantilever 38

2.20 Gauge factor estimation of a small-sized NTR sensor 39

3.1 Effect of cantilever dimensions on the maximal bending angle and maximal strain induced in the cantilever. 42

3.2 The amplifier circuit seen by the RTI amplifier voltage noise 46

3.3 SEM images of $300 \times 100\,\mu m^2$ and $70 \times 30\,\mu m^2$ Si piezoresistive cantilevers 50

3.4 Noise measurements with OBD and piezoresistive readout 51

3.5 AFM images of biological and solid state samples obtained using piezoresistive readout. 52

3.6 Impact of the cantilever dimensions on MDD and noise terms, for both OBD and piezoresistive readout 56

3.7 Dependence of cantilever spring constant on the cantilever dimensions . . 57

3.8 Temperature distribution across $70 \times 30 \times 5\,\mu m^3$ sized silicon cantilever, for three different deflection readouts 58

4.1 PID controller gains realized in analog design using operational amplifiers. 64

4.2 A photo of the digitally controlled analog PID controller. 64

4.3 A schematic of the fine gain stage 65

4.4 Schematic of the PID controller and measured bandwidths of each coarse gain stage 66

4.5 The electrical bandwidth measurement of the PID controller 68

4.6 A closed-loop comparison between the analog PID and the commercial PID controller in cantilever surface tracking 69

4.7 AFM images of a silicon calibration grating obtained using the PID controller, at several 100s of Hz line rates 70

5.1 Cantilever development since the AFM discovery 74

5.2 Future in self0sensing cantilevers: trilayer polymer cantilevers 76

A.1 Parameter space of cantilever length and thickness comparing the SNR of optical and NTR deflection detection. 100

List of Abbreviations

AFM Atomic Force Microscopy

AM-AFM Amplitude Modulation - Atomic Force Microscopy

DAM-AFM Drive-Amplitude-Modulation - Atomic Force Microscopy

DNA Deoxyribonucleic Acid

DSP Digital Signal Processor

FEA Finite Element Analysis

FEBID Focused Electron Beam Induced Deposition

FIB Focused Ion Beam

FM-AFM Frequency Modulation - Atomic Force Microscopy

FPAA Field Programmable Analog Array

FPGA Field Programmable Gate Arrays

HOPG Highly Ordered Pyrolytic Graphite

HS-AFM High-Speed - Atomic Force Microscopy

MDD Minimum Detectable Deflection

NEMS Nanoelectromechanical Systems

NTR Nanogranular Tunneling Resistor

OBD Optical Beam Deflection

PALM Photo-Activated Localization Microscopy

PBS Phosphate Buffered Saline

PCB Printed Circuit Board

PF-QNM PeakForce Quantitative Nanoscale Mechanical

PFT PeakForce Tapping

PID Proportional-Integral-Derivative

PI Proportional-Integral

PLL Phase-Locked Loop

PM-AFM Phase Modulation - Atomic Force Microscopy

PSD Power Spectral Density

RTI Referred-To-Input

SEM Scanning Electron Microscopy

SEW Scattering Evanescent Wave

SNR Signal-to-Noise Ratio

SPI Serial Peripheral Interface

SPM Scanning Probe Microscopy

STM Scanning Tunneling Microscopy

STORM Stochastic Optical Reconstruction Microscopy

TEM Transmission Electron Microscopy

UHV Ultra High Vacuum

USB Universal Serial Bus

Chapter 1

Atomic Force Microscopy

A microscopy is *"...a technique that allows an examination of minute objects by means of an instrument which provides an enlarged image, not visible with the naked eye"* (a dictionary definition). In general, the term microscopy is mostly tied to the use of light and optical components such as lenses. However, invention of scanning electron microscopy (SEM) [1], transmission electron microscopy (TEM) [2] and atomic force microscopy (AFM) [3] provided alternative non-light based approaches for imaging of matter on the micrometer and nanometer scale.

To date, many excellent imaging tools are developed that allow obtaining detailed information about static structures of samples from various research areas such as physics, semiconductor industry, material sciences and life sciences. These tools can have accuracy down to atomic resolution. However, there are still very few tools that give us the opportunity to observe and understand how these structures change dynamically at the nanometer scale. This is particularly important for modern structural biology, where the structure and function of molecules and molecular assemblies are studied to understand the intricate processes of life.

Atomic force microscopy is a rare technique that gives us opportunity to inspect dynamics of processes on a micrometer and nanometer scale. While it can provide knowledge on molecular level it also enables real-time imaging of living matter such as cells and bacteria in their natural environment. AFM relies on mechanical (atomic) forces to reconstruct a sample image and it allows imaging in gas, liquid and vacuum environment. What distinguishes AFM from other microscopy techniques is that additionally to visualisation of a sample, AFM can also provide a lot of additional information about the sample such as height, stiffness, roughness, various electrical and magnetic properties etc.

Lateral resolution in AFM strongly depends on the sensing probe but can be down to 1 nm (typically few nanometers), while vertical resolution is typically less than 0.5 Å. In comparison, SEM has lateral resolution down to typically few nanometers but does not provide any height information, it is limited to a vacuum environment and it necessitates conductive contact with the sample and often metal coating of the poorly conducting samples. On the other hand, the highest resolution optical microscopy techniques ("super-resolution microscopy"), photo-activated localization microscopy (PALM) [4, 5] and stochastic optical reconstruction microscopy (STORM) [6] have lateral resolution on the order of few tens of nanometers and necessitate fluorescent dye staining of the sample.

However, temporal resolution is still a sore point of AFM. Standard commercial AFMs take on the order of few to few tens of minutes per image. However, in the recent years a branch of high-speed AFMs evolved, that can obtain up to several tens of images per second. Although, it is important to note that achievable AFM image rate strongly depends on the scan size. In comparison, super-resolution microscopy techniques, typically take several minutes per image, while SEM typically takes several seconds per image.

This chapter gives an explanation of the AFM functioning principle; it investigates the factors that limit the AFM imaging speed and gives an overview of HS-AFM field; it briefly explains common AFM probe sensing techniques and covers the state-of-the-art deflection readouts of small-sized probes that can no longer be sensed by the conventional techniques.

1.1 Introduction

Atomic force microscopes (AFM) belong to the class of scanning probe microscopes (SPM). Common to all scanning probe microscopes is that an image of a sample surface is obtained using a probe that scans the sample. The sample surface is line by line raster scanned with a probe and information about the sample surface is obtained by recording the probe-surface interaction as a function of the probe position. As a result, a three-dimensional surface profile of the sample is recorded. The first microscope in the SPM class was the scanning tunneling microscope (STM) [7] invented in 1981. This microscope obtains the sample image by measuring the tunneling current between the probe tip and the sample. Although it can scan samples with atomic resolution, STM can primarily be used for scanning of conductive samples.

In 1986 Binning, Quate and Gerber developed the first in a series of Atomic Force Microscopes [3]. This microscope could image both conductive and nonconductive samples with very high-resolution. In AFM, the sample is also scanned with a probe in the form of a small cantilever containing a sharp tip at its free end. As the sample is scanned, interatomic forces are acting between cantilever tip and the sample. These forces are causing bending of the cantilever which can be measured. By measuring the deflections of the cantilever, information about the sample surface can be reconstructed and the topography of the sample surface is imaged.

The development of AFM gave rise to an entire new family of microscopes. Besides topography, other sample characteristics that can be measured include electrical properties (conductance, capacitance, potential), magnetic properties, sample rigidity etc. with a resolution down to fractions of a nanometer. AFM allows for sample imaging in various surroundings: from standard ambient conditions to ultra high vacuum (UHV), liquid and gas environments, very low temperatures, etc. Also, in AFM no special treatment of the sample is needed. This allows for a wide application range, from semiconductor physics to the study of biological macromolecules and even living organisms.

AFM has numerous modes of operation [8,9]. Basic classification can be made depending on whether or not the cantilever is oscillating (dynamic mode and static mode) while the sample surface is scanned. In dynamic mode, depending on the parameter of the oscillation whose changes are used in tracking the surface, we distinguish Amplitude-Modulation AFM (AM-AFM, also known as the tapping mode) [10], Phase-Modulation AFM (PM-AFM) [11] or Frequency-Modulation AFM (FM-AFM) [12]. The most often used dynamic imaging mode is the so-called tapping mode in which the cantilever's tip is touching the sample surface only at its lowest point of oscillation. In this mode both amplitude or phase could be used for tracking.

1.2 High-Speed Atomic Force Microscopy

Despite many benefits and the widespread use of AFM, its imaging speed is still a limiting factor. Conventional AFMs typically take several minutes to several tens of minutes to obtain a high-quality image. The productivity and use of AFMs would increase dramatically if the speed could match the millisecond to minute imaging time of other scanning microscopes such as confocal and scanning electron microscopes. Moreover, many applications in materials science, life science and process control would benefit from AFMs with higher scan speeds [14, 15]. This is particularly important for modern structural

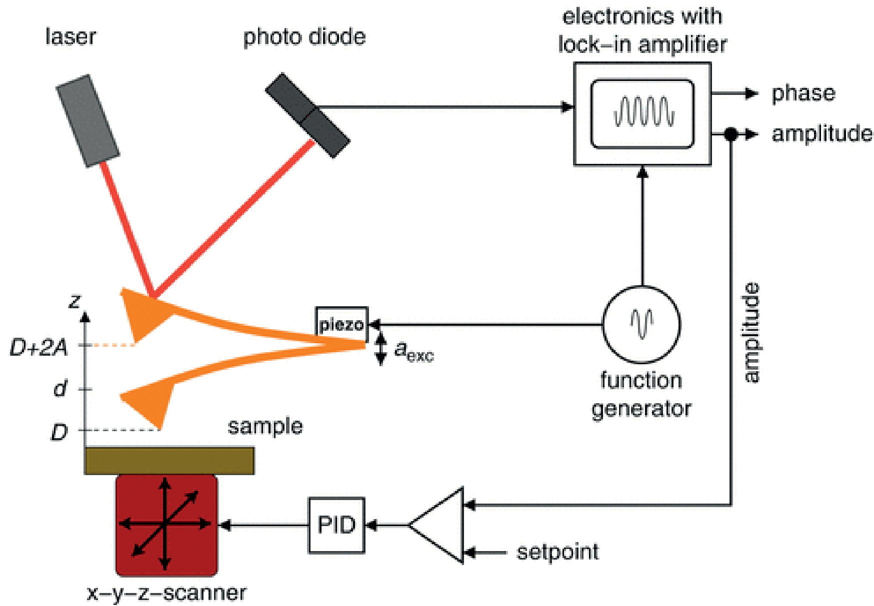

Figure 1.1: A schematic presentation of a tapping mode AFM system with optical beam deflection readout [13]

biology, where AFM is one of the few techniques that can image and probe biological samples in fluid with nanometer resolution to give information about the surface architecture, the localization and the interactions of individual constituents of cells. While knowing the static structure is essential, it is however often required to measure dynamic structural changes and measure living organisms in real time in order to understand the functioning of biological systems. New biocompatible, high-speed nanoscale characterization technologies are required to perform these measurements. To achieve this, the performance of many of the AFM components has to be increased.

Ando et al. pioneered HS-AFM imaging of various proteins down to molecular level, inspecting their underlaying functional mechanisms [16–26]. He focused on achieving high temporal resolution (down to sub-100 ms) at the expense of smaller scan size (in 10s and 100s of nanometers), devoting mainly to the study of the structural biology dynamics. Ando investigated dynamics of membrane proteins [17], protein self-assemblies [18, 24], peptide chains [16, 23], and dynamics of bacteriorhodopsin (bR) [20, 22, 25], F_1-ATPase [21] and myosin V [19].

Various other groups also performed structural biology studies by HS-AFM [27–29]. Casuso et al. imaged an interaction between the two membrane proteins [27]. Suzuki et al. used HS-AFM as auxiliary tool to investigate the dynamics of certain proteins involved in cell division [28]. Katan investigated the dynamics of deoxyribonucleic acid (DNA) molecules [29].

HS-AFM is also used in study of cellular biology dynamics. Fantner et al. was among the first to study cell processes with HS-AFM. He studied the effect of an antimicrobial peptide on the *Escherichia coli* cells [30], with nanometer lateral resolution which enabled inspecting the cell membrane in great detail. Imaging was performed with 13 s frame rate on the $3 \times 3\,\mu m$ area.

Several instruments combining various optical microscopy techniques and HS-AFM were recently developed for studying of cellular biology [31–34]. Combining optical microscopy with HS-AFM offers several advantages: precise optical identification of the area of interest for high resolution spatial and temporal HS-AFM imaging and correlation of structure and functioning of bacteria and cells.

Ando et al. recently also devoted to the inspection of bacteria and mammalian cell processes, by developing a wide area scanner [35] and specialized cantilever probes [36].

1.3 Speed limiting factors

To overcome the speed limitation of conventional AFM, a new generation of high-speed atomic force microscopes (HS-AFM) has been developed. Especially for AFM, as a mechanical system with electronic feedback, the imaging speed is limited by the mechanical and electrical bandwidths of each of the individual components such as the cantilever, the scanner and the feedback electronic components of the system [14, 15, 37, 38]. In a more detailed discussion about limitations of each of these components, only tapping mode operation will be considered as it is the most suitable mode for the observation of soft (biological) samples.

1.3.1 Cantilever sensor

The first limiting factor in HS-AFM is the speed of the local interaction between the tip and the sample. In this case the speed performance is limited by the performance of the sensor, i.e. the cantilever bandwidth. The bandwidth of the cantilever is determined by the factor

$$B = \pi f_0 / Q \tag{1.1}$$

where f_0 and Q are resonant frequency and quality factor of the cantilever, respectively. Therefore, higher resonant frequencies and lower Q factors result in a higher bandwidth of the cantilever. In imaging of soft samples it is desirable to have a low spring constant of

the cantilever, in order not to damage the sample while imaging. The first mode resonant frequency and the spring constant of the rectangular cantilever are defined by [39]:

$$f_0 = \frac{1.875^2}{2\pi}\frac{t}{l^2}\sqrt{\frac{E}{12\rho}} \quad (1.2)$$

$$k = \frac{wt^3}{4l^3}E \quad (1.3)$$

where t, w and l are the thickness, the width and the length of the cantilever, and E and ρ are the Young's modulus and the density of the cantilever material. The high f_0 and low k requirements can be met using small cantilevers. However, the smallest optically detectable cantilevers have the width of around 2 µm. While it is possible to fabricate cantilevers having much smaller dimensions, measuring the deflections of such cantilevers becomes very complex, as will be discussed later.

Using the current state-of-the-art small-sized cantilevers [40] one can reach close to video-rate imaging speeds on soft samples in media with inherently low Q factors (such as fluids) [19,21,30]. In comparison, achievable imaging speed in air is still lower due to the higher Q factor of the cantilever when oscillating in air and necessity for higher spring constant cantilevers, to avoid the problem of surface adhesion.

Another approach to increase the cantilever bandwidth and reach high scanning speeds in air, was demonstrated recently by Adams et al. [41]. Rather than just reducing the cantilever size to increase the f_0, he suggested to change the cantilever material and decrease the intrinsic cantilever Q factor, which can be achieved by using polymer cantilevers. This approach gave more than one order of magnitude higher cantilever bandwidth in air, while still maintaining similar spring constants as conventional cantilevers of alike size and resonance frequency.

1.3.2 Scanner

The second limiting factor in HS-AFM development is scanner speed in x, y and z axis. The limiting factor in this case is usually the low mechanical resonant frequency of the scanner system. Sending triangular shaped scan signals to the piezo actuators can excite the resonances of the scanner in all axes which affects the imaging process. Several approaches were demonstrated to avoid these issues such as scanning at the resonant frequency of the scanner [38] or designing a scanner with higher resonant frequencies [14, 37, 42]. Using resonant scanners has the disadvantage that the line rate of such scanners cannot be changed easily. On the other hand, designing a scanner with higher

resonant frequencies, which is directly related to the scan speed, usually comes at the cost of a smaller scan range. Therefore, it is hard to design a scanner that sufficiently satisfies both conditions. Work has also been done to develop model based filters in order to modify the signals sent to the scanner in such a way as not to excite its resonant frequencies [43]. To improve scanning in the z direction cantilevers with integrated piezo actuators were developed that could react much faster to height variations [44, 45]. However, this complicates the fabrication process of the cantilevers and as well, achieving the desired parameters of the cantilever becomes difficult or impossible.

Recently, a new AFM imaging technique, so called peak force tapping (PFT) [46] was published combining both direct force control while simultaneously avoiding lateral forces damage. In the PFT imaging, the z piezo is sinusoidally excited and the cantilever is brought in and out of contact with the surface, while the force interaction between the cantilever tip and the sample is continuously controlled. The main speed limiting factor in this technique represents the z piezo resonance, as the frequency of the z piezo modulation has to stay well below the scanner resonance [47].

1.3.3 Electronics

The bandwidth of every single electronic system of the AFM also limits the AFM imaging speed. In the feedback loop, firstly a cantilever deflection needs to be measured. In tapping mode it is also necessary to extract the information about the amplitude change and error signal needs to be generated. This error signal is passed to the feedback controller which afterwards generates the control signal. Most of the AFM systems use digital signal processor (DSP) based feedback controllers, which require high-speed analog-to-digital and digital-to-analog converters. Finally, the control signal needs to be amplified using high voltage amplifier in order to move the scanner z piezo. Also, when recording images with a HS-AFM, a large amount of data needs to be processed in real-time: analog to digital conversion of height and error signal, transfer of height and error data into the computer memory, displaying and/or saving data etc.

Many advances in AFM electronics have been reported over years, in the detector electronics [48–50], the data acquisition [14] and the piezo amplifiers [48, 51–55]. The speed of the feedback proportional-integral-derivative (PID) controller is one of the bottlenecks of the HS-AFM, where higher bandwidths enable faster scanning speeds and higher resolution. In the past many different approaches to increase the speed of the feedback controller were introduced. Schitter et al. [56] and Uchihashi et al. [57] used feedforward control technique, where they exploited the fact that two consecutive lines in AFM

raster scanning have very similar topography. Kodera et al. proposed dynamic PID controller, where gains of the PID are automatically altered depending on the value of the error [58]. Many other non-PID based control approaches were also implemented, such as H-∞ controllers [59–61] along with various other algorithms of modern control theory [62–65].

1.4 Deflection readout of AFM cantilevers

Deflection readout system presents very important part of any AFM, since its accuracy determines the AFM imaging resolution. Optical systems such as optical beam deflection (OBD) [66, 67] and interferometric [68, 69] provide the best noise performance. Beyond optical techniques, many other deflection sensing techniques were proposed in the past: capacitive [70–74], doped silicon and polysilicon piezoresistive [75–83], piezoelectric [84–87], magnetic [88,89] and thin metal film [90–92] deflection sensing and numerous alternative self-sensing techniques [93–97]. Although, so far none became preferable over optical sensing in routine AFM imaging, due to the comparatively lower signal-to-noise ratio (SNR), detection speed or complexity of integration.

Techniques with strain-sensing elements incorporated in the cantilever are particularly interesting, offering several advantages over external readout techniques [98]. These include a compact measurement setup that occupies little space and allows for integration in large cantilever arrays, imaging in environments with low or varying optical transparency, imaging of samples with geometrical constraints, imaging of light-sensitive samples, and potential to detect submicron-sized cantilevers [91].

In the subsequent chapter two sensing methods will be discussed in more details: OBD method as the current standard in AFM imaging and various strain-sensing methods due to their numerous advantages.

1.4.1 Optical Beam Deflection method

Optical beam deflection (OBD) is the most prevalent method for measuring cantilever deflections in atomic force microscopy, due to its low noise, its reliability and its ability to use a variety of cantilever sensors. OBD readout uses a focused laser beam to measure cantilever angular changes caused by deflection of the cantilever tip (see Figure 1.2a). The laser beam reflects from the cantilever surface towards a position sensitive detector,

where a shift in the laser spot position is measured. Further signal processing is usually achieved by using a transimpedance amplifier and voltage arithmetic electronics [67,99]. Recently, other electronic signal processing methods, such as one using bipolar current mirrors were also reported [49].

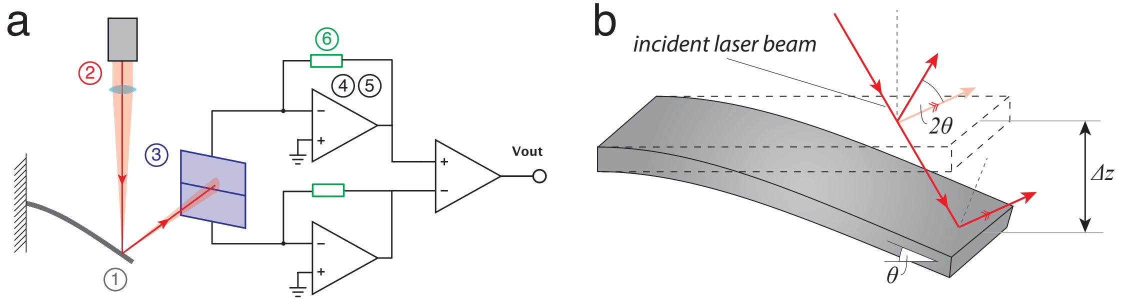

Figure 1.2: **a)** A schematic representation of the OBD measurement setup and the major noise sources: 1. Cantilever thermomechanical noise 2. Laser noise 3. Photodiode shot noise 4–5. Voltage and current noise of an amplifier 6. Noise of a feedback resistor. **b)** A schematic illustration of OBD sensing principle. OBD readout measures changes in the bending angle. Upon cantilever deflection, the laser spot will shift towards the cantilever free end. Also, the distance traveled by the laser will change due to Δz. However, in most cases these effects are negligible. The most important effect is the change of the angle of the reflected laser beam, equal to 2θ, where θ is the cantilever bending angle at the laser spot position. The laser spot should be positioned close to the cantilever free end, where the change in the angle is the highest.

An OBD readout measures cantilever deflection through angular changes (see Figure 1.2b). If a cantilever free end deflection Δz produces an angular change θ at the laser beam position ($x = l - l_b/2$, where l is the cantilever length and l_b is the diameter of the laser beam, along the cantilever length), then the signal measured by the optical readout will be proportional to $\tan(2\theta)$ where

$$\theta = \frac{3}{2l}\left(1 - \left(\frac{l_b}{2l}\right)^2\right) \cdot \Delta z \tag{1.4}$$

(see Appendix A.1). For small bending angles, $\tan(2\theta) \approx 2\theta$. Also, if $l \gg l_b$ the term in the brackets can be neglected. However, this term should be taken into account if cantilever dimensions become on par with laser spot dimensions (10s of microns).

The OBD method also has certain limitations, including a cumbersome measurement setup requiring frequent laser alignment and a cantilever with a reflective surface, and imaging artefacts due to stray light reflected by the sample surface. The latter phenomenon is a problem particularly in high quality metrology applications for the semiconductor industry. Furthermore, due to the optical diffraction limit, only cantilevers with widths down to a few micrometres are usable for imaging.

1.4.2 Strain-sensing readout methods

The first strain-sensing AFM cantilevers were using piezoresistive readout. Primarily doped silicon resistors were used [75–78, 80–83], followed by cantilevers with polysilicon [100–103] and thin metal film [90–92] strain-sensing resistors. Piezoresistors measure strain through a change in resistivity (effect dominant in semiconductors) and a change in geometry (effect dominant in metals). The sensors are usually configured in a Wheatstone bridge with differential amplification, where the measured voltage is directly proportional to the cantilever deflection (Figure 1.3a). Concurrently to piezoresistive cantilevers, piezoelectric self-sensing cantilevers using various materials (PZT, ZnO, AlN) were developed [84–87]. Two common readout configurations used for sensing of piezoelectric cantilevers are the charge amplifier (Figure 1.3b) and the voltage amplifier circuit (Figure 1.3c) [104].

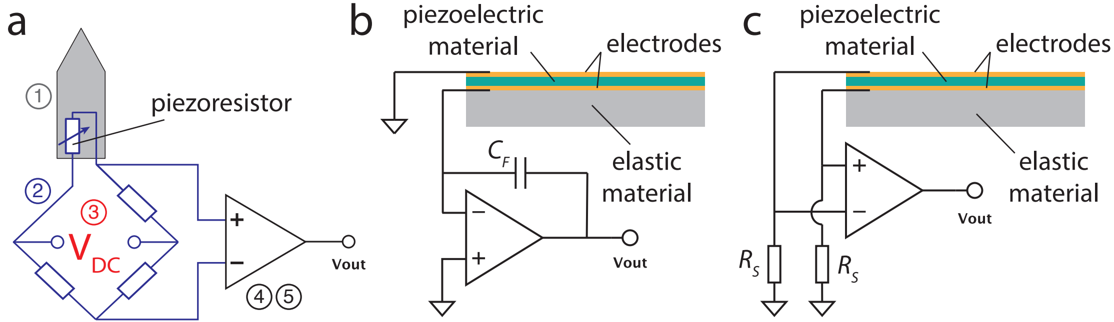

Figure 1.3: a) A schematic representation of the piezoresistive strain-sensing measurement setup and the major noise sources: 1. Cantilever thermomechanical noise 2. Wheatstone bridge resistor noise 3. Bridge voltage reference noise 4–5. Voltage and current noise of a differential amplifier. **b-c)** A schematic representation of the piezoelectric measurement setup: **b)** charge amplifier and **c)** voltage amplifier circuit

A strain-sensing readout measures cantilever deflection through the strain induced in the sensor. An average longitudinal strain ε in a sensor positioned at the cantilever fixed end (see Figure 1.4), induced by the cantilever free end deflection Δz can be approximated as

$$\varepsilon = \frac{3}{2} \cdot \frac{(t \pm t_s)\,(1 - l_s/2l)}{l^2} \cdot \Delta z \tag{1.5}$$

where l and t are the cantilever length and thickness; and l_s and t_s are the piezoresistor length and thickness. Thickness of the sensing resistor is incorporated in equation (1.5) either with plus sign, if the resistor is deposited on the cantilever surface (e.g. like thin Au film resistors) or with minus sign, if the resistor is incorporated in the cantilever body (e.g. doped Si piezoresistors).

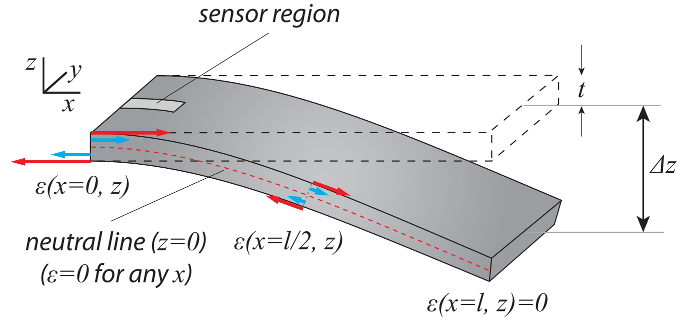

Figure 1.4: Strain-sensing readout measures changes in the induced strain. Thee strain is always zero on the cantilever neutral line (dashed red line), along the whole cantilever length. The strain varies linearly along the cantilever thickness, with maximum compressive strain at the bottom, zero strain at the neutral line and maximum tensile strain at the top (coloured arrows). Along the cantilever length, strain also varies linearly from a maximum at the cantilever fixed end to zero at the cantilever free end (coloured arrows). Therefore, the piezoresistor should be positioned at the regions of maximum strain – the top or bottom surface of the cantilever fixed end.

A fundamental parameter describing the performance of a piezoresistive strain sensor is the gauge factor κ which is defined as:

$$\kappa = \frac{\Delta\rho/\rho}{\varepsilon} + 1 + 2\nu \qquad (1.6)$$

where $\Delta\rho/\rho$ is the relative change of the piezoresistor resistivity and ν is the Poisson ratio of the piezoresistor material. For n-type Si, gauge factor has values up to +200, and for n-type Si gauge factor goes down to −125 [105]. For metals, change in the resistivity with strain is negligible and the gauge factor is usually ≈ 2 (e.g. thick gold film has $\nu \approx 0.42$).

1.4.3 Deflection readout of small-sized cantilevers

As it was already discussed, a reduction in cantilever size increases both sensitivity and detection speed [91,106]. As the cantilever dimensions are decreasing, the diameter of the laser beam in OBD readout becomes larger than the cantilever dimensions (usually the width) and we become limited by optical diffraction effects. Theoretically, the laser beam can be focused down to the minimum width w_b (measured between the $1/e^2$ irradiance points):

$$w_b \cong \frac{2\lambda}{\pi \cdot NA} \qquad (1.7)$$

where λ is the laser wavelength (usually used $\sim$ 650 nm) and NA is the numerical aperture of the focal lens (where the maximum NA currently achievable in air is around ~ 0.8). This gives theoretical minimum of $w_b \approx 0.5\,\mu m$. However standardly available lenses have lower NA and certain imperfections are always present, leading to $w_b \approx 2\,\mu m$ at best.

This diffraction limit presents a major barrier for the use of OBD readout with increasingly miniaturized cantilevers. Currently existing specialized HS-AFM prototypes use the smallest possible cantilevers that are detectable with a modified optical beam deflection technique. In these systems, the laser beam is focused onto small cantilevers using an objective-lens system [37, 107]. However, further increase in the speed requires reduction of size of the cantilevers well below the optical diffraction limit. Therefore, an alternate detection scheme is required.

Several approaches based on advanced optics have been proposed to detect the deflection of small cantilevers that can no longer be measured using the conventional OBD method (Figure 1.5a-c). Antognozzi et al. [108] have developed a system to detect the deflection of vertically mounted cantilevers using the scattering of an evanescent electromagnetic wave (SEW) above the transparent substrate in a 25 µm area around the tip. The motion of the cantilevers is detected through an interference pattern of the scattered light and the incident laser beam. However, this system is limited to low scattering of evanescent waves and to small aspect-ratio samples on a flat surface.

Sanii and Ashby used the Mie scattering of the nanowire focused on a split photodiode for position detection [109]. The system can detect cantilevers down to 100 nm width and 40 µm length. Disadvantages of this system are that it can't be used for detection of short cantilevers (shorter than 1 µm) and that positioning and focusing of the optical system is very complex.

Optomechanical transduction such as that proposed by Srinivasan et al. has recently shown the fundamental capability of detecting thermal vibrations using optical resonance in a nanoscale gap between a nanocantilever and a microdisc resonator, all integrated on one device layer of the NEMS device [110]. While Srinivasan et al. envision the use of this detection for AFM in the future, they mention that several more technological developments are required in order to obtain functional devices.

Roukes demonstrated the ability to measure the resonance spectrum of freestanding cantilevers using resistive readout of a 30 nm thick gold film on the SiC cantilevers [91]. The sensitivity of this readout is increased with cantilever dimensions decrease and has been

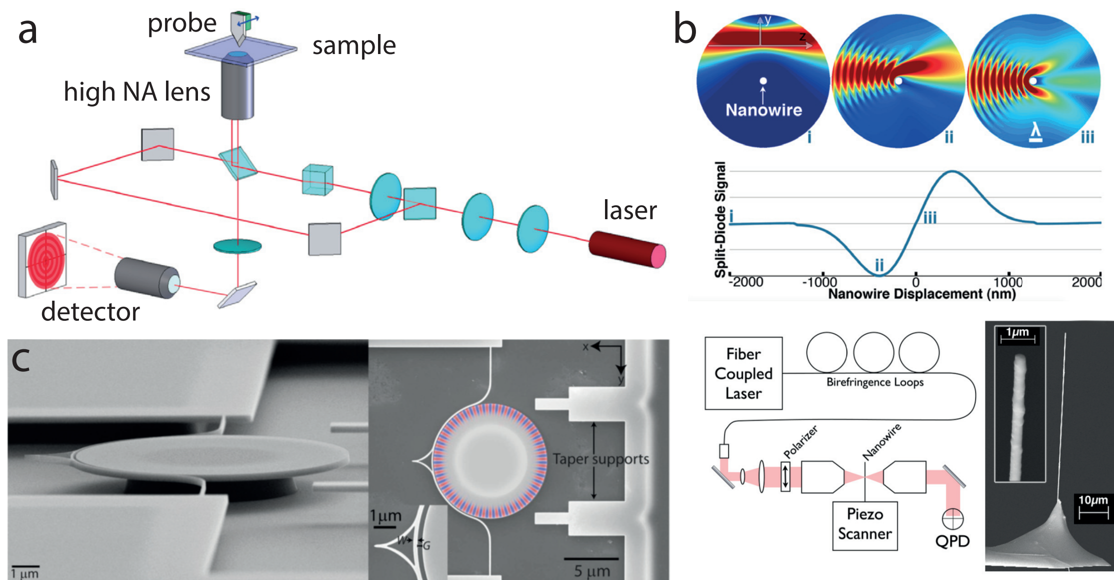

Figure 1.5: Several advanced optics approaches proposed for deflection sensing of small-sized cantilevers: **a)** Deflection detection using the scattering of an evanescent electromagnetic wave [108]: a diagram of the SEW detection system. **b)** Deflection detection using the Mie scattering of the nanowire focused on a split photodiode [109]: above - the calculated local intensity as a nanowire translates through a Gaussian beam and the simulated profile of the photodiode signal, below - a detection scheme and a scanning electron microscope (SEM) image of a nanowire cantilever used in measurements. **c)** Deflection detection using optical resonance in a nanoscale gap between a nanocantilever and a microdisc resonator [110]: SEM images of a cantilever-microdisc system.

demonstrated up to 127 MHz cantilever resonance frequency. Use of these cantilevers for AFM in air could also be promising, but has not yet been shown. Also, these resistors have low values, which result in large currents through the sensors making them difficult to use in fluids. Using thin metal films for sensing of small-sized cantilevers also has a disadvantage in the fact that the resistance of the sensor can become much less than the resistance of the connecting leads, which can significantly reduce the effective signal (for details see Section 2.4.3).

Doll et al. managed to make very thin and narrow self-sensing cantilevers [81], having the thickness $t = 300\,\text{nm}$ and the width $w = 1\,\mu\text{m}$. The sensing is performed using shallow n-type doped Si piezoresistors. Such cantilevers were designed for high bandwidth and high resolution force measuring. However, currently it is technologically very challenging to fabricate shallow piezoresistors, necessary to maintain the SNR performance.

People have also demonstrated usage of thin piezoelectric films for cantilever deflection sensing. Ivaldi et al. developed self-sensing cantilevers incorporating only 50 nm thick AlN piezoelectric film [87]. However, the overall thickness of such cantilevers is still

very large (cantilever thickness is close to a micron) as surrounding metal electrodes are necessary to connect the piezoelectric layer and a certain thickness of the cantilever body material is necessary to achieve a satisfactory SNR performance.

Clearly, deflection readout of small-sized cantilevers is still very challenging. On the one hand, optical methods demand very complicated and space consuming measurement setups. On the other hand, it is very challenging to make small-sized strain sensors and still maintain their SNR performance. In the scope of this thesis I was investigating a novel self-sensing method for deflection sensing of nanomechanical cantilevers. The sensing method is based on electron co-tunneling through a nanogranular metal [97,111]. It was successfully used in AFM imaging and for deflection sensing of 100 nm thick and 500 nm wide cantilevers. The following chapter describes the sensing principal and sensor implementation on the AFM cantilevers, and discusses the achievable performance of these sensors.

Chapter 2

Nanogranular Tunneling Resistors in AFM

The sensitivity and detection speed of cantilever-based mechanical sensors increases drastically by decreasing their size [91]. The need for such increased performance drives their sub-micrometer miniaturization in a broad variety of research fields for nanoscale sensing of topography [106], mass [112] or small forces [98, 113]. However, existing detection methods of the resonator motion do not scale down easily. This prohibits further increase in sensitivity and detection speed, and thereby limits progress in emerging areas such as personal diagnostics [114, 115] and high-speed atomic force microscopy [21, 30].

In this chapter a novel nanomechanical readout method is introduced that overcomes these limitations. The sensing method is based on inelastic electron co-tunneling through a nanogranular metal [111]. We refer to these sensors as the nanogranular tunneling resistors (NTRs). The sensors can be deposited through rapid prototyping with lateral dimensions down to 10s of nm, thereby allowing the readout of nanoscale resonators without constraints on their size, geometry or material. By modifying the intergranular tunnel-coupling-strength, the sensors' conductivity can be tuned by up to four orders of magnitude to optimize their dynamic performance [116]. Our results show that these sensors are functional on 500 nm wide cantilevers and that their sensitivity is well suited even for demanding applications such as AFM imaging. The unprecedented scalability and versatility opens the door for the development of a new generation of self-sensing nanoscale resonators ranging from nanowire cantilevers for high-speed atomic force microscopy [21] to 3D resonators [117].

Research regarding development of the NTR cantilevers was done in collaboration with Prof. Dr. Michael Huth and his group for thin films and nanostructures. My contribution regarding research presented in this chapter was published in [97,118–120], with the main manuscript [121] currently being under revision.

The chapter explains the NTR deposition process and functional principal, and gives a feasibility analysis of the NTR application for the use in AFM. The instrumentation necessary for AFM imaging is described, along with the custom designed self-sensing NTR cantilevers. Finally, AFM imaging results achieved with the NTR cantilevers are presented.

2.1 Introduction

Decreasing cantilever dimensions to the sub-micrometer range drastically decreases its inertial mass and thereby increases its sensitivity, resonance frequency and detection bandwidth [19, 91, 98]. Such miniaturization has recently pushed the limits in studies of nanoscale processes, enabling video rate imaging in high-speed AFM [19,21,30]. However, as was described in Section 1.4.3, further decrease in size rules out standard optics-based approaches to measure cantilever deflection, as the cantilever dimensions are below the conventional optical detection limit.

Strain sensors integrated with the cantilever can circumvent the problems with optical detection. These sensors can be piezoelectric or piezoresistive in nature. However, a fundamental problem for using these sensing materials on very small cantilevers is the minimum required size and especially thickness of the sensor elements (100s of nanometers to micrometers). This often exceeds the total allowable thickness of these cantilevers, typically less than 100 nm.

Here, we present an approach to self-sensing of nanomechanical cantilevers that overcomes these problems. We use nanoscale additive deposition (3D printing) of nanogranular metals to directly write nanometer-sized nanogranular tunneling resistor (NTR) strain sensors onto prefabricated cantilevers. The tunneling nature of the electron transport in the nanogranular metal results in a highly tunable, sensitive strain gauge with thicknesses down to around 5 nm and widths around 20 nm.

2.2 NTR deposition process

The NTR sensors are deposited using focused electron beam induced deposition (FEBID). For this, a platinum based gaseous precursor trimethylmethylcyclopentadienyl-platinum(IV) [MeCpPt(Me)3] is introduced through a capillary, in the vicinity of the focal spot of a scanning electron microscope (see Figure 2.1). The precursor molecules adsorb on the surface and are dissociated in the focus of the scanned electron beam [122]. As a consequence, a deposit (NTR) is formed, while the volatile products are diffused and pumped away.

In the deposit, the freed platinum atoms form clusters or nanoparticles which become embedded in a matrix of deposited carbon atoms. The Pt(C) NTRs are composed of $22-23$ at% Pt and $77-78$ at% C, in form of platinum nanocrystallites with a diameter of $2-5$ nm which are embedded in a dielectric, carbonaceous matrix. The NTR sensor can be 3D printed on almost any substrate material and, due to the excellent depth of focus, on almost arbitrarily shaped surfaces.

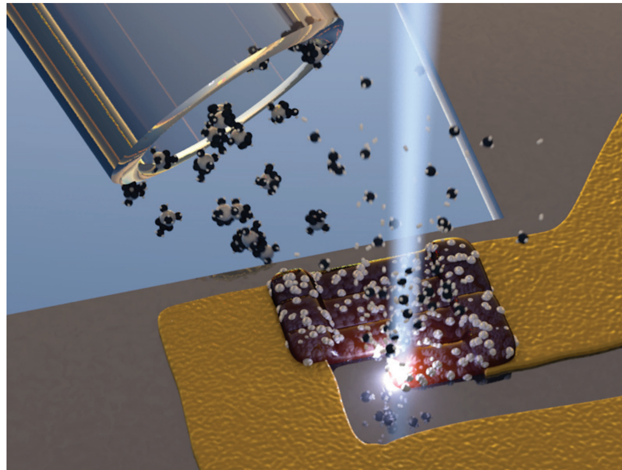

Figure 2.1: An illustration of the NTR electron beam induced deposition process. Precursor gas molecules adsorb and diffuse on the surface where they are dissociated by the scanned electron beam and form platinum clusters embedded in a carbonaceous matrix.

The NTR sensors were fabricated using a dual-beam SEM/focused electron beam (FIB) microscope (FEI, Nova Nanolab 600) equipped with a Schottky electron emitter with an ultimate resolution of 1 nm. The microscope is equipped with a gas injection system, which introduces the precursor gas via a 0.5 mm diameter capillary in close proximity to the focus of the electron beam. An electron beam energy of 5 keV and an electron current of 1.1 nA were employed for the FEBID process using s-shaped stripe-like patterns (serpentine scanning mode) that were repeatedly rastered over the structure at fixed dwell time per pixel (1 µs) and pitch (20 nm) between pixels.

2.3 NTR functional principal

The charge transport in NTR sensors occurs through tunneling between the Pt nanoparticles. This tunneling process strongly depends on the Coulomb charging energy E_C of the nanoparticles, and the inter-granular tunnel coupling strength g. E_C is largely determined by the capacitance C of the nanoparticles (in the dielectric matrix) and therefore their size. g is dominated by the properties of the dielectric matrix and the particle-to-particle distance. The exponential dependence of the tunneling probability on the inter-granular distance suggests the suitability of the material as a high sensitivity strain sensor. When the material is strained, the average distance between the particles increases, the tunneling probability decreases and the resistivity of the NTR increases. Previous attempts to use tunneling as strain sensing readout have focused on the integration of single tunnel junctions or single electron transistors onto cantilevers [94, 95]. In NTR sensors, however, multiple tunneling events are involved in electron transfer through the whole resistor (represented by the chain of solid arrows in Figure 2.2a).

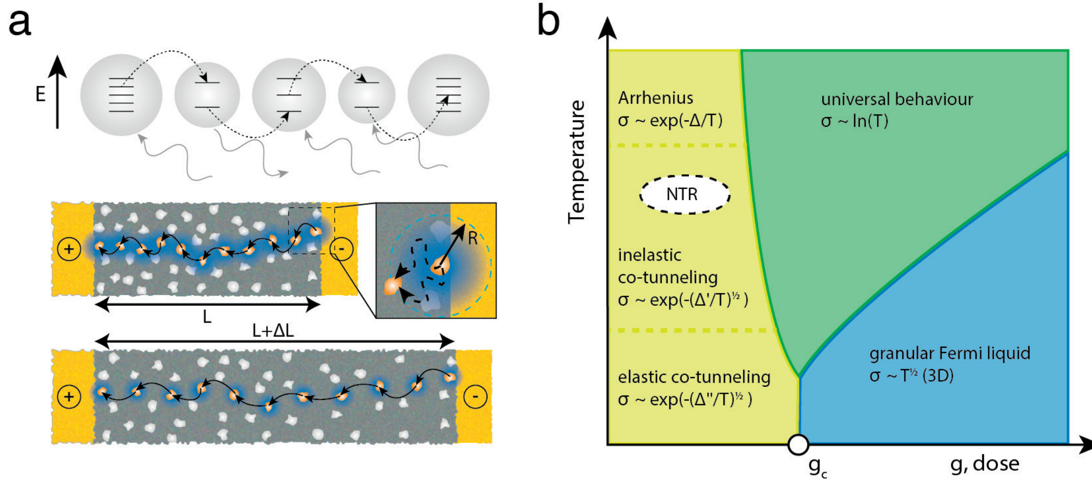

Figure 2.2: NTR strain-sensing functional principal: **a)** Schematic depiction of the inelastic co-tunneling process in the NTR. Electrons tunnel through several grains at the same time via virtual energy levels. The co-tunneling radius therefore is larger than the inter grain distance (blue halos). When the sensor is stretched, the inter grain distance increases and the co-tunneling radius decreases which results in an increased resistance. **b)** Phase diagram of the electronic transport regimes in granular metals. This phase diagram was theoretically predicted based on recent theoretical investigations [123] and was largely verified experimentally by very recent experiments on Pt(C)-based granular metal samples with finely tuned tunnel coupling g [116]. The conductivity temperature dependence is given for each regime, where $\Delta' - \Delta'''$ are temperature constants that depend on the NTR material properties and conduction regime [124]. At room temperature and the prevailing coupling strength, the NTR sensors operate within the inelastic co-tunneling regime.

Transport mechanisms in nanogranular metal can differ significantly due to the wide possible range of the inter-granular coupling strength. This results in a phase diagram of the transport regimes, as is schematically depicted in Figure 2.2b. The regime of activated transport or correlated variable range hopping (dashed region in Figure 2.2b) is most relevant for the strain-sensing effect in the cantilever sensors [124]. In this regime, the Coulomb blockade of each single nanoparticle is partially lifted by charged defects surrounding it [125]. As the nanoparticle size gets smaller, the charging energy grows like $E_C \sim 1/C$. As a consequence, charge transport is dominated by thermally assisted tunneling between nanoparticles in a way that the electrostatic energy of the charge carriers along the tunneling path is kept small. Theory suggests that for these NTR materials at room temperature each individual electron transfer event is a co-tunneling event where electrons can hop over distances larger than the average distance between two nanoparticles [123]. This tunneling process can occur through tunneling via virtual electron levels in a sequence of nanoparticles (dotted arrows in Figure 2.2a). The result is a co-tunneling radius r shown in blue. Due to their small size, the nanoparticles exhibit discrete quantum mechanical energy levels inside the grains. During co-tunneling the energy level of the starting particle and the energy level of the final particle can be different. The electron therefore creates electron-hole excitations as it tunnels out of the virtual intermediate state, making the co-tunneling inelastic. From this theoretical description of the electron transport process we can derive guidelines for optimization of the NTR material by tuning the deposition and post processing conditions.

2.4 A feasibility analysis: the NTR readout for AFM

We wanted to develop self-sensing cantilevers incorporating NTR readout. In order to apply any strain-sensing method for sensing of the small-sized cantilevers (by small-sized we will refer to cantilevers whose deflection is not detectable with optical readout present in conventional AFMs) and for HS-AFM imaging there are several criteria that strain sensor needs to satisfy:

1. One must be able to deposit a functional sensor having very small size. The small thickness of the sensor is especially important, as any additional thickness of the sensor would stiffen the cantilever in the area around the sensor. This would shift the neutral axis of the cantilever and disrupt its mechanical properties.
2. A certain optimal resistance of the sensor is necessary. On the one hand, lower resistance means less resistor noise ($1/f$ and Johnson's noise) in the readout. Lower resistance is also desirable because there is always a certain parasitic capacitance

present in the readout (from connecting leads, at the input of the amplifier etc.). This capacitance with the resistance of the strain sensor forms a *RC* low pass filter, which limits the electrical bandwidth of the readout [126]. On the other hand, if resistivity of the sensor is too low, resistance of the small-sized sensor will become comparable to the parasitic resistance of the connecting leads, which can significantly reduce the effective signal (see Section 2.4.3).

3. Finally, the sensor needs to have enough sensitivity to allow imaging of a topography at the nano scale.

We will discuss these criteria for the case of the NTR sensor.

2.4.1 NTR sensor dimensions

The 3D additive fabrication of the NTR sensors allows for extreme flexibility in sensor length, thickness and width. Minimizing the thickness and width of the sensing element is crucial to maintain a high signal from a strain-sensing element in a nano-cantilever. The sensor should be thin enough as to not contribute much to the flexural rigidity of the cantilever. This is especially problematic for nano-cantilevers intended for measurement of small forces at high bandwidths (such as cantilevers for high-speed AFM). Cantilevers for the next generation high-speed AFM will require total thicknesses below $50-100$ nm, and width below 500 nm, which rules out the use of sensors made of conventional self-sensing materials such as doped Si, PZT or AlN, at least with their current state-of-the-art fabrication techniques. One of the most extraordinary features of our NTR sensors is the scalability of the sensor in thickness and width, down to single nanoparticles in height and 10 nm in width. Figure 2.3a shows NTR sensors deposited with varying widths. The inset shows a continuous sensor having a width of 25 nm and a thickness of 15 nm. Figure 2.3b shows how thickness of the NTR sensors from Figure 2.3a was increased, with successive scanning electron beam passes. The smallest NTR thickness was around 5 nm.

In most cases, the optimal performance of a resistive strain sensor on a cantilever is reached when the active length of the sensor (i.e. the gap between the electrodes) is as short as possible without compromising the electron transport mechanism. This is because the sensor length influences the resistance and thereby the Johnson noise. By controlling the gap size between the electrodes before deposition, we can control the active sensor length. Figure 2.4a presents AFM images of several NTR sensors with different active sensor lengths (ranging from $40-200$ nm). The active sensor length is

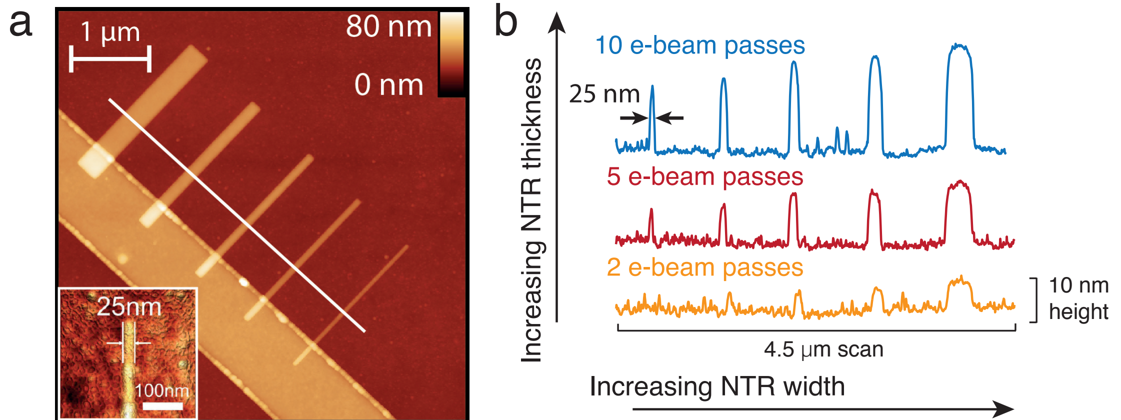

Figure 2.3: Scalability of the NTR sensor in thickness and width. **a)** An AFM image of NTR sensors deposited with varying widths. Inset: a continuous sensor having a width of only 25 nm. **b)** Thickness of the NTR sensors, presented in a), after 2, 5 and 10 e-beam passes. With each e-beam pass the thickness of the NTR deposit is grown. The smallest thickness was around 5 nm. The achievable resolution here is primarily determined by the substrate roughness.

determined only by the electrode gap. Figure 2.4b presents a zoomed-in AFM image of an NTR sensor with the active sensor length of only 40 nm. In such short active sensor lengths, only $10-15$ nanoparticles in a direct chain are involved in the strain sensitive electron transport (for grain sizes of about $2-3$ nm at 0.5 nm peripheral distance). Still, the I/V-characteristic for different active sensor lengths (see Figure 2.4c), shows linear behavior up to a threshold electric field of at least 15 kV/cm, beyond which local heating effects lead to deviation from linearity.

2.4.2 NTR sensor resistance and gauge factor

NTR sensors have an interesting property that their resistance and gauge factor can be tuned by post-growth electron irradiation The post-growth electron irradiation increases the inter-granular tunnel coupling strength g, since it leads to a transformation of the carbon matrix from amorphous carbon to nanocrystalline graphite resulting in a strong reduction of the resistivity of the strain sensor elements [116]. This is shown in Figure 2.5a for a typical sensor. Besides transformation of carbon matrix structure, additional electron irradiation also induces dissociation of non-dissociated precursor molecules (which are always present to some extent). Additionally, certain amount of carbon will be further removed in the form of CO or CO_2 gasses.

With the gradual increase of the irradiation dose, the resistance of the sensor elements drops by two orders of magnitude as a function of dose d in the relevant transport regime

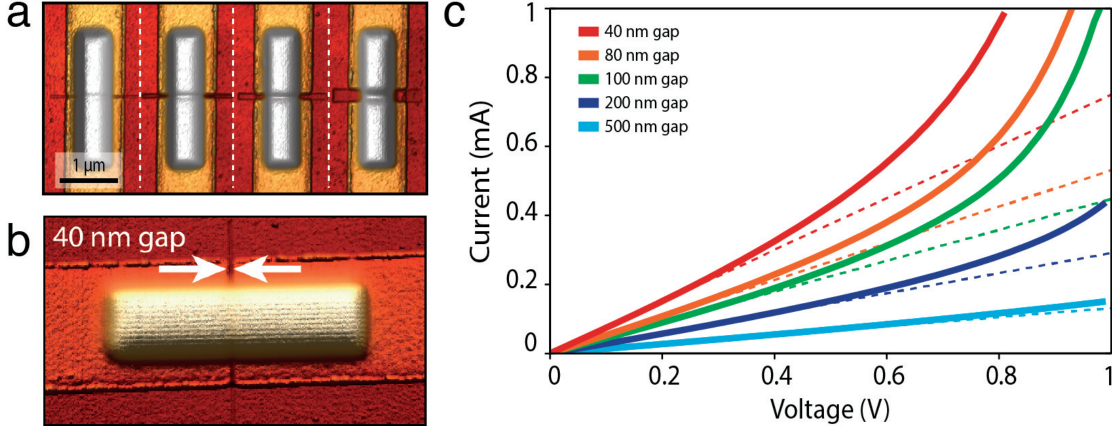

Figure 2.4: Scalability of the NTR sensor in length. **a)** AFM images of NTR sensors with different active sensor lengths. **b)** The active sensor length is determined only by the electrode gap, which can go down to 40 nm. The individual lines of the e-beam NTR writing process can be seen. **c)** I/V curves of un-strained NTR sensors for different active sensor lengths. E-beam irradiation dose used after sensor deposition was 74 nC/µm. Dashed lines serve to guide the eye and present sensor I/V dependence in the linear regime. We hypothesize that at higher voltages the onset of non-linearity is due to overheating effects.

(see Figure 2.5a). As predicted, the gauge factor of the strain sensor drops as well (see Figure 2.5b).

Here, we use the observed dose-dependence of resistance and gauge factor to optimize the signal-to-noise ratio (SNR) achievable with NTR-based strain sensors on very small cantilevers. We define the SNR as the ratio of the cantilever peak thermomechanical fluctuations to the NTR voltage noise, scaled by the deflection sensitivity:

$$SNR = \frac{A_{\max}}{n_J \cdot DS} \tag{2.1}$$

where $A_{\max}$ represents the peak of the cantilever thermomechanical noise spectral density at cantilever resonance frequency, n_J is the NTR noise spectral density at cantilever resonance frequency and DS is the deflection sensitivity of the measurement system.

$A_{\max}$ is given by

$$A_{\max} = \sqrt{\frac{4}{3} \cdot \frac{4k_BTQ}{2\pi f_0 k}} \tag{2.2}$$

where k_B and T are Boltzmann constant and temperature; Q, k and f_0 are cantilever quality factor, spring constant and resonance frequency. The parameter 4/3 represents a correction factor due to a non-perfect harmonic oscillator behaviour of the cantilever and the fact that the induced strain, rather than deflection is measured with strain-sensing element [127, 128].

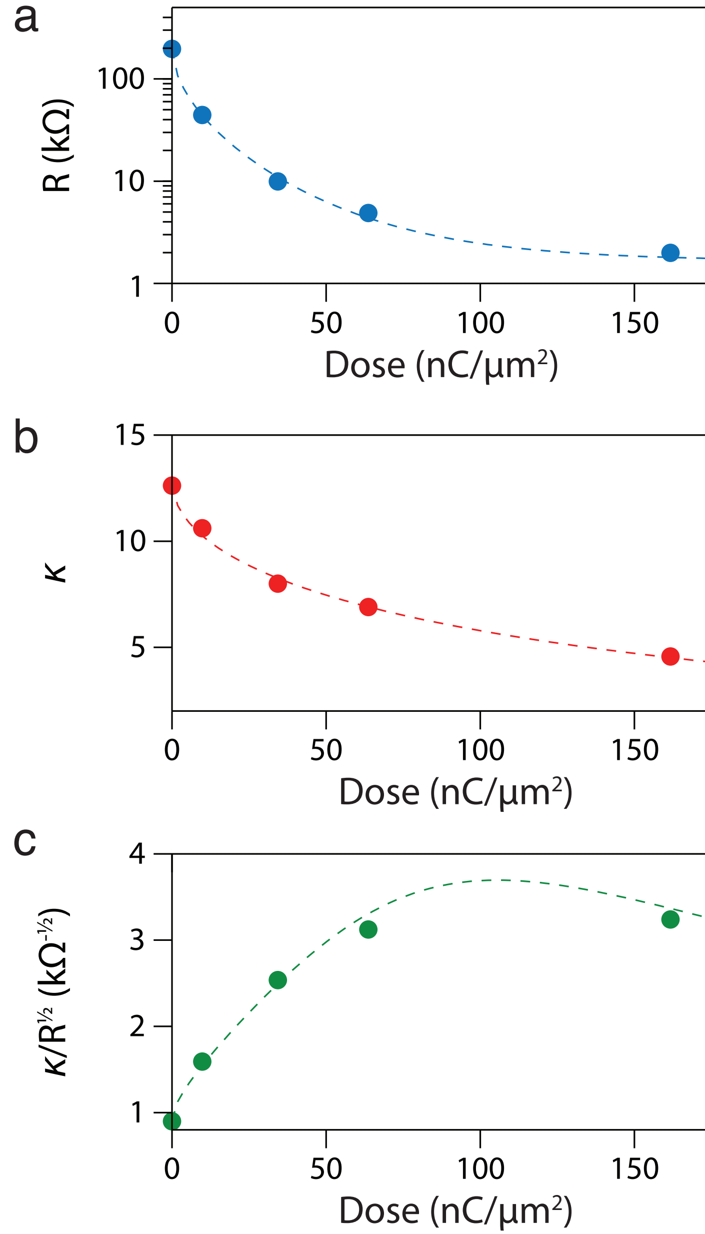

Figure 2.5: Signal-to-noise ratio optimization of NTR sensors. **a)** Measured reduction of resistance R of typical NTR strain sensor element (active sensor element size $4 \times 2 \times 0.2\,\mu m^3$) vs. effective post growth electron irradiation dose. Within the applied dose range transport remains in the inelastic co-tunneling regime (see dashed ellipse in Figure 2.2b). **b)** Associated measured drop of NTR gauge factor κ vs. irradiation dose. **c)** Calculated dose-dependent signal-to-noise ratio as a consequence of its $\kappa/\sqrt{R}$ dependence given in Equation (2.5). The dashed lines serve to guide the eye.

The NTR noise spectral density n_J [111] and the deflection sensitivity DS [104] are given by

$$n_J = \sqrt{4k_BTR} \tag{2.3}$$

$$DS = \frac{8}{3} \cdot \frac{1}{\kappa V_s} \cdot \frac{l^2}{t\left(1-\frac{l_s}{2l}\right)} \tag{2.4}$$

where R is resistance of the NTR, V_s is supply voltage to the Wheatstone bridge, κ is gauge factor, l_s is NTR sensor length, and l and t cantilever length and thickness. Finally, such defined SNR is

$$SNR = \frac{A_{\max}}{n_J \cdot DS} = 0.173 \cdot \frac{\kappa}{\sqrt{R}} \cdot V_s \cdot \frac{t\left(1-\frac{l_s}{2l}\right)}{l^2} \cdot \sqrt{\frac{Q}{kf_0}} \tag{2.5}$$

factorized in NTR sensor element specific aspects (κ: gauge factor, R: resistance, V_s: supply voltage to the Wheatstone bridge) and a geometry/material factor governed by the cantilever dimensions (l_s: NTR sensor length, l and t: cantilever length and thickness) and its oscillator properties (Q: quality factor, k: spring constant, f_0: resonance frequency). For simplicity, the numerical constant 0.173 in the SNR expression is calculated from all other numerical constants.

Figure 2.5c shows the NTR-specific sensitivity factor $\kappa/\sqrt{R}$ as a function of the post-growth irradiation dose. The sensitivity increases by more than a factor of 3 for low doses. A rather broad sensitivity maximum occurs for dose values between 75 and 200 nC/µm^2, which results in reproducible sensor performance.

During NTR fabrication, the post-growth electron irradiation was performed using electron beam energy of 5 keV, electron current of 2.6 nA, dwell time of 10 µs and pitch of 20 nm.

2.4.3 Influence of parasitic resistances on the SNR

As was previously mentioned, the minimum required thickness of the strain sensor often presents a challenge. With miniaturisation of cantilever dimensions towards sub-micrometer range, desirable cantilever thickness is typically less than 100 nm. However, the thinnest self-sensing cantilevers incorporating standard strain sensors, such as piezoelectric [87] or piezoresistive [81], are several 100s of nm thick which is not acceptable.

Li et al. [91] have demonstrated the sensing of impressively small cantilevers using very thin metal film sensors (30 nm) by measuring the change in resistance mostly due to geometric effects. With such approach however, as the size of the cantilever is decreased, the resistance of the thin gold film resistor decreases as well. In the measurement setup there will always exist some parasitic resistances of the connection lines. When these resistances become on par with the resistance of the strain sensing resistor, the SNR of the readout will start to decrease significantly. One benefit of the NTRs is that they can be deposited with sub-micron dimensions while their resistance can be tuned by post irradiation, hence always keeping the resistance in an optimal range. Here we performed a comparison of a SNR loss due to parasitic resistances, for both thin Au film and NTR sensor.

In order to compare the SNR loss due to parasitic resistances in thin gold films and NTR deflection readout, we performed a case study. We assume that the change of the resistance is measured using a Wheatstone bridge, with one active resistor positioned on the cantilever and three passive resistors. We will denote the total parasitic resistance of each trace connecting the bridge as R_P^* (see Figure 2.6a). Parasitic resistances of the connection lines in the bridge itself are neglected as they can be designed to be fairly small. For the ease of writing, we define $R_P = 2R_P^*$. We would like to maximize the input

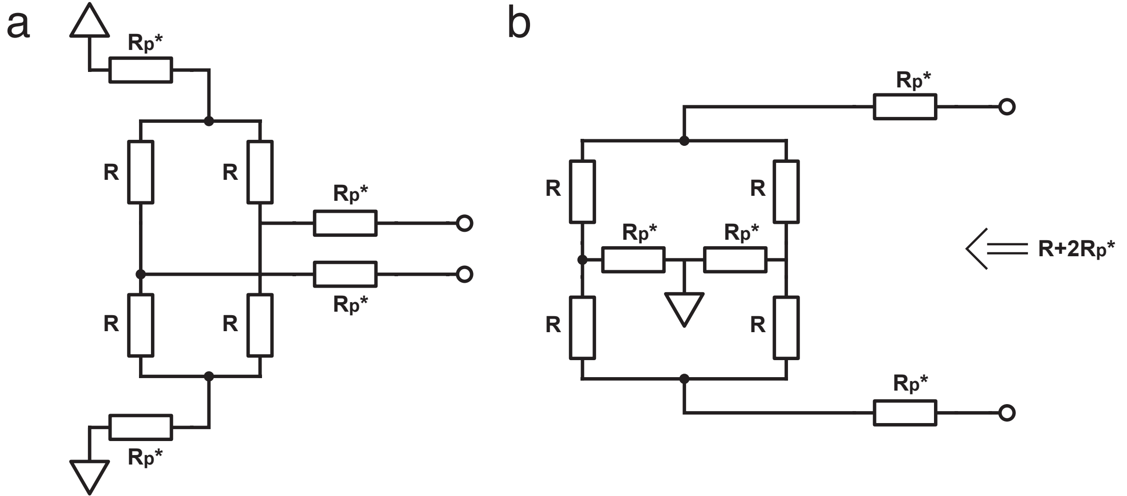

Figure 2.6: Influence of parasitic resistances on the SNR. **a)** Schematic of the Wheatstone bridge readout. **b)** Equivalent resistance circuit for Johnson noise estimation.

bridge voltage V_{in} in order to get a higher output signal. The maximum input voltage that we can apply is defined by the maximum allowed current through the resistor $I_{\max}$ as $V_{in,\max} = 2\,(R + R_P)\,I_{\max}$, where R is resistance of the bridge resistors. In this case, for a certain cantilever deflection δ, the maximum achievable output voltage of the circuit is

$$V_{out} = \kappa \cdot \frac{3\left(l - \frac{l_s}{2}\right)(t + t_s)}{2l^3} \cdot \delta \cdot \frac{I_{\max} R}{2} \tag{2.6}$$

where l and t are the cantilever length and thickness; l_s and t_s represent the length and thickness of the sensing resistor and κ is the sensor gauge factor.

In order to estimate the SNR of the readout, we are considering the intrinsic noises of the circuit resistors. For simplicity, we will not take into account the low frequency $1/f$ noise as we are only considering the case where resistors are used for strain sensing at higher frequencies, with band pass filtering around the working frequency. In this case the overall circuit noise comes from the circuit Johnson noise:

$$V_J = \sqrt{4k_B T B\left(R + R_P\right)} \tag{2.7}$$

where k_B, T and B represent Boltzmann constant, temperature in Kelvins and measurement bandwidth, respectively. This formula results from the fact that V_{in} is an AC ground, so the equivalent resistance seen from the output ports of the bridge is $R + 2R_P^* = R + R_P$ (see Figure 2.6b).

The SNR of the readout for a given cantilever deflection can be calculated as

$$SNR = \frac{V_{out}}{V_J} = \kappa \cdot \frac{3\left(l - \frac{l_s}{2}\right)(t + t_s)}{4l^3} \cdot \frac{I_{\max}}{\sqrt{4k_B T B}} \cdot \frac{R}{\sqrt{R + R_P}} \cdot \delta \tag{2.8}$$

Case study

The cantilever used in our calculations is a silicon nitride cantilever ($E = 250\,\mathrm{GPa}, \rho = 3100\,\mathrm{kg/m^3}$), having dimensions of $3 \times 1 \times 0.1\,\mathrm{\mu m^3}$. The measurement bandwidth is set to 500 kHz and the point load induced deflection of the cantilever is set to $\delta = 1\,\mathrm{nm}$. Calculations were made for three values of the connection lines parasitic resistance $R_P^* = 5\,\Omega$, $25\,\Omega$ and $50\,\Omega$.

Two types of resistive strain sensors were compared: a U-shaped thin gold film resistor and a cuboid shaped NTR resistor. The assumed properties of each resistor are given in Table 2.1. Properties for each resistor are chosen in a way to maximize its performance. The resistivity value chosen for the thin gold film corresponds to the resistivity value we measured for an evaporated 5/30 nm thick Cr/Au film. The irradiation dose used for NTR post deposition resistance tuning is $75\,\mathrm{nC/\mu m^2}$.

Table 2.1: Parameters used for calculation of the expected SNR performance of thin gold film sensor versus NTR sensor

Parameter	**Thin gold film**	**NTR**
Resistor shape	U-shaped	Cuboid
Length l_s [µm]	$0.1 - 6$ (arm length is $l_s/2$)	$0.05 - 0.5$
Width w_s [µm]	0.2	0.6
Thickness t_s [nm]	30	30
Gauge factor κ	4.5	6
Resistivity ρ [Ω m]	5×10^{-8}	3.37×10^{-4}
Maximum current density $J_{\max}$ $\left[\mathrm{A/m^2}\right]$	Limited by electromigration: 1×10^{11}	Limited by nonlinearity in conductivity: $E_{\max} = 1.5\,\mathrm{MV/m}$, $J_{\max} = E_{\max}/\rho$

Results obtained by the calculation are plotted in Figure 2.7. SNR losses due to parasitic resistances are much larger for the case of the thin gold film resistor. This is because the maximum achievable resistance for the gold film resistor is around 50 Ω (when the gold trace goes along the whole cantilever length). By varying post deposition irradiation dose and resistor length, for chosen thickness and width of the sensor (Table 2.1), the resistance of the NTR can be tuned from several 100s of Ω to several 10s of kΩ.

2.5 Self-sensing NTR cantilevers for AFM

We wanted to develop small-sized self-sensing NTR cantilevers to perform high-speed AFM imaging, in both air and fluid. Several generations of NTR cantilevers were developed, where size of the cantilever and/or NTR sensor were gradually decreased. Figure 2.8 shows a montage of different size cantilevers equipped with NTR sensors (see orange arrows and inset figures), with cantilever widths down to 500 nm (cantilever 5, see also Figure 2.19a).

Cantilevers 1-4 were fully released and were successfully used in AFM imaging (see 2.5.2). They were fabricated using standard microfabrication techniques. Contacts to the NTRs were made with Cr/Au traces. On the $20 \times 8 \times 0.3\,\mu\mathrm{m}^3$ cantilevers (cantilever 4) the fine-scale electrical contact structures were defined in the Cr/Au traces using focused ion beam (FIB) milling. In the last step NTR resistors were deposited. Since FEBID is a serial process, the writing time for one sensor depends strongly on the size. For the smallest fully released AFM cantilever (cantilever 4, see Figure 2.11a as well) write time is in the order of two minutes for full bridge of NTR sensors, with an additional irradiation time of 1.5 min.

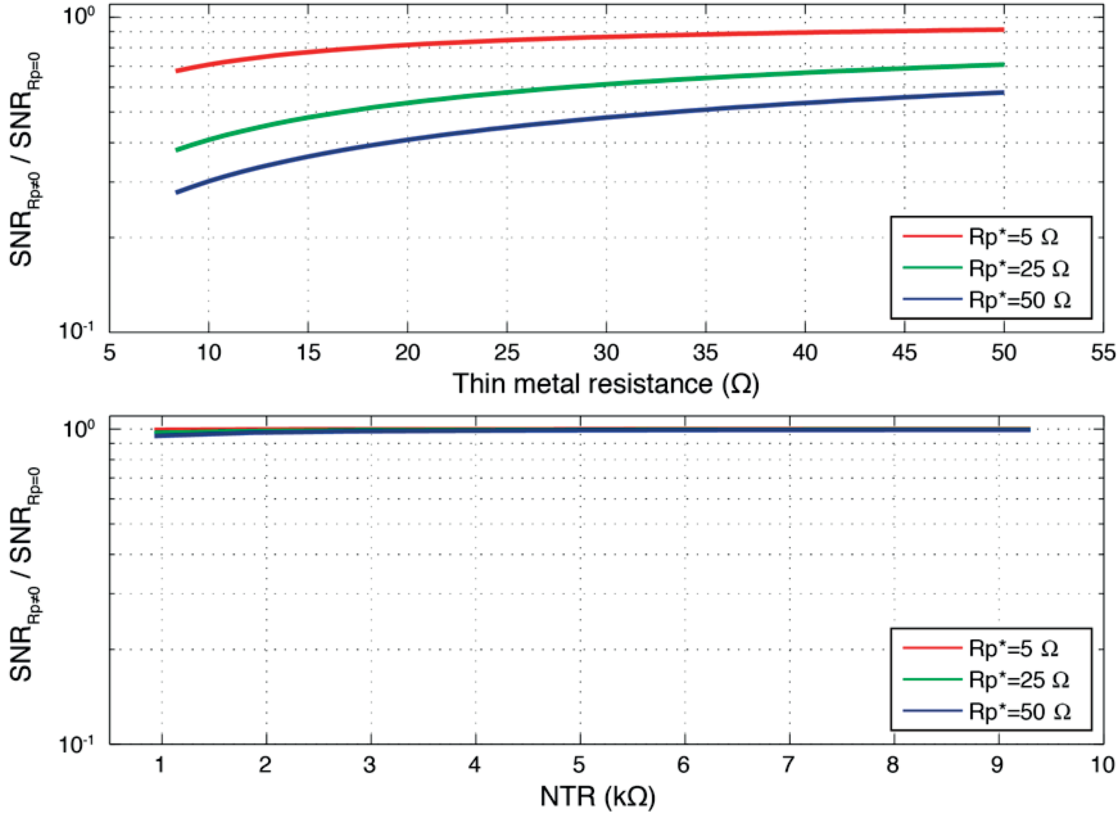

Figure 2.7: SNR loss in NTR and thin gold film readout due to parasitic resistances: **a)** $SNR\left(R_P \neq 0\right)/SNR\left(R_P = 0\right)$ for a thin gold film resistor. **b)** $SNR\left(R_P \neq 0\right)/SNR\left(R_P = 0\right)$ for a NTR, for several different values of connecting trace parasitic resistance.

Cantilever 5 was a locally released cantilever having size of only $1.5 \times 0.5 \times 0.1\,\mu m^3$. It was not applicable for AFM imaging, but it was successfully used to measure cantilever deflection (see Section 2.6.2). The fabrication process of these cantilevers is described in Section 2.6.1.

In order to perform imaging with NTR cantilevers, several measurement setups were made. For cantilever generations 1-3 (Figure 2.8) a custom-made cantilever holder (compatible with the Bruker MultiMode AFM head) was used for imaging, allowing simultaneous measurements and AFM imaging with both the OBD readout and the electrical readout. For cantilever generation 4 (Figure 2.8) a custom-made AFM head was used for imaging, which allowed simultaneous optical sensing of $20 \times 8 \times 0.3\,\mu m^3$ sized cantilevers. The AFM measurement setups and imaging procedure are explained in the following chapter.

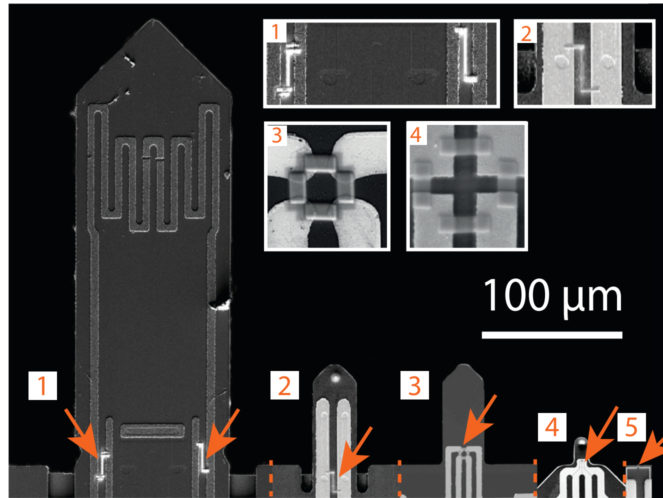

Figure 2.8: NTR sensors deposited on a variety of custom made AFM cantilevers spanning two orders of magnitude. Cantilevers 1-4 were fully released and were used in AFM imaging. Cantilever 5, (for zoom in see Figure 2.19a) was locally released and was deflected by a nanomanipulater to measure cantilever deflection.

2.5.1 AFM measurement setup and procedure

For the large NTR cantilevers (cantilevers 1-3 from Figure 2.8), AFM imaging and noise measurements were performed using a custom made cantilever holder (see Figure 2.9a-c). The cantilever holder was designed in order to enable simultaneous measurements with both the OBD and the electrical readout. A stack piezo actuator (PL022.30, Physik Instrumente, USA) was integrated in the holder to excite the cantilever resonance. The custom made electronics setup was used for electrical readout of the self-sensing cantilevers. The electrical readout consisted of a full Wheatstone bridge of piezoresistors located on the cantilever chip and subsequent amplification stages (see Figure 2.9d). The flexible printed circuit board (PCB) was used to provide signals to and from the cantilever chip. A low noise instrumentation amplifier AD8250 (Analog Devices, USA) was positioned on the flexible PCB, close to the cantilever chip to reduce noise and stray capacitances of the electrical lines. The rest of the amplification stages were located on the readout electronics PCB. An ultra-precision, low noise 2.048 V voltage reference ADR420 (Analog Devices, USA) was used to bias the Wheatstone bridge.

For the small NTR cantilevers (cantilever 4 from Figure 2.8), AFM imaging was performed using a custom-made electronics setup and custom-made AFM head (see Figures 2.10a-c). Details regarding the design of the AFM head are previously published in reference [119]. The custom-made AFM head allowed us to compare the self-sensing performance of the small $20 \times 8 \times 0.3\,\mu m^3$ sized NTR cantilevers to OBD readout.

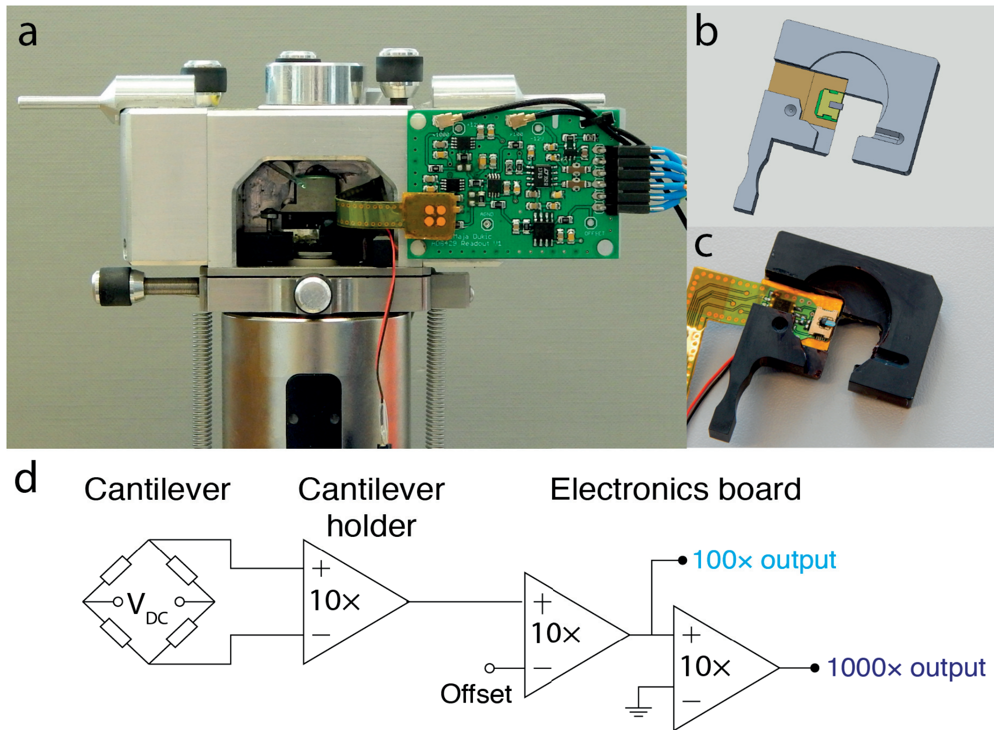

Figure 2.9: The AFM measurement setup for large self-sensing cantilevers: **a)** AFM head with the custom designed cantilever holder and readout electronics **b)** The design and **c)** an image of the cantilever holder designed for simultaneous measurements with both OBD and electrical readout. **d)** A schematic of the electrical readout.

A custom-made fluid-sealed cantilever holder allowed for imaging in both air and liquid environments (see Figure 2.10d). All connection lines on the cantilever and the PCB chip were fluid isolated, except for the NTRs themselves, which were in direct contact with fluid.

The electrical readout of the NTR cantilevers consisted of a full Wheatstone bridge of NTR resistors on the cantilever and subsequent amplification stages (Figure 2.10a). The first amplification stage, a low noise instrumentation amplifier (AD8250), was positioned in the AFM head close to the cantilever sensor to reduce noise and stray capacitances from the Wheatstone bridge electrical connections. A high precision 0.5/1 V voltage reference (ADR130) biased the bridge. The subsequent amplification stages were located in an electronics module below the standard Bruker MultiMode AFM base and were designed to intersect between the Bruker Nanoscope controller and the Bruker MultiMode AFM base (see Figures 2.10b-c).

For AFM measurements the DC offset of the Wheatstone bridge was first zeroed. The electrical and optical deflection signals were verified by a frequency sweep of the tapping

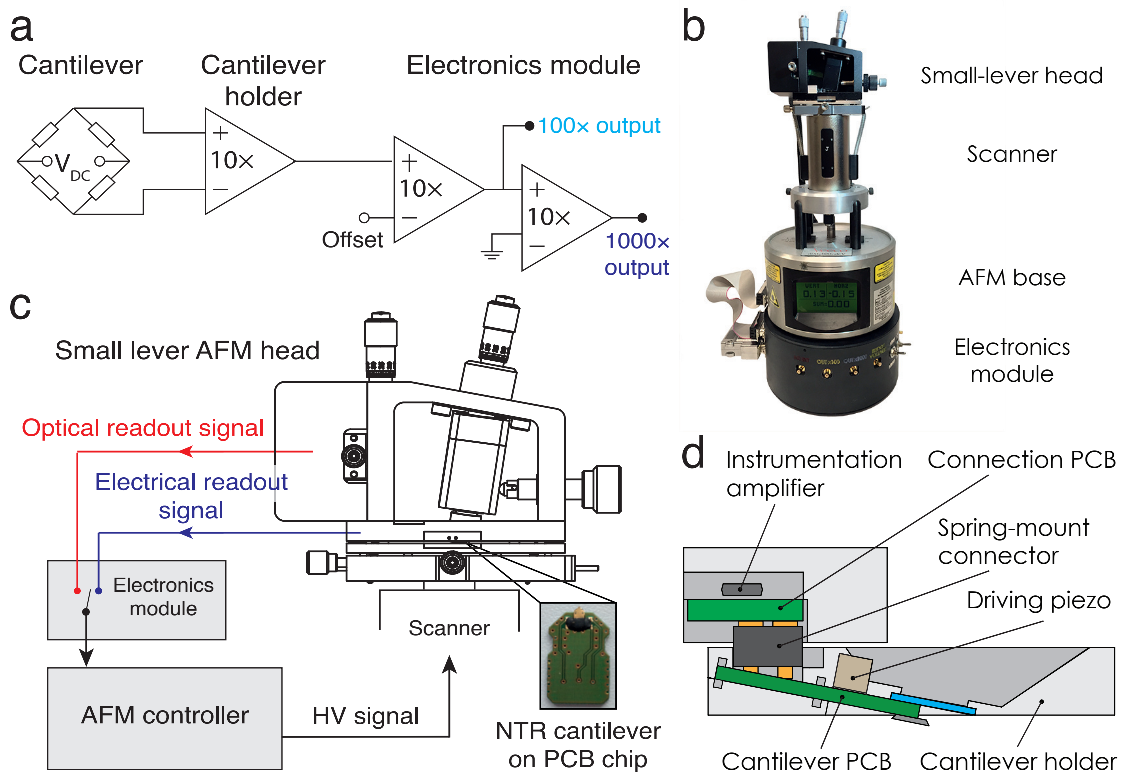

Figure 2.10: The AFM measurement setup for small self-sensing cantilevers: **a)** A schematic of the electronic readout. **b)** AFM measurement setup. **c)** A schematic of the AFM measurement setup for both optical and electrical readout. **d)** A schematic of the cantilever holder

excitation piezo; the appropriate working frequency was further confirmed via a thermal tune using OBD detection. Finally, appropriate cantilever free and setpoint oscillation amplitudes, gains and other imaging parameters were chosen.

2.5.2 AFM imaging

In order to test the functionality of the NTRs in a sensing application we have equipped a small, high-speed silicon nitride (SiN) AFM cantilever with a full Wheatstone bridge of NTR resistors (see Figure 2.11a). The full Wheatstone bridge readout cancels any NTR temperature-dependent effects, such as the influence of temperature on the NTR conductivity (with the conductivity temperature dependence given in Figure 2.2b). The active sensor length used was 500 nm. The dimensions of the AFM cantilevers ($20 \times 8 \times 0.3\,\mu m^3$) were chosen such that it was still possible to use a laser for comparison readout. Figure 2.11b shows the driven resonance curve measured with the NTR sensor (red). The optically detected thermomechanical tune is shown for reference (blue).

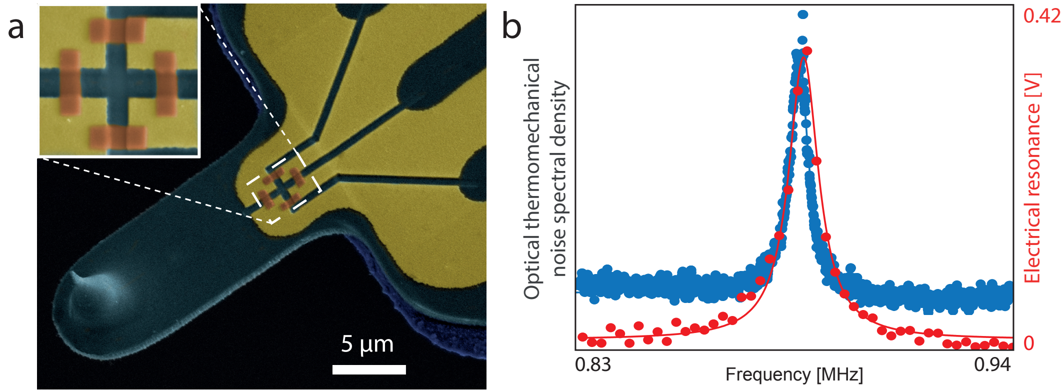

Figure 2.11: AFM cantilever incorporating NTR active readout. **a)** SEM image of the SiN AFM cantilever for dual readout (dimensions: $20 \times 8 \times 0.3\,\mu m^3$). Inset: NTR full bridge. **b)** Driven resonance curve measured with NTR sensor (red) and optical thermal spectrum (blue).

Figure 2.12 shows selected tapping mode AFM images of: a) atomically flat terraces in MICA, b) dried *Escherichia coli* bacteria on the MICA disc, c) rat-tail collagen fiber and d) custom made *EPFL* silicon test grating. All AFM imaging was performed using a commercial AFM system (Bruker MultiMode or Anfatec DS4). The NTR readout electronics were interfaced to either the standard MultiMode optical readout head, a custom-made MultiMode-compatible optical readout head for small cantilever deflection detection [119] or a custom-built Anfatec DS4-compatible tip scanner. The cantilever resonances were excited using sheet or stack piezoactuators. Sample preparation and imaging conditions were as follows: the MICA sample was lightly scratched with 1000 grit sandpaper and cleaned with a CO_2 snow cleaner. The AFM image was taken in air at 1.5 Hz scan rate and at 323 kHz resonance frequency. A droplet of *E. coli* suspension was dripped to a freshly cleaved MICA disc and left to dry. The AFM image was taken in air at 1 Hz scan rate and at 323 kHz resonance frequency. We obtained collagen from a rat tail tendon sample. The tendon was placed on a freshly cleaved MICA disk immersed in DI water. The tendon was pulled apart using sharp tweezers to spread the individual fibers across the MICA disc and left to dry at room temperature. The AFM image was taken in air at 0.5 Hz scan rate and at 419 kHz resonance frequency. The *EPFL* test grating AFM image was taken in air at 0.5 Hz scan rate and at 453 kHz resonance frequency.

The collagen fiber image shows the characteristic 67 nm periodic banding pattern. The image quality proves the applicability of the NTRs as strain sensors even for demanding applications such as AFM. However, in these measurements the noise floor of the electrically detected deflection was not thermomechanically limited due to the still relatively large cantilever size. At this cantilever size, optical detection methods are still superior since they measure angular deflection rather than strain.

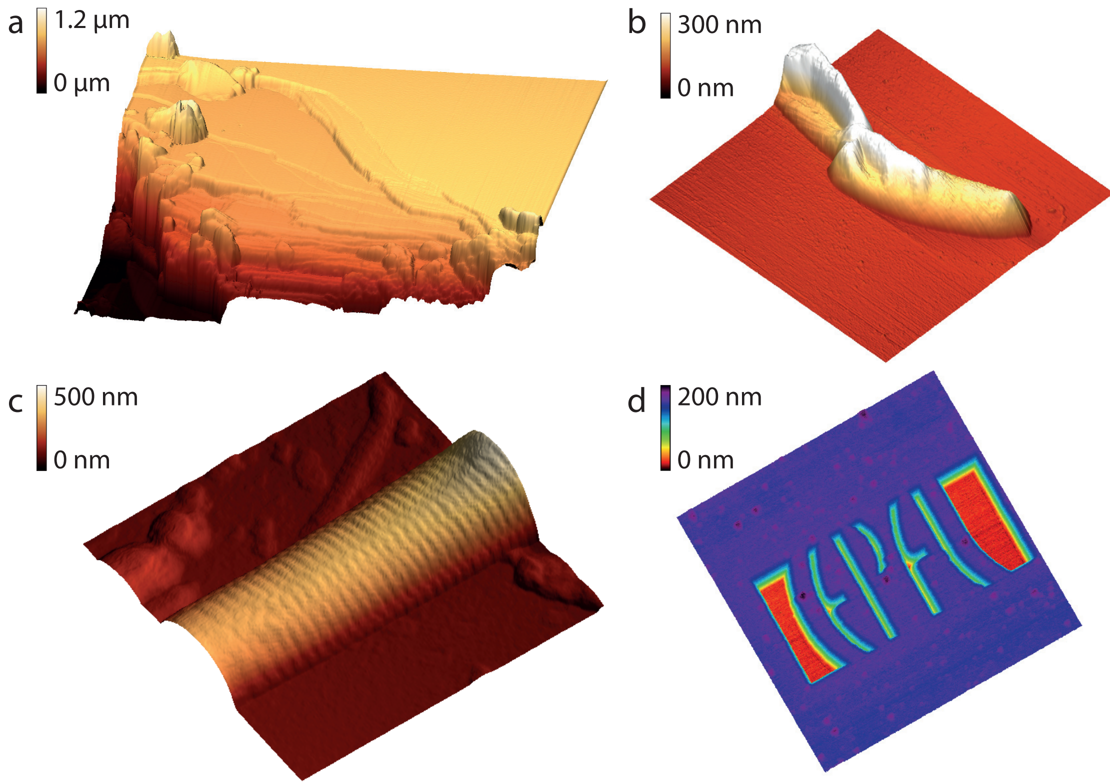

Figure 2.12: Selected AFM images obtained with the self-sensing NTR cantilevers in air. **a)** AFM image of atomically flat steps on scratched mica. Total scan size: $5 \times 5\,\mu m^2$. **b)** AFM image of dried *Escherichia coli* bacteria on the MICA disc. Total scan size: $4.7 \times 4.7\,\mu m^2$. **c)** AFM image of rat-tail collagen fibril showing the characteristic 67 nm spaced, 6 nm high banding pattern. Total scan size: $2.1 \times 2.1\,\mu m^2$. **d)** AFM image of custom made silicon *EPFL* test grating. Total scan size: $10 \times 10\,\mu m^2$

The small active sensor lengths also allow for the use of small bridge voltages of 0.1−0.5 V, while still giving sufficient readout signal. This in principle enables the use of the NTR sensors for measurements in fluid even without passivation. Figure 2.13a-b shows the comparison of the sensor noise of a cantilever operated in air vs. phosphate buffered saline (PBS). NTR resistors were tested in PBS for several hours and remained stable. However, the noise fluctuations in PBS were a factor of 2 higher than in air. We hypothesize this is due to the interaction of ions with the surface of the NTR, changing the effective dielectric properties of the medium adjacent to the NTR. This effect could be reduced through passivation of the NTR sensor element. Nevertheless, the NTR sensors remained stable in PBS for hours and we did not observe any degradation of the sensor. Figure 2.13c-d shows the comparison of the AFM imaging of NTR cantilever obtained in air vs. water. The AFM images of the silicon calibration grating (Bruker STR 10-1800P) were taken with the same cantilever, at 1 Hz scan rate and 913 kHz resonance frequency in air (Figure 2.13c) and 332 kHz resonance frequency in water (Figure 2.13d).

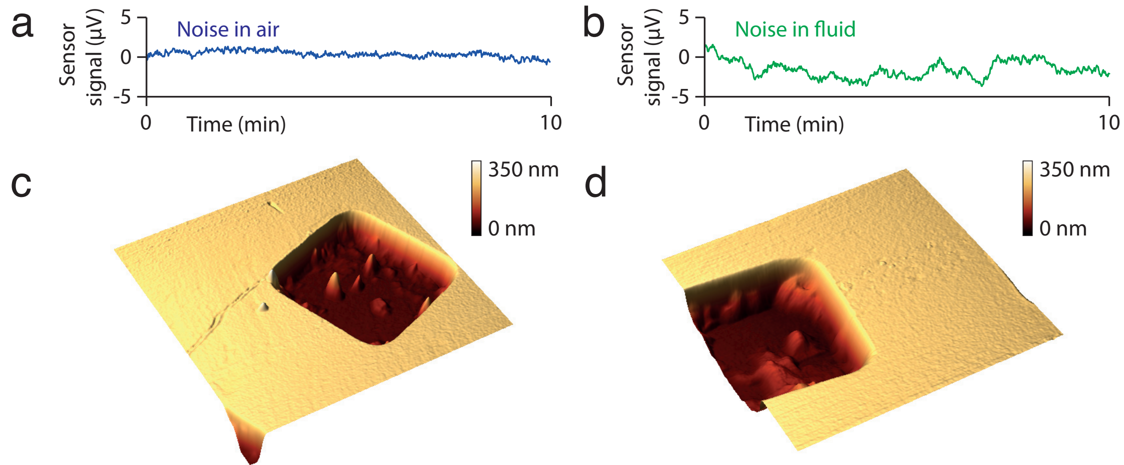

Figure 2.13: Noise of NTR sensor in **a)** air and **b)** PBS accompanied by AFM image of a silicon calibration grating obtained in **c)** air and d) water. Total scan size for both images: $10 \times 10\,\mu m^2$.

2.5.3 High-speed AFM imaging

We tested the imaging capabilities of the smallest NTR-sensing AFM cantilevers in terms of the speed. Figure 2.14 presents height (above) and amplitude error (below) AFM images taken at 1 Hz, 10 Hz and 20 Hz line rate using NTR sensing.

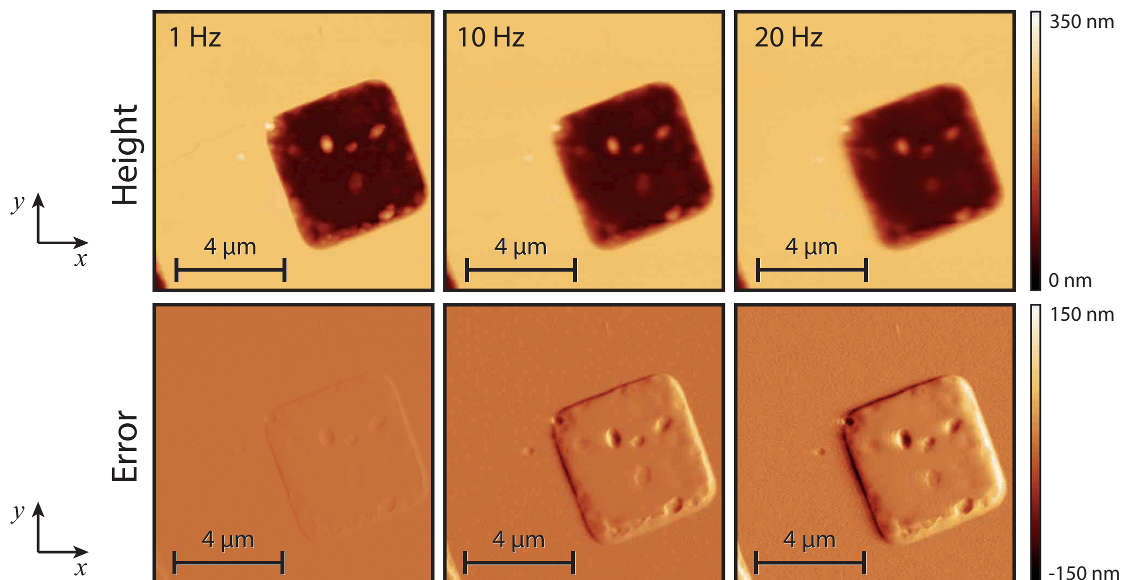

Figure 2.14: Imaging speed performance of NTR cantilevers: AFM images of a Si calibration grating recorded at 1 Hz, 10 Hz and 20 Hz line rate using NTR sensing. Above: height images, below: corresponding amplitude error images. The images are taken at 1024×1024 pixel resolution.

At these line rates, 1024 × 1024 pixel resolution and 10 µm scan size, imaging speed is already higher than what is achievable with conventional AFM cantilevers. As expected, image quality degrades slightly with an increase of the imaging speed: decrease in the amount of detail in the height image and increase of the error signal can be noticed. This effect can be better observed on the height and error cross sectional profile lines presented in Figure 2.15.

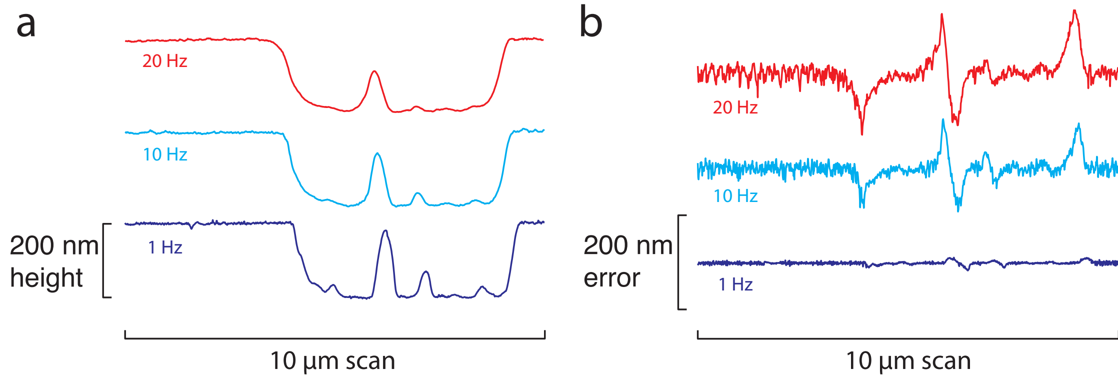

Figure 2.15: Cross sectional profile lines taken at the same y position, for different imaging speeds using NTR sensing readout. The lines are extracted from: **a)** height and **b)** amplitude error AFM images presented in Figure 2.14.

The limitation on the imaging bandwidth exists due to two factors: 1) The mechanical bandwidth of the cantilever and 2) the required integration time to reduce noise. The first factor is independent on the sensing mechanism (optical or NTR) and is purely a function of the cantilever geometry, material and environmental damping. We measured the mechanical bandwidth of the $20 \times 8 \times 0.3\,\mu m^3$ sized NTR cantilever using OBD readout (see Figure 2.16). The measurement procedure was similar as described in [41]. The measured bandwidth was around 6.5 kHz which is consistent with what one would expect for a cantilever of such dimensions.

The second factor is dominated by the noise of the overall readout (NTR sensor and readout electronics). Measured noise values using NTR sensing were around 3 nm and 7 nm, at 1 Hz and 10 Hz line rate, respectively. This is around two orders of magnitude higher than what is commonly achieved with an OBD readout. On the other hand, self-sensing cantilevers having noise levels comparable to optical readout were previously reported by Li et al. [91] for cantilever dimensions in the sub-micron range (using thin gold film strain sensors).

The fully released cantilever with a sharp tip we used for AFM imaging was $20 \times 8 \times 0.3\,\mu m^3$ in size, corresponding to the large cantilevers reported in [91] (with lengths in 10s of µm). We compared the noise densities reported in [91] with noise densities we

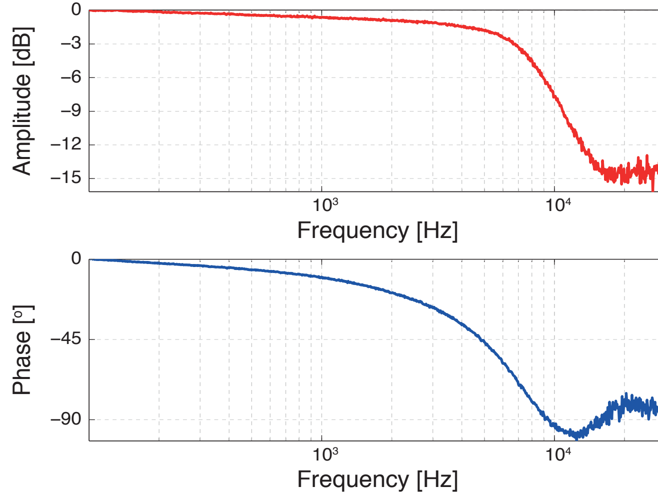

Figure 2.16: Cantilever mechanical bandwidth measurement: transfer function of the $20 \times 8 \times 0.3\,\mu m^3$ NTR cantilever in tapping mode. The amplitude curve reaches the $-3\,dB$ point at around 6.5 kHz. The amplitude setpoint was set to 65 % of the free amplitude.

achieved. We came to the conclusion that the noise levels of the cantilevers of similar dimensions are similar between NTR and thin gold. In the same fashion, with smaller cantilever dimensions the NTR performance improves. We calculated that below a cantilever length of $\sim 3\,\mu m$ (thickness 300 nm) the NTR sensors are expected to outperform optical detection given reasonably achievable electronic noise levels (see Appendix A.2).

2.6 Deflection sensing of the 500 nm wide NTR cantilevers

We wanted to demonstrate that NTR sensors can be used for sensing of sub-micron sized cantilevers, having cantilever dimensions below the conventional optical detection limit. With this goal, we designed chips with small-sized locally released cantilevers having various sizes ($3 \times 1\,\mu m^2$, $1.5 \times 0.5\,\mu m^2$ and $1 \times 0.3\,\mu m^2$, 100 nm thick).

2.6.1 Fabrication of locally released NTR cantilevers

A process flow was determined for locally released silicon nitride cantilevers incorporating NTR readout. The most important steps of the process flow are presented in Figure 2.17. Firstly, silicon nitride is etched to define the cantilever shape. Then, lift-off processes of thin Au film (NTR connecting electrodes) and thick Al film (contact traces) are performed. Afterwards, chips are protected and diced, and potassium hydroxide (KOH)

etching of silicon is performed in order to locally release the cantilevers. Finally, NTR sensor was deposited, where deposition as well as irradiation of an NTR was realized in less than 10 s.

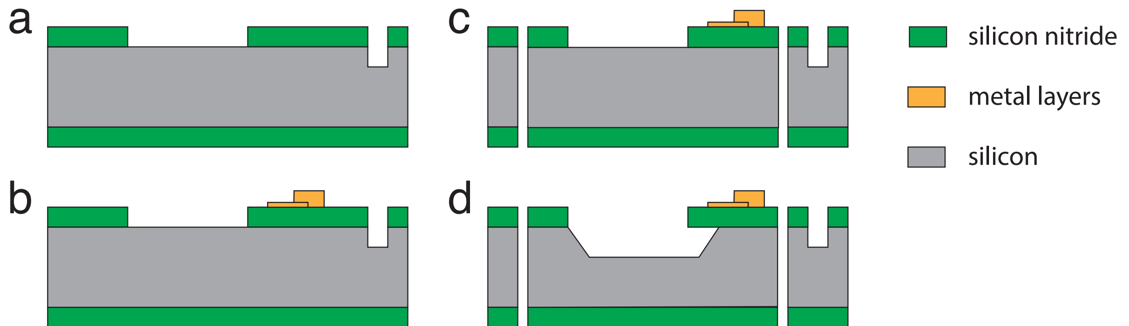

Figure 2.17: The most important steps in the process flow for locally released NTR cantilevers: **a)** silicon nitride dry etch **b)** metal lift-off **c)** dicing **d)** silicon KOH etch.

2.6.2 Deflection measurements

The static deflection measurements were performed by deflecting the NTR cantilever with a closed loop nanomanipulator system (SMARACT SLC1720-SL) integrated inside the electron microscope. To achieve sub-nm resolution for the deflection of the 500 nm wide NTR cantilevers, the cantilevers were mounted onto a piezoactuator and pushed against the overlaying nanomanipulator needle (see Figure 2.18).

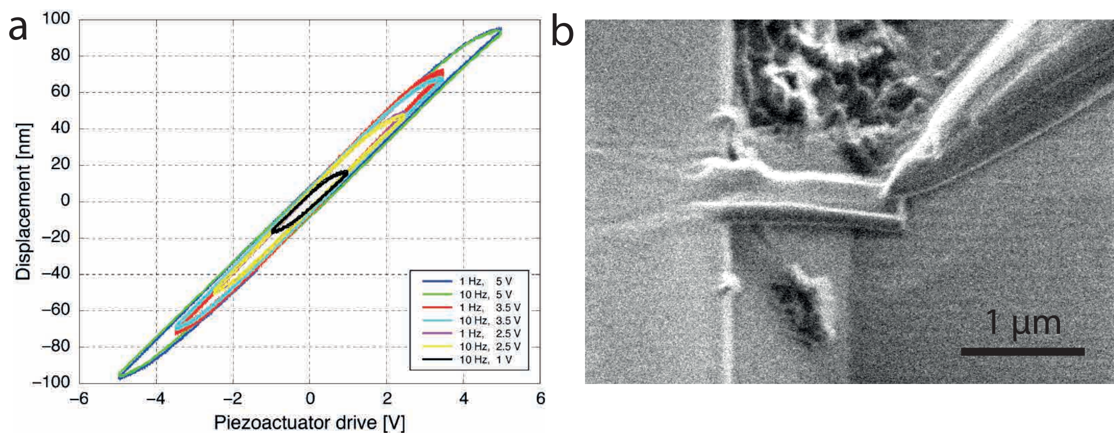

Figure 2.18: Deflection measurement setup for the smallest NTR cantilevers. **a)** Characterization of the stack piezoactuator hysteresis and sensitivity, for sub-nm resolution deflection measurements. Piezoactuator was characterized for different excitation voltage amplitudes and frequencies. Deflection sensitivity was around $\approx 20\,\mathrm{nm/V}$. **b)** A focused ion beam (FIB) image of the NTR cantilever being pushed against the overlaying nanomanipulator needle.

To demonstrate NTR sensing of the 500 nm wide cantilever (presented on Figure 2.19a), the relative change in resistance due to the deflection was measured (see Figure 2.19b) using a lock-in amplifier (Stanford Research SR830) and a Wheatstone bridge setup.

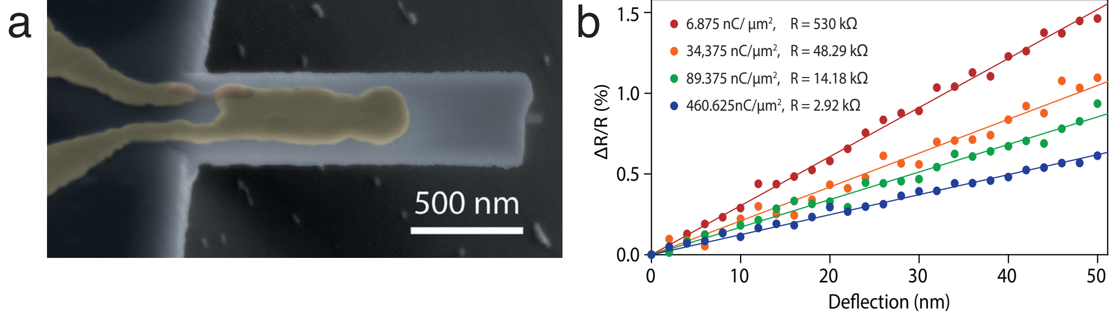

Figure 2.19: Deflection sensing of a 500 nm wide NTR cantilever: **a)** SEM image of a $1.5 \times 0.5 \times 0.1\,\mu m^3$ cantilever with NTR sensor. **b)** Dose dependent deflection curves of a 500 nm wide cantilever.

2.6.3 Apparent gauge factor

In order to estimate gauge factors of the NTR structure deposited on the $1.5 \times 0.5 \times 0.1\,\mu m^3$ silicon nitride cantilever, a finite element analysis simulation was performed in COMSOL Multiphysics (see Figure 2.20a). To calculate the strains in the structure, we estimated that the elastic modulus of the NTR is close to the Young's modulus of a diamond-like structure of amorphous carbon [129, 130]. Therefore, in simulations we assumed the Young's modulus for NTR of 760 GPa.

For irradiation doses in the range from $0 - 500\,nC/\mu m^2$, estimated gauge factor values were in the range of 2 - 5 (see Figure 2.20b). This range of values is lower than gauge factors measured for larger cantilevers and NTR structures (see Figure 2.5b). We suspect that this is due to several reasons:

1. Assumed values for the NTR Young's modulus might be off and we might have stronger stiffening effects of the cantilever.
2. If the NTR is too broad, a fraction of the current can directly flow from the left to the right electrode and not over the bending edge (see Figure 2.20c). For this part the resistance does not change during bending of the cantilever.
3. If the gold contacts are not located at the bending edge but are slightly offset back on the chip body, the effective change of resistance is reduced to $x/l_s \cdot \Delta R$ (see Figure 2.20d). This effect was incorporated in the COMSOL simulation. However it was difficult to estimate the exact position of the cantilever bending edge from the SEM cantilever image.

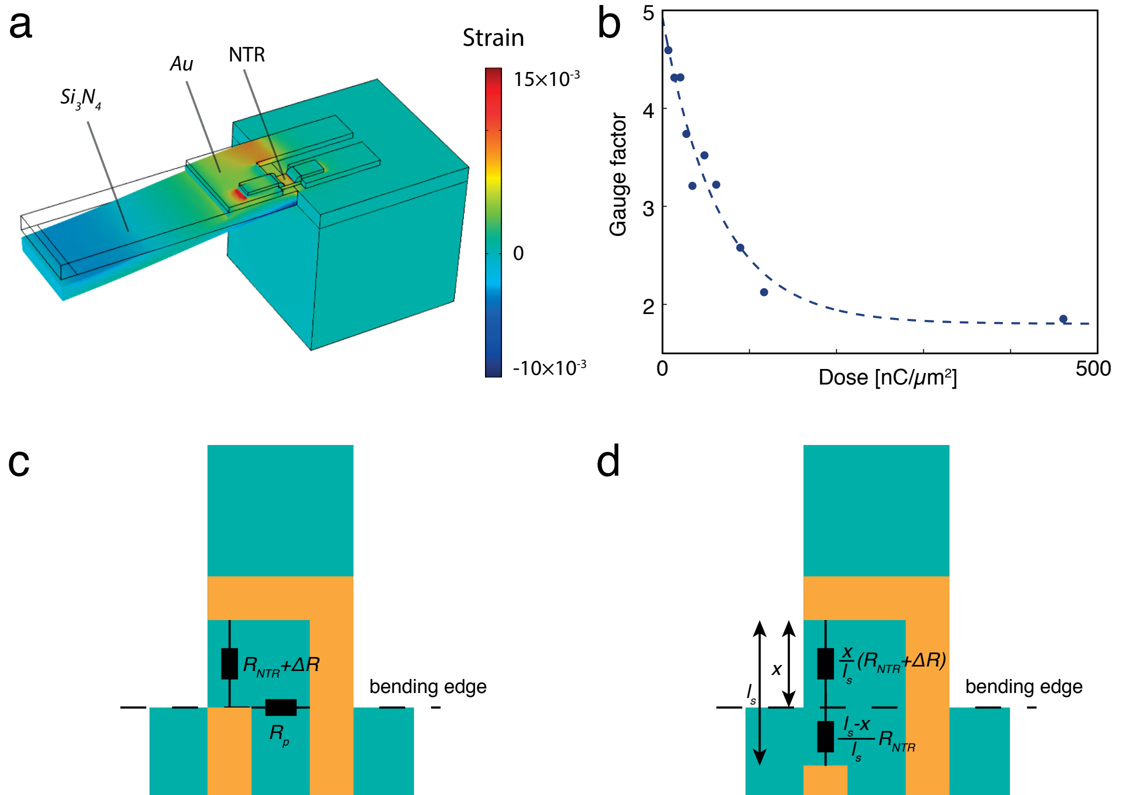

Figure 2.20: Gauge factor estimation of a small-sized NTR sensor. **a)** Strain distribution in the structure simulated in COMSOL for 50 nm cantilever deflection. Cantilever size: $1.5 \times 0.5 \times 0.1\,\mu m^3$, active NTR size: $150 \times 100 \times 20$ nm. **b)** estimated gauge factors from simulated strain in the structure and measured change of the relative resistance. **c)** and **d)**: possible scenarios for the reduction of the apparent NTR gauge factor: **c)** current flow directly from one electrode to another through parasitic resistance and **d)** misalignment of the gold contact electrodes, for which only part of the NTR acting as strain sensor.

2.7 Conclusion

The NTR 3D printing technology is extremely flexible in size, shape, substrate material as well as sensor operating environment. This makes it possible, for the first time, to add strain sensing on very small and thin devices, and on unconventional materials and in arbitrary shapes, and opens the door for a range of applications, from sensing of nanowire cantilevers for high-speed AFM to various 3D resonators. Although FEBID deposition is a serial process, where the sensors are written one at a time with an electron beam we have successfully implemented a semi-automated deposition of the NTR sensors, which makes larger scale fabrication viable.

While we have shown the use of NTR sensors for AFM cantilever sensing, the same sensor and rapid prototyping technology can also be used in cantilever based bio sensors, 3D MEMS and NEMS devices. Future research in NTR development could be focused on optimizing the gauge factor by investigating alternative metal precursors and dielectrics and deposition of NTR sensors on chemical vapor deposition grown Si nanowires [131] for use as ultra-high-speed AFM cantilevers. These cantilevers can have mechanical resonance frequencies two orders of magnitude larger (100 MHz) than cantilevers currently used in high-speed AFM. Such cantilever frequencies will be required for imaging the function of many molecular machines, which operate at timescales of 5 ms or less [21].

Chapter 3

Doped silicon piezoresistors in AFM

Of the methods proposed to detect cantilever deflection in atomic force microscopy (AFM) [3], the optical beam deflection (OBD) method [66, 132] remains predominant, due to its low noise, its reliability and its ability to use a variety of cantilever sensors. However, as it was mentioned in Section 1.4.1, OBD readout has certain limitations. The main limitation is, that due to the optical diffraction limit, only cantilevers with widths down to a few micrometres are usable for imaging. It is well-known that a reduction in cantilever size increases both sensitivity and detection speed [91, 106], and this diffraction limit presents a major barrier for the use of OBD readout with increasingly miniaturized cantilevers. On the other hand, as was mentioned in Section 1.4.2, strain-sensing techniques offer many advantages over OBD readout, such as a potential to detect submicron-sized cantilevers [91].

Most strain-sensing techniques have been applied on large cantilevers equally well suited for optical readout (with lengths in 100s of micrometres) or with cantilever dimensions optimized for force sensing and softer imaging. Although strain-sensing techniques are less suitable for force sensing, they are very well suited for achieving high topography resolution. These large piezoresistive self-sensing cantilevers even achieved low noise imaging [75, 77], although with low bandwidth and higher cantilever heating. With the continuing reduction of cantilever sizes to the range of tens of micrometres, the performance of strain-sensing methods in deflection sensing drastically increases.

We show both theoretically and experimentally that smaller size piezoresistive cantilevers permit AFM imaging with noise equal or lower than with OBD readout. We performed a comparison of the imaging noise achievable with the OBD and the piezoresistive readout, in an amplitude modulation AFM (AM-AFM) mode in air on a commercial AFM

system. At 20 kHz measurement bandwidth, with both readout techniques, we achieve a deflection noise of ≈ 0.3 Å, which is the noise level specified for the specific commercial AFM instrument used in measurements. Finally, we demonstrate that the piezoresistive cantilevers are suitable for nanometre and angstrom scale imaging of solid state samples or even biological samples in air, at standard AFM imaging scan rates. Research presented in this chapter was published in [133].

3.1 Introduction

In Section 1.4.1 and Section 1.4.2 we gave equations which provide dependence of cantilever angular change θ and longitudinal strain ε on cantilever free end deflection Δz, equations (1.4) and (1.5), respectively.

From equations (1.4) and (1.5), one can conclude that changing the cantilever length adjusts the sensitivity of both optical and piezoresistive readout. Specifically, a length decrease will increase the measured signal for a given displacement in both readouts. Figure 3.1 shows the relative change in $\tan(2\theta)$ and ε for varied cantilever length and thickness. A decrease in cantilever length has a much higher impact on piezoresistive readout performance than on OBD performance.

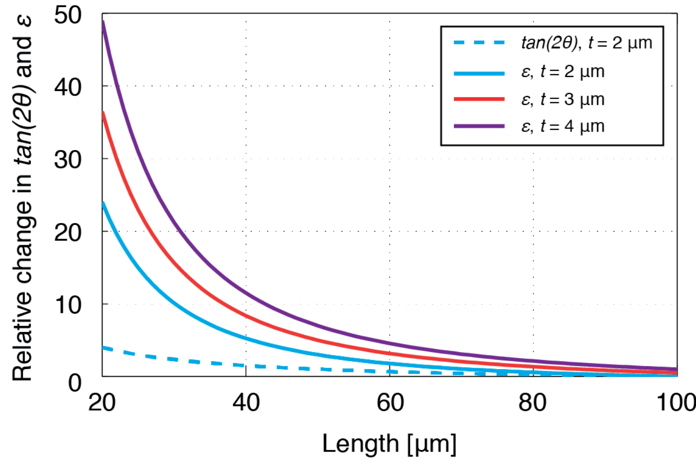

Figure 3.1: Effect of cantilever dimensions on the maximal bending angle (at $x = l$) and maximal strain (at $x = 0$) induced in the cantilever. The figure shows the relative change in cantilever bending angle: $\Delta \tan(2\theta(l))/\tan(2\theta(l_0))$, where $l_0 = 100\,\mu\text{m}$ and the relative change in generated strain: $\Delta\varepsilon(l,t)/\varepsilon(l_0,t_0)$, where $l_0 = 100\,\mu\text{m}$ and $t_0 = 2\,\mu\text{m}$. A decrease in cantilever length and increase in cantilever thickness will increase strain, and hence performance, of piezoresistive readouts by over an order of magnitude. At the same time, in OBD readouts, performance increase is only a few fold.

Additionally, from equation (1.5) we notice that increasing the cantilever thickness improves the deflection sensitivity of piezoresistive readout but does not affect the sensitivity of OBD readout. Based on the results in Figure 3.1, we conclude that decreasing the cantilever length and increasing the cantilever thickness significantly improve the deflection sensitivity of piezoresistive readout, but only marginally improve the deflection sensitivity of OBD readout. However, decreasing the length and increasing the thickness also strongly increases the cantilever spring constant. For AFM applications that require soft cantilevers, increasing the deflection sensitivity at the cost of a higher spring constant is not suitable. For AFM imaging applications such as AM-AFM mode in air however, high spring constants of 10s of N/m are used to overcome surface adhesion due to the absorbed water layer. In this application, miniaturized piezoresistive cantilevers can perform very well.

As we have seen from Figure 3.1, a reduction in cantilever size increases sensitivity much more in the favor of piezoresistive readout. In the next chapters we will show both theoretically and experimentally that this fact can be exploited to allow piezoresistive AFM imaging with the noise performance equal or better than in OBD readout.

Firstly, we make an analysis of dominant noise sources present in both OBD and piezoresistive readout and estimate deflection sensitivity and noise terms for each readout, in order to theoretically calculate the noise limits.

3.2 Noise sources and achievable MDD in AFM imaging

We classify noise sources in both OBD and strain-sensing readouts into three main groups: noise coming from the actual motion of the cantilever, noise coming from the measurement principle, and noise coming from the readout electronics. In each readout, these noise sources in combination determine the minimum detectable deflection (MDD), which is the deflection that causes the output voltage of the readout to be equal to the root mean square (RMS) voltage noise [134].

Brownian motion causes spontaneous oscillations in microcantilevers, such that each mode of the cantilever oscillation has the same average thermal energy $k_B T$ [135]. These thermal fluctuations are referred to as the thermomechanical noise. Figure 1.2a and Figure 1.3a indicate this noise with number 1. Butt and Jaschke [127] derived the mean

square deflection at the free end of the cantilever for each oscillating mode:

$$N_{th} = \frac{12}{\alpha_i^2} \cdot \frac{k_B T}{k} \underset{i=1}{=} 0.971 \cdot \frac{k_B T}{k} \tag{3.1}$$

where k is the cantilever spring constant, k_B is the Boltzmann constant, T is the temperature and α_i is a constant that is different for each oscillating mode. This noise scales slightly differently in piezoresistive and OBD readouts due to the measurement of displacement as an angle (OBD) or displacement as strain (piezoresistive), as will be explained in Section 3.2.1 and Section 3.2.2.

Noise coming from the measurement principle involves laser and photodiode noise for OBD readout and resistor noise for piezoresistive strain-sensing readout. Laser noise in OBD readout (labeled as number 2 in Figure 1.2a) comes from both fluctuations in the laser beam intensity and the spatial distribution, and from laser mode hopping [67, 136]. Photodiode shot noise (labeled as number 3 in Figure 1.2a) comes from statistical fluctuations in the number of photons emitted by the laser. For a well-designed system, this noise is usually dominant in OBD readout and it sets the lower limit for the deflection noise [67, 136]. The inherent noise for piezoresistive strain-sensing readout is the resistor noise in the Wheatstone bridge. It includes both $1/f$ and Johnson resistor noise (labeled as number 3 in Figure 1.3a). For the frequencies of interest in AM-AFM, Johnson noise usually predominates.

Finally, in both readouts there are also noise sources coming from the measurement electronics. In OBD readout electronics, the main noise sources are voltage and current noise of the transimpedance amplifier (labeled as numbers 4 and 5 in Figure 1.2a), the transimpedance feedback resistor noise (labeled as number 6 in Figure 1.2a) and the voltage divider noise (where the voltage divider is used in subsequent signal processing). In piezoresistive strain-sensing readout electronics, the main noise sources are noise of the bridge voltage reference (labeled as number 3 in Figure 1.3a) and the voltage and current noise of the differential amplifier (labeled as number 4 and 5 in Figure 1.3a).

In the following sections, we will derive expressions for MDD in both OBD and piezoresistive readout.

3.2.1 MDD in OBD readout

The overall deflection noise of OBD readout can be calculated by adding deflection power spectral densities (PSDs) of all relevant noise sources and then integrating this

sum over the frequency range of an AFM lock-in measurement bandwidth. To perform this calculation, the deflection sensitivity of the OBD readout method also needs to be determined in order to scale electrical noises from amperes to distance units.

The mean square deflection at the cantilever free end, for fundamental resonance mode, as seen with OBD readout is [127, 137, 138]

$$\widehat{z_1^2} = \frac{16}{3\alpha_1^2} \cdot \left(\frac{\sin\alpha_1 \sinh\alpha_1}{\sin\alpha_1 + \sinh\alpha_1} \right)^2 \cdot \frac{k_B T}{k} = 0.8175 \cdot \frac{k_B T}{k} \tag{3.2}$$

where k_B is the Boltzmann constant, T is the temperature and $\alpha_1 = 1.875$ for the first resonance mode. Equation (3.2) differs from equation (3.1) because OBD readout measures angular changes, rather than deflection, so the correction factor is introduced [127, 137, 138]. From equation (3.2) and the cantilever amplitude transfer function [139] we obtain the deflection noise PSD of the first resonance mode of the cantilever:

$$S_z(f) = 0.8175 \cdot \frac{4k_B T}{2\pi f_0 k Q} \cdot \frac{1}{\left(1 - \left(\frac{f}{f_0}\right)^2\right)^2 + \left(\frac{f}{f_0 Q}\right)^2} \tag{3.3}$$

where f_0 and Q are the cantilever fundamental mode resonance frequency and the quality factor, respectively. Assuming that we excite the cantilever oscillations at the frequency $f_e \cong f_0$ and that the lock-in measurement bandwidth is B, we obtain the power of the deflection noise coming from the thermomechanical noise [140, 141]:

$$N_{th,B} \cong 0.8175 \cdot \frac{2k_B T Q B}{\pi f_0 k} \tag{3.4}$$

In the OBD readout electronics, a transimpedance amplifier is commonly used as the first stage amplifier, to convert the photodiode current I_D to voltage. Noise sources present in this readout include the photodiode current shot noise $i_{N,D}$, the amplifier input referred current noise $i_{N,amp}$ and the feedback resistor noise $i_{N,R}$. These noise sources can all be treated identically as the current noise sources, which add onto the measured photodiode current [142]. These noise sources have the same gain, which is constant in the amplifier flat-band.

Additional noise source also present in the readout is the influence of the amplifier non-inverting input voltage noise $e_{N,amp}$. This noise, contrary to other noise sources, varies with frequency in the amplifier flat-band. $e_{N,amp}$ is multiplied by the amplifier's non-inverting closed loop gain $A_{CL}(f)$. The referred-to-input (RTI) voltage amplifier noise $e_{N,amp}$ sees the amplifier circuit as presented in Figure 3.2, where $Z_F = R_F \parallel C_F$ represents the total feedback impedance and C_S represents the total stray capacitance which

includes the photodiode capacitance, the amplifier input capacitance and other stray capacitances (e.g. such as the ones coming from the traces).

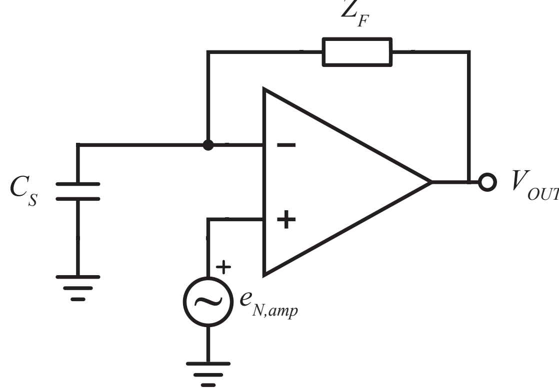

Figure 3.2: The amplifier circuit seen by the RTI amplifier voltage noise $e_{N,amp}$

If $A_{OL}(j\omega)$ is the amplifier open loop gain frequency response, then $e_{N,amp}$ is amplified by the amplifier's non-inverting closed loop gain:

$$A_{CL}(j\omega) = \frac{A_{OL}(j\omega)}{1 + \frac{A_{OL}(j\omega)}{1+j\omega C_S Z_F}} \tag{3.5}$$

In the amplifier flat-band we can assume that

$$A_{CL}(j\omega) \cong 1 + j\omega C_S Z_F \tag{3.6}$$

By substituting $Z_F = R_F/(1 + j\omega R_F C_F)$ in equation (3.6) and assuming $C_S \gg C_F$ we obtain

$$A_{CL}(j\omega) \cong \frac{1 + j\omega R_F C_S}{1 + j\omega R_F C_F} \tag{3.7}$$

From (3.7) we see that the closed loop gain transfer function has a zero at $f_z = 1/2\pi R_F C_S$ (where the gain starts to rise) and a pole at $f_p = 1/2\pi R_F C_F$ (where the gain levels off). For low frequencies $A_{CL}(f) \approx 1$ which will result in the input referred current noise of $e_{N,amp}/R_F$.

Finally, the total input referred current noise PSD of the transimpedance readout in the gain flat-band can be written as

$$N_i = 2eI_D + i_{N,amp}^2 + \frac{4k_B T}{R_F} + \left(|A_{CL}(j\omega)| \cdot \frac{e_{N,amp}}{R_F}\right)^2 \tag{3.8}$$

where e is an electron charge and R_F is the resistance of the feedback resistor. In equation (3.8) we take into account the entire current of the photo sensitive detector I_D but for the

rest of the noise sources we consider only noise sources coming from one transimpedance amplifier. Depending on the number of photodiode quadrants n_{PD} in the detector, the remaining noise terms need to be multiplied by n_{PD} to obtain the total readout noise. Finally, the current noise needs to be scaled to distance units by the deflection sensitivity (in nm/A units). The deflection sensitivity of the OBD readout is [136]

$$DS_{OBD} = \frac{\Delta z}{\Delta I} = \frac{la_0}{6\eta\chi\alpha P_0 l_f} \cdot \frac{1}{1 - \left(\frac{l_b}{2l}\right)^2} \tag{3.9}$$

where a_0 is the diameter of the short axis of the collimated laser beam, l_f is the focal length of the focusing lens, η is the efficiency of the light-to-current conversion at the photodiode, χ is the correction factor correcting for the assumed rectangular shape of the laser spot [136], P_0 is the laser power and α is the total laser power attenuation factor (coming from the optical path loss, the laser light spillage and the cantilever absorption). Finally, the total deflection noise or MDD of OBD readout equals to

$$n_{OBD} = \sqrt{N_{th,B} + DS^2_{OBD} \cdot B \cdot N_i} \tag{3.10}$$

In this section, we ignored laser noise sources for two main reasons: the laser intensity fluctuations are mostly eliminated by the differential amplifier present in the OBD readout electronics, and laser mode fluctuations that cause fluctuations in spatial distribution are very hard to estimate and strongly depend on the OBD setup [67].

Finally, in most cases the noise term coming from the photodiode shot noise will be the dominant one ($N_i \approx 2eI_D$) and for any well designed system it will determine the lower limit of deflection noise [67, 136]. Therefore, we used this assumption in the noise calculations.

3.2.2 MDD in piezoresistive readout

The deflection noise of piezoresistive strain-sensing readout can be calculated in similar fashion as was the case for the OBD readout. To perform this calculation, the deflection sensitivity of the piezoresistive readout method needs to be determined in order to scale the electrical noises from volts to distance units.

The mean square deflection at the free end of the cantilever for the fundamental resonance mode, as seen with piezoresistive readout is [128]

$$\widehat{z_1^2} = \frac{4}{3} \cdot \frac{k_B T}{k} \tag{3.11}$$

Equation (3.11) differs from equation (3.1) because piezoresistive strain-sensing readout measures changes in the induced strain, rather than deflection, so a correction factor is introduced. Assuming that we excite cantilever oscillations at a frequency $f_e \cong f_0$ and that the lock-in measurement bandwidth is B, we obtain the power of the deflection noise coming from the thermomechanical noise:

$$N_{th,B} = \frac{4}{3} \cdot \frac{2k_B TQB}{\pi f_0 k} \tag{3.12}$$

The PSD of the piezoresistor Johnson noise, from the Wheatstone bridge is $N_w = 4k_B TR$. Johnson noise coming from the differential amplifier is

$$N_{amp} = e^2_{N,amp} + \frac{i^2_{N,amp} R^2}{2} \tag{3.13}$$

where $e_{N,amp}$ and $i_{N,amp}$ are the input-referred Johnson voltage and current noise of the amplifier. Finally, some of the noise coming from the bridge voltage reference will affect the readout, where the level of the influence depends on the common mode rejection ratio (CMRR) of the differential amplifier. The PSD of the bridge voltage reference noise, referred to the amplifier input is

$$N_{ref} = \frac{n^2_{ref}}{4 \cdot 10^{CMRR_{dB}/10}} \tag{3.14}$$

where $CMRR_{dB}$ is the amplifier CMRR expressed in decibels and n_{ref} is the voltage noise spectral density of the bridge voltage reference. Usually, with a well-chosen differential amplifier and a low noise bridge reference (e.g. such as battery), this noise term is negligible. The total electrical noise PSD is then

$$N_v = N_w + N_{amp} + N_{ref} \tag{3.15}$$

In order to calculate the total deflection noise, the electrical noise needs to be scaled by the deflection sensitivity (in nm/V units, calculated for the case of two active resistors on the cantilever) [104, 128, 143]

$$DS_{PIEZO} = \frac{\Delta z}{\Delta V} = \frac{4}{3} \cdot \frac{l^2}{E\,(t - t_s)\left(1 - \frac{l_s}{2l}\right)} \cdot \frac{1}{\pi_l V_B} \tag{3.16}$$

where l and t are the cantilever length and thickness, l_s and t_s are the piezoresistor length and thickness, E is Young's modulus of the cantilever material, along its length, π_l is the longitudinal piezoresistive coefficient, and V_B is the bridge supply voltage. Finally,

total deflection noise or MDD of the piezoresistive readout equals to

$$n_{OBD} = \sqrt{N_{th,B} + DS^2_{PIEZO} \cdot B \cdot N_v} \tag{3.17}$$

3.3 Noise measurement in AFM imaging

We measured our AFM system noise for the same cantilever using both OBD and piezoresistive readout. The cantilevers used in the measurements were $300 \times 100\,\mu m^2$ and $70 \times 30\,\mu m^2$ sized piezoresistive silicon cantilevers (PRSA and PRS probes, SCL-Sensor.Tech. Fabrication GmbH, Austria) presented in Figure 3.3a-b. These cantilevers have a thickness from $4-6\,\mu m$ and a resonance frequency around 80 kHz ($300\times100\,\mu m^2$) and 850 kHz ($70 \times 30\,\mu m^2$). The measured mechanical bandwidth of these cantilevers is around 0.8 kHz ($300 \times 100\,\mu m^2$) and 3 kHz ($70 \times 30\,\mu m^2$). We performed all measurements using a Bruker MultiMode 8 AFM system. We custom-made a cantilever holder enabling simultaneous optical and electrical readout to adapt into the MultiMode AFM head.

The measurement setup used was the same as described in Section 2.5.1, used for sensing of the large NTR cantilevers (see Figure 2.9), with only difference in instrumentation amplifier used (AD8429, Analog Devices, USA). Two active piezoresistors integrated on the cantilever body and two passive piezoresistors integrated on the cantilever chip formed a Wheatstone bridge used for piezoresistive readout. The bridge resistance was around $1\,k\Omega$, for both large ($300\times100\,\mu m^2$) and small ($70\times30\,\mu m^2$) sized cantilevers. A 2 V input voltage was supplied to the bridge. The output signals from the bridge were sent to a low noise instrumentation amplifier and afterwards signal was amplified by additional amplification stages. The total amplification gain of the measured electrical signal is switchable to either 100 or 1000. The amplified signal was input to the Bruker AFM Nanoscope controller as the deflection signal at the IN0 input of the signal access module. The backside of the silicon cantilevers was sufficiently reflective for OBD measurements such that no reflective coating was required.

We characterised the RMS AFM imaging noise using 2D "noise images" in AM-AFM mode with each cantilever, using both the OBD and piezoresistive readout. In order to obtain the 2D "noise image", we performed the following procedure: first, we set the AFM image scan size to a value small enough that the tip can be considered as not moving and that there is no change in the surface topography (e.g. 0.01 nm). Then, the proportional and integral gains of the AFM proportional-integral (PI) controller were

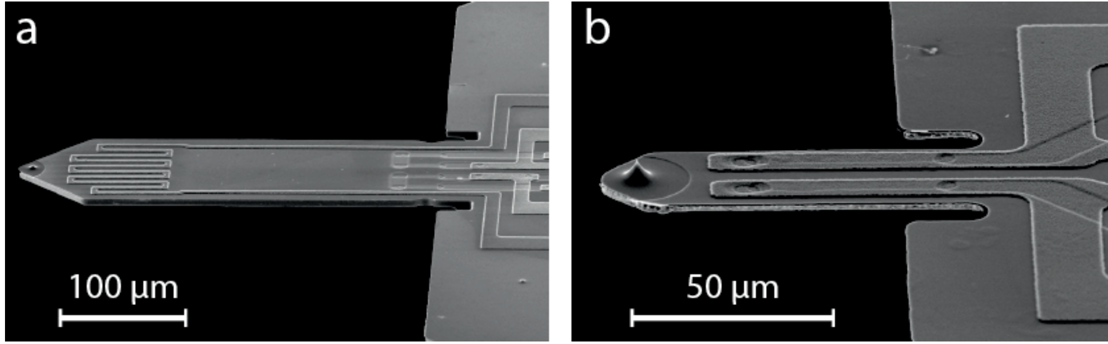

Figure 3.3: SEM images of representative **a)** $300 \times 100\,\mu m^2$ and **b)** $70 \times 30\,\mu m^2$ silicon piezoresistive cantilevers used for noise measurements and AFM imaging. **a)** The large-sized piezoresistive cantilever has a meander-like patterned heater resistor for thermal actuation (close to the free end, not used in measurements) and two active piezoresistors (close to the fixed end). **b)** The small-sized piezoresistive cantilever has two active piezoresistors along its length.

set to a very small value, just to prevent the cantilever from drifting off the surface. As the gains are set so low, almost the entire signal obtained from the "surface topography" is present in the amplitude error image. Since we consider that there is no change in surface topography, we can assume that the entire amplitude error signal actually represents noise present in the system. The amplitude error images taken in volts are scaled by the measured amplitude sensitivity parameter in order to obtain a 2D image of the noise in distance units. Using AFM image processing software [144] and processing the distribution of the pixel heights in the 2D noise image an RMS value of the noise was derived. Figures 3.4a and 3.4c present the noise images, and Figures 3.4b and 3.4d presented the corresponding noise histograms.

For the large-sized cantilevers ($300 \times 100\,\mu m^2$), we used a lock-in measurement bandwidth of 4.8 kHz, a free amplitude of 50 nm and an amplification gain for the piezoresistive readout of 1000. Such large amplitude was necessary as these cantilevers exhibit a very strong long-range damping and high surface adhesion. For the small-sized cantilevers ($70 \times 30\,\mu m^2$) we used a lock-in measurement bandwidth of 20 kHz, a free amplitude of 20 nm and an amplification gain for the piezoresistive readout of 100. As expected, the imaging noise of the large-sized cantilevers with the piezoresistive readout was several times higher (around 1 Å) than it was with the OBD readout (0.25 Å). On the other hand, the imaging noise of the small-sized cantilevers measured with the piezoresistive readout was 0.32 Å, while the noise obtained with the OBD readout was 0.35 Å. Therefore, at the measurement bandwidth of 20 kHz we achieved with both readouts a deflection noise $\approx$ 0.3 Å, which is the Z noise level specified for the Bruker MultiMode 8 AFM using AM-AFM mode in air at zero scan size [145]. To verify these results, we performed noise measurements with several small-sized cantilevers.

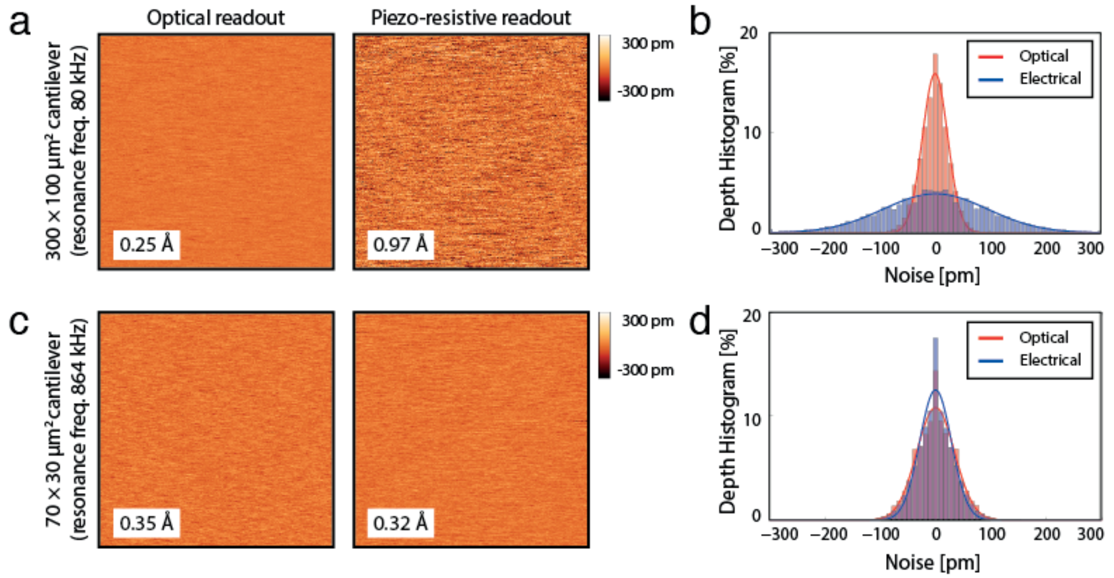

Figure 3.4: Noise measurements with OBD and piezoresistive readout. $300 \times 100\,\mu m^2$ piezoresistive cantilever: **a)** Deflection noise measured with OBD and piezoresistive readout and **b)** the corresponding noise histograms. $70 \times 30\,\mu m^2$ piezoresistive cantilever: **c)** Deflection noise measured with the OBD and piezoresistive readout and **d)** the corresponding noise histograms.

3.4 Low-noise AFM imaging with piezoresistive readout

In order to show image quality achievable with piezoresistive readout, we used small-sized piezoresistive cantilevers to image several AFM samples with very low topography features (see Figure 3.5a-c). We obtained all AFM images using AM-AFM imaging mode in air at 1 Hz scan rate. Figure 3.5a presents an AFM image of a collagen fibril showing the characteristic 67 nm spaced bending pattern. The collagen fibril corrugation depth is only a few nanometres. Figure 3.5b presents an AFM image of a housefly eye corneal surface pattern, showing maze-like features of only ~ 10 nm height. Figure 3.5c presents an AFM image of a highly ordered pyrolytic graphite (HOPG) showing graphite atomic steps. We chose a topography line (see Figure 3.5c, the dashed green line), averaged over 50 neighbouring pixel lines, whose profile is presented in Figure 3.5d. The line profile clearly shows topography steps of 3.3 Å, which corresponds to distance between HOPG atomic layers, which is 3.354 Å.

We performed AFM imaging using a custom made piezoresistive cantilever holder with readout electronics (see Section 2.5.1, Figure 2.9) in combination with a commercial AFM system (Bruker MultiMode 8). The images were taken with cantilevers having resonance frequencies in the range of $840 - 860$ kHz. We extracted collagen from a rat tail tendon as described in Section 2.5.2. To prepare the corneal sample from a captured housefly, we

dissected the head from the body with a scalpel, and afterwards an eye from the head in the same fashion. We used a scalpel to break the eye into several pieces, and some pieces were attached to an AFM sample disc via double-sided sticky tape. A freshly cleaved HOPG sample was prepared by cleaving a block of HOPG (PFQNM-SMPKIT-12M, Bruker, USA) with a sticky tape.

AFM images were processed using Gwyddion [144]. We used standard AFM image processing steps: levelling sample tilt by plane subtraction, removing scanner bow by 2D polynomial fitting, line-by-line matching of height median and line-by-line linear fitting. Lastly, images are presented as pseudo-three-dimensional images.

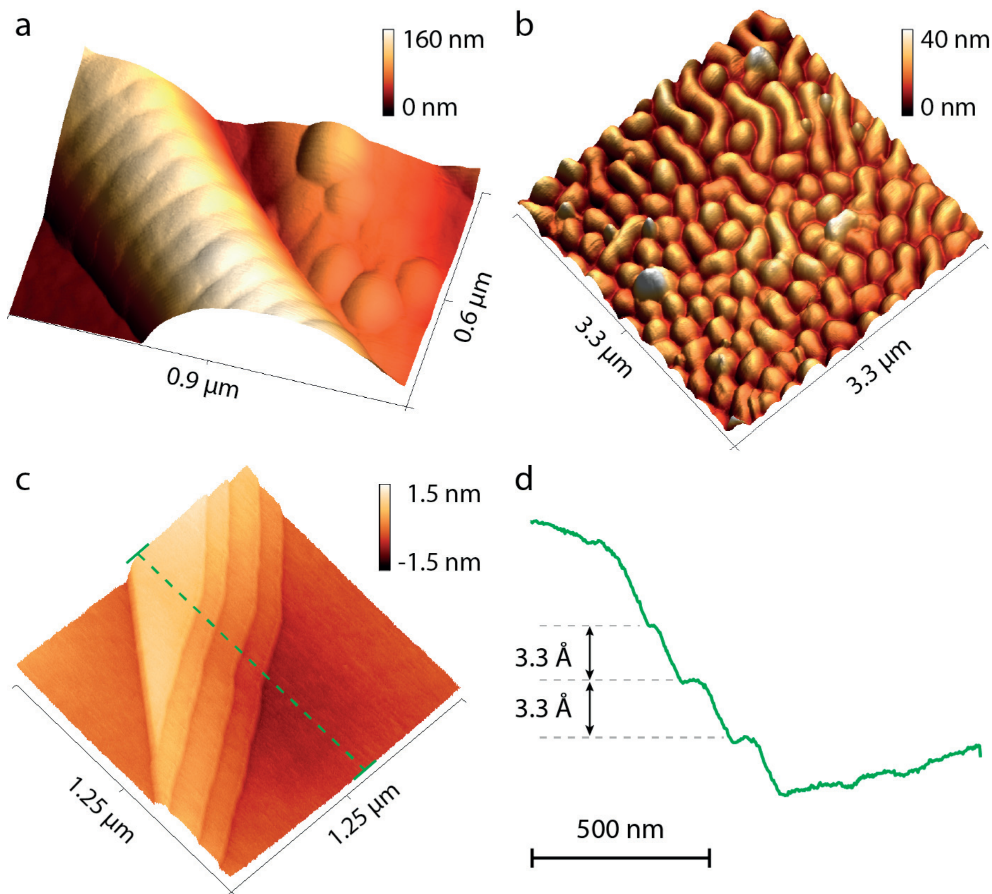

Figure 3.5: AFM images of biological and solid state samples obtained using piezoresistive readout. **a)** An AFM image of a collagen fibril showing the characteristic 67 nm spaced bending pattern. **b)** An AFM image of a housefly eye corneal surface pattern showing $\sim$ 10 nm high features **c)** An AFM image of a graphite (HOPG) surface, showing atomic steps. **d)** The selected topography line (averaged over 50 neighbouring pixel lines) demonstrates discernible topography steps of 3.3 Å, which corresponds to distance between HOPG atomic layers.

3.5 Impact of the cantilever dimensions on MDD

We performed theoretical calculations of the MDD achievable with both readouts, depending on the cantilever dimensions. The total deflection noise or MDD in both readouts can be expressed as

$$MDD = \sqrt{(CF \cdot N_{th} + DS^2 \cdot N_{el}) \cdot B} \tag{3.18}$$

where N_{th} is the on-resonance thermomechanical noise power spectral density (PSD), CF is a correction factor determined for each readout (see Section 3.2.1 and Section 3.2.2 for details); DS is the deflection sensitivity of the readout (in units of distance per Volts or distance per Amperes); N_{el} represents the entire electrical noise PSD (coming from both measurement principle noise terms and the readout electronics), and B is the lock-in measurement bandwidth, usually set close to the mechanical bandwidth of the cantilever B_{CNT}.

3.5.1 Estimated parameter values for MDD calculations

Although in AM-AFM mode the amplitude sensitivity, rather than deflection sensitivity should be used for scaling of the electrical noise N_{el}, we assume that for stiff samples in air the deflection and amplitude sensitivity have very close values [146–148]. This assumption applies to the exact imaging conditions we propose for piezoresistive readout.

All terms in equation (3.18) depend on the cantilever geometry, except for N_{el}, which remains constant. We estimated the influence of cantilever dimensions on the MDD and on the individual terms in equation (3.18), for both readouts (see Figure 3.6a-d).

We compared the piezoresistive readout noise for small-sized cantilevers to the noise performance of a custom AFM head designed for OBD AFM imaging with small-sized cantilevers [119]. For the case of the OBD readout, parameters used in calculation are given in Table 3.1. All calculations were performed for room temperature $T = 23\,°\mathrm{C}$. We assumed that photodiode shot noise limits the total electrical noise of the OBD readout. We performed the noise calculations for the OBD readout using a procedure similar to that of Fukuma et al. [136], explained in detail in Section 3.2.1.

For the case of piezoresistive readout we used the parameters estimated for $70 \times 30\,\mu\mathrm{m}^2$ sized piezoresistive silicon cantilevers (PRS probes, SCL-Sensor.Tech. Fabrication GmbH, Austria), which are presented in Table 3.2. These cantilevers have two active and two

Table 3.1: Estimated OBD readout parameters

Parameter	**Value**
Laser spot width: w_b [µm]	5.8
Laser spot width: l_b [µm]	18
Lens focal length: l_f [mm]	4.6
Diameter of the collimated laser beam: a_0 [mm]	2.5
Laser power: P_0 [mW]	3
Photodiode responsivity: η [A/W]	0.42
Laser light optical path loss attenuation factor: α_1	0.8
Laser light spillage attenuation factor: α_2	$erf\left(2\sqrt{2}w/w_b\right)$
Laser light Si absorption attenuation factor: α_3	0.35
Total laser light attenuation factor: α	$\alpha_1 \cdot \alpha_2 \cdot \alpha_3$
Transimpedance feedback resistance: R_F [kΩ]	20

passive p-type Boron doped piezoresistors which form a Wheatstone bridge. The differential amplifier used in the calculations was the low noise instrumentation amplifier AD8429 (Analog Devices, USA), set to a gain of 10. This amplifier was also used in the noise measurements and AFM imaging. All calculations were performed for room temperature $T = 23\,°C$.

Table 3.2: Estimated piezoresistive readout parameters

Parameter	**Value**
Active piezoresistor length l_s [µm]	40
Piezoresistor width: w_s [µm]	5
Piezoresistor thickness: t_s [µm]	1
Doping concentration: $c\left[1/\mathrm{cm}^3\right]$ [149]	8.5×10^18
Piezoresistor resistance: ρ_R [Ω cm]	0.01
Longitudinal piezoresistive coefficient: π_l [/Pa] [150]	4.72×10^{-10}

The noise calculations using the piezoresistive readout were performed using a procedure similar to one derived in [104, 128, 143], explained in detail in Section 3.2.2. In the calculations, we explored various cantilever sizes while keeping the piezoresistor dimensions and the doping properties constant. We varied the cantilever length from 50 to 300 µm with a constant length-to-width ratio at = 70/30. We performed the calculations for three chosen cantilever thicknesses: 4 µm, 5 µm and 6 µm.

In the calculations, we estimated the cantilever mechanical bandwidth as $\pi f_0/Q$ where f_0 and Q are the first mode resonance frequency and the quality factor, respectively. f_0

was calculated as [135]

$$f_0 = \frac{1.875^2}{2\pi} \cdot \frac{t}{l^2} \cdot \sqrt{\frac{E}{12\rho}} \tag{3.19}$$

where l and t are the cantilever length and thickness, E is the Young's modulus of the cantilever material along the cantilever length and ρ is the cantilever material density. The quality factor Q in air was calculated as [151, 152]

$$Q = \frac{4\rho t w f_0}{6\eta + 3w\sqrt{\eta\,(M/RT)\,\pi f_0 p}} \tag{3.20}$$

where w is the cantilever width, R is the gas constant, and η, M, T and p are air dynamic viscosity, molar mass, temperature and pressure, respectively.

3.5.2 Calculated MDDs and noise terms

Figure 3.6a presents the on-resonance thermomechanical noise power spectral density of the cantilever free end N_{th}, for a range of different cantilever dimensions. N_{th} decreases for smaller lengths and larger thicknesses, corresponding to the cantilever geometries preferred for strain-sensing. Figure 3.6b presents the deflection sensitivity of the OBD readout and the piezoresistive readout. A dashed line indicates the OBD deflection sensitivity DS_{OBD} which does not depend on the cantilever thickness. Three solid lines show the piezoresistive deflection sensitivity DS_{PIEZO}, for three different cantilever thicknesses. Both deflection sensitivities are referred to the input of the first amplifying stage (the output of the photodiode for the OBD readout and the output of the Wheatstone bridge for the piezoresistive readout).

Lower values of the deflection sensitivity (distance units per Volts or Amperes) correspond to better performance of the readout. From Figure 3.6b, we see that deflection sensitivity will improve with the cantilever length decrease, for both readouts. However, length decrease improves DS_{PIEZO} more significantly than DS_{OBD}. In addition, increasing the cantilever thickness further improves the performance of the piezoresistive readout.

The cantilever mechanical bandwidth B_{CNT} (estimated as $\pi f_0/Q$) increases with shrinking cantilever dimensions (see Figure 3.6c). A cantilever with higher B_{CNT} will respond more quickly to topography changes and allow for faster AM-AFM imaging. A higher B_{CNT} will also allow for a higher lock-in measurement bandwidth B. Although this permits faster AM-AFM detection, a higher B also increases the deflection noise. However, if faster scanning is not required, choosing a lower measurement bandwidth will decrease the imaging noise.

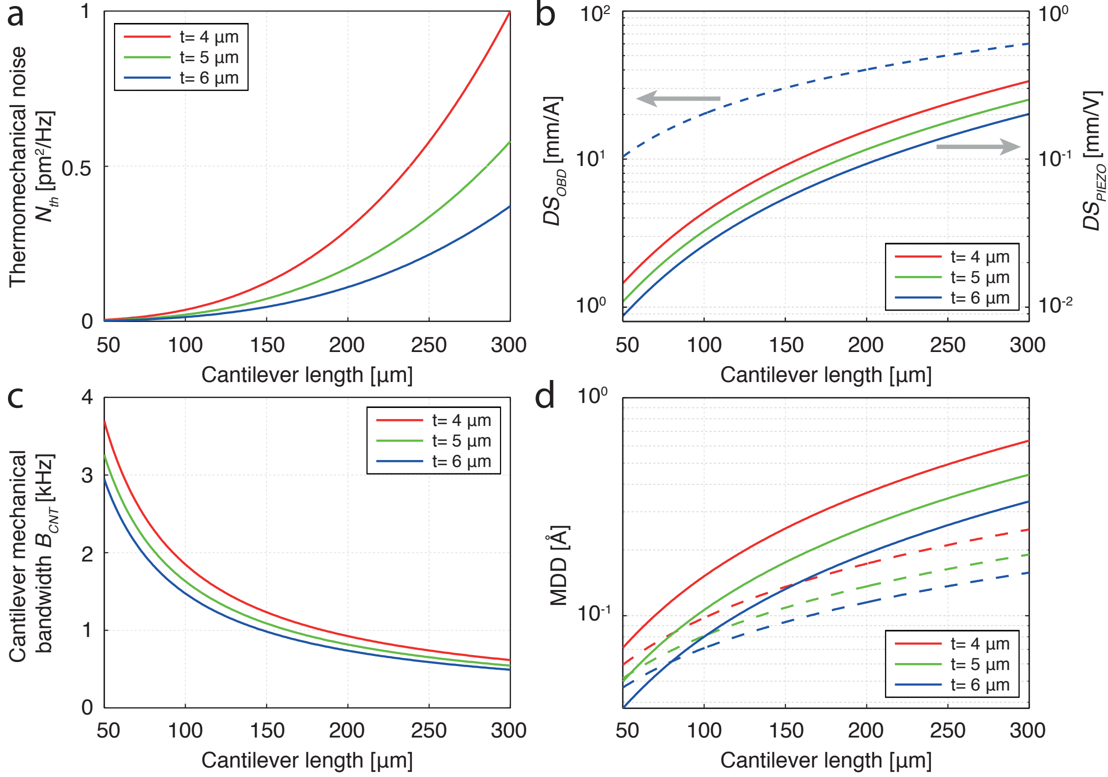

Figure 3.6: The effect of cantilever dimensions on terms contributing to deflection noise and achievable MDD, for both OBD and piezoresistive strain-sensing readout. **a)** On-resonance thermomechanical noise power spectral density of the cantilever free end irrespective of detection method. **b)** Deflection sensitivity of the OBD readout DS_{OBD} (dashed line, left axis in mm/A) and the piezoresistive readout DS_{PIEZO} (full lines, right axis in mm/V). DS_{OBD} is independent of the cantilever thickness. **c)** The cantilever mechanical bandwidth, estimated as $\pi f_0/Q$. **d)** A comparison of the theoretically achievable MDD, with OBD readout (dashed line) and piezoresistive readout (full lines), for several different cantilever thicknesses over the defined length range. The length-to-width ratio used is 70/30.

Even for a lock-in measurement bandwidth B set close to B_{CNT}, the overall achievable MDD still decreases with a decrease of the cantilever length (see Figure 3.6d). The results presented in Figure 3.6d suggest a set of cantilever dimensions, at which point the piezoresistive strain-sensing readout MDD equals the MDD of the OBD readout. After this point, piezoresistive readout performs better than the OBD readout in achievable MDD. Although DS_{OBD} is independent of cantilever thickness, both the cantilever thermomechanical noise N_{th} and the cantilever mechanical bandwidth B_{CNT} depend on thickness; therefore, a MDD achievable with OBD readout also depends on the cantilever thickness.

3.5.3 Dependence of the cantilever dimensions on the spring constant

Any decrease in cantilever length and increase in thickness (at constant l/w ratio) inevitably leads to an increase of the spring constant. For cantilever dimensions we analysed, the spring constants range from 10s N/m to 100s N/m, as is presented in Figure 3.7.

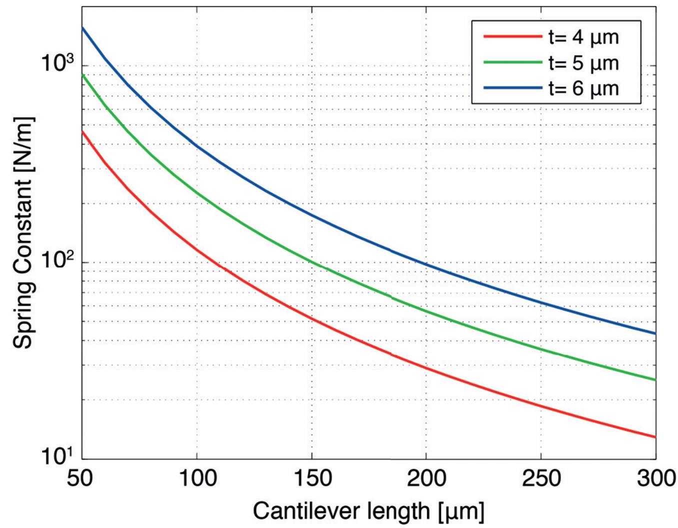

Figure 3.7: Dependence of cantilever spring constant on the cantilever dimensions. The cantilever length-to-width ratio is kept constant at $l/w = 70/30$.

The required cantilever spring constant for AFM depends strongly on the application and the imaging mode and can span up to four orders of magnitude. For AM-AFM imaging in air, cantilevers usually have spring constants in the range from few N/m up to 100 N/m. Traditionally, cantilevers with spring constants in hundreds N/m are considered very stiff and unsuitable for imaging soft samples, and are often identified with a rapid tip wear. However, tip wear comes mainly from lateral forces occurring when the feedback loop cannot compensate surface topography fast enough. A stiffer cantilever with a higher resonance frequency and a higher mechanical bandwidth enables a faster feedback, and hence mitigates the negative effect of the high spring constant on the tip wear. Furthermore, in certain AFM applications, k of the order of several hundred to several thousand is desired and successfully used [153]. Stiffer cantilevers also avoid the problem of surface adhesion that limits the use of softer cantilevers for AM-AFM imaging in air. Therefore, despite higher spring constants, cantilevers with the proposed dimensions are well suited for AM-AFM imaging of stiff samples in air.

3.5.4 Estimation of dissipation power in OBD and piezoresistive readout

For the piezoresistive readout with two active piezoresistors ($R = 1\,\mathrm{k}\Omega$) and a bridge voltage $V_B = 2\,\mathrm{V}$ we estimate the dissipated power as

$$P_{D,PIEZO} = 2 \cdot \frac{(V_B/2)^2}{R} = 2\,\mathrm{mW} \tag{3.21}$$

Measured laser powers shined on a cantilever for Bruker MultiMode AFM head and for custom AFM head [119] were 1.3 mW and 3 mW, respectively. However, it is the tip temperature, rather than overall cantilever dissipation that is critical in AFM imaging.

Using finite element analysis (FEA) we simulated temperature distribution across $70 \times 30 \times 5\,\mu\mathrm{m}^3$ sized silicon cantilever for three different readouts: MultiMode head and custom AFM head [119] OBD readouts and piezoresistive readout using doped silicon piezoresistors (see Figure 3.8). The calculations were performed using COMSOL Multiphysics software platform. We assumed that laser power absorbance for silicon was ≈ 0.65 at $\lambda = 650\,\mathrm{nm}$. The maximum temperature in the cantilever, which is close to the cantilever tip region, was 22.5 °C for MultiMode head, 27.2 °C for custom AFM head and 27.5 °C for piezoresistive readout.

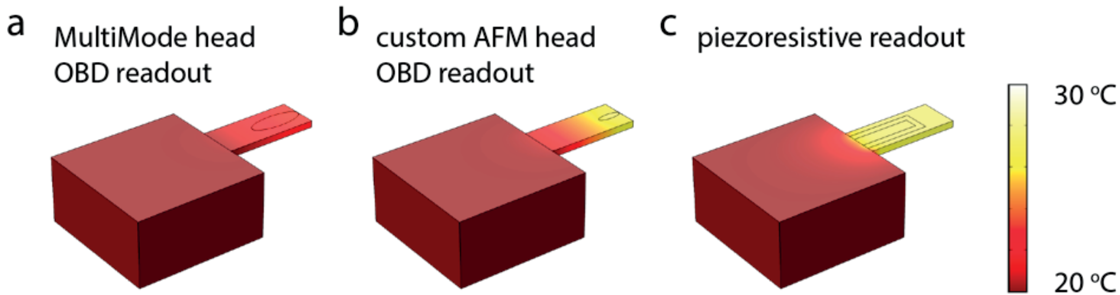

Figure 3.8: Temperature distribution across $70 \times 30 \times 5\,\mu\mathrm{m}^3$ sized silicon cantilever, for three different deflection readouts: **a)** Bruker MultiMode head OBD readout, **b)** Custom AFM head [119] OBD readout dedicated for optical detection of small-sized cantilevers, **c)** Piezoresistive readout with doped silicon resistors.

3.6 Conclusion

Because piezoresistive sensors measure the strain in the cantilever they are best suited for cantilevers with larger thickness and higher spring constants. While this type of cantilever is not well suited for force sensing, we demonstrated that it is very well suited

for deflection sensing and imaging of small feature topographies.

We discussed the cases of two specific electronic readouts: an OBD readout using a transimpedance amplifier and voltage arithmetic electronics, and a piezoresistive readout using a Wheatstone bridge and a differential amplifier. Other types of electronic signal processing also exist for both OBD [49] and piezoresistive [126] readout. However, the electronic readouts that we have chosen to analyse are up to present the most commonly used ones.

The low noise instrumentation amplifier we used in our measurements and calculations has a 4 MHz bandwidth at 10× gain. A wide range of cantilevers with geometries where piezoresistive readout outperforms OBD readout have resonance frequencies within this bandwidth. For further improvement (e.g. higher frequencies), alternate readout setups should also be investigated [126].

We showed that with a measurement bandwidth of 20 kHz and an estimated resistor power dissipation of around 2 mW, the measured imaging noise with the piezoresistive readout is only ≈ 0.3 Å. However, it is the tip temperature, rather than overall cantilever dissipation that is critical in AFM. We simulated the cantilever heating and concluded that the tip temperature was as on par with the temperatures occurring in OBD readout.

We didn't discuss the application of the proposed piezoresistive cantilevers for measurements in fluids. Even though imaging in fluid with piezoresistive cantilevers is possible [154, 155], stiff cantilevers are generally not well suited for imaging of soft biological samples, which are the most common samples that demand a fluid environment.

Although miniaturisation improves cantilever performance, shrinking cantilever dimensions becomes problematic for both readout methods. For OBD readout, cantilever dimensions close to the optical diffraction limit result in laser light spill over and a loss of signal. On the other hand, in piezoresistive readout, fabrication of shallow piezoresistors (necessary to maintain signal-to-noise performance) is very challenging [81, 82]. While the former issue is fundamental, the latter issue is addressable through further developments in the fabrication process of piezoresistive cantilevers.

In this paper, we demonstrated, both theoretically and experimentally that small-sized cantilevers can have equal or better AFM imaging noise performance using piezoresistive readout than using OBD readout. This result refutes the common belief that self-sensing cantilevers are always noisier than optically detected cantilevers. For AM-AFM imaging in air, small-sized and high spring constant cantilevers offer a viable alternative to optical beam deflection. They enable a whole set of different applications where OBD readout is

either not practical or not possible. In the future, further improvements in microfabrication and development of improved strain sensing materials may allow miniaturisation of AFM cantilevers below the optical diffraction limit. Such ultra-miniature cantilevers will further increase the sensitivity and speed of cantilevers for next generation high-speed AFMs. Therefore, we hope that this result stimulates further advances in miniaturisation of piezoresistive self-sensing cantilevers.

Chapter 4

Analog PID controller for HS-AFM

A proportional-integral-derivative (PID) controller is a control loop feedback mechanism widely used in industrial control systems. A PID controller uses as an input an "error" value that is the difference between a measured process variable and a desired setpoint. The controller attempts to minimize the error by adjustment of the process control element. A PID controller consists of three separate parts: the proportional, the integral and the derivative part. Their transfer functions depend on values of their coefficients denoted as K_P, K_I, and K_D, respectively. The weighted sum of the outputs of these three parts is used to adjust process by a control element. By tuning these three coefficients PID controller can provide desired control action for specific process requirements.

All AFM systems contain a feedback controller, which is used to move the scanner in z axis in order to keep the deflection or amplitude of the cantilever constant during scanning. This is used in order to maintain a constant force between the cantilever tip and the sample, which prevents damaging the sample. The most frequently used feedback controller in AFM is the proportional-integral (PI) controller. Bandwidth of the PI controller presents one of the speed limiting factors in HS-AFM, where higher bandwidths enable faster scanning speeds and higher imaging resolution. Most AFM systems use digital signal processor (DSP) based PI feedback controllers, which require analog-to-digital and digital-to-analog converters (ADCs and DACs). These data converters introduce additional delays and quantization noise in the feedback loop, which limit the imaging speed and resolution.

In this chapter we present a digitally controlled analog PID controller. Such controller implementation allows tunability of PID gains over large amplification and frequency range, while also providing precise control of the system and reproducibility of the gain

parameters. By using our analog PID controller we were able to perform successful AFM imaging of a standard silicon calibration grating at line rates of several hundred Hz. The PID controller PCB was designed and provided by Vencislav Todorov (Techproject Company, Vienna, Austria). Research presented in this chapter is yet to be published.

4.1 Introduction

Most of the AFM systems use DSP based PI feedback controllers. In such digital implementation of controller, the signal needs to be sampled and afterwards quantized by ADC before it is sent to the processor. In order to avoid the aliasing problem of high-frequency signals it is necessary to perform signal sampling at frequency which is usually 10 to 20 times higher than the system's closed-loop bandwidth. Additionally, the signal should be low-pass filtered before the sampling, by an anti-aliasing filter. Once the digital processor has calculated the new control value, this value needs to be converted back to the voltage by a DAC in order for it to be applied to the process control element.

ADCs, DACs and filters introduce additional delays in AFM feedback loop and decrease the AFM scanning speed. Moreover, ADCs and DACs can introduce quantization noise, which can be avoided if high precision converters are used. As a consequence, HS-AFMs would necessitate high performance ADCs, DACs and DSPs in order to provide high speed, low noise and conversion precision [156]. These parameters easily increase cost, power consumption and the size of a controller. However, even such high performance digital PID controllers provide a limited frequency bandwidth. For instance, commercial AFM PI controllers usually have bandwidth of about few tens of kHz, which is not sufficient for HS-AFM imaging. Recently, the increased availability of the field programmable gate arrays (FPGA) has led to their use for the implementation of various parts of AFM system, including PID controller [157]. Nevertheless, they suffer from the similar problems as their DSP based counterparts.

In the past many different approaches to increase the speed of the z stage feedback loop were introduced, as was mentioned in Section 1.3.3, mostly by additional adaptation of the PID algorithm [56–58] or by implementing various non-PID based control mechanisms [59–65]. However, such approaches generally lead to an increased complexity of the system and are often more difficult to use.

On the other hand, analog PID controllers should be able to provide larger bandwidth

and eliminate noise issues present in digital implementations. With no sampling necessary, limitations on the bandwidth of the analog PID controller are far less strict. In the past years, advances in the realization of reconfigurable analog blocks led to field programmable analog array (FPAA) systems being used to successfully implement PID controllers for control of various physical processes [156, 158] and for various control applications in AFM as well [159, 160]. FPAA manufacturers even offer manually tunable PID control interface [161]. However, FPAAs use a switched capacitor resistors for tuning so they are still quantised in time. Analog PID controllers were already successfully used in several high-speed AFM experiments [58, 162]. The main disadvantage of the solely analog implementation of the controller is its lack of precise control and parameter reproducibility, and susceptibility to parameter variation due to noise.

Combining a digital control of the gain parameters with analog controller design provides a very precise and fast response controller with ability of dynamic adaptation of control parameters [163]. During this thesis, we have developed a fast digitally controlled analog PID controller which combines the best features from both analog and digital implementation.

4.2 Implementation

In a PID controller, the proportional, integral, and derivative terms are summed up to calculate the output of the PID controller. If we define $u(t)$ as the controller output, the final form of the PID algorithm can be described as

$$u(t) = K_P \cdot e(t) + K_I \cdot \int_0^t e(\tau)\, d\tau + K_D \cdot \frac{d\, e(t)}{dt} \tag{4.1}$$

where $e(t)$ represents the input error value and K_P, K_I and K_D represent proportional, integral and derivative gain of the PID controller, respectively. Proportional, integral and derivative part of the system, together with summation of their outputs, can be realized in analog electronics by using operational amplifiers and passive components, such as resistors and capacitors placed at the amplifier input and feedback loop (see Figure 4.1).

In the design of the PID we used the aforementioned analog design. However, in order to achieve digital control of gain parameters, some of the resistors were replaced with digital-to-analog converters. These DACs convert a digital control data to a certain resistance value of a resistor ladder network. In such implementation, user can configure PID controller gains and various operating parameters using the interface on the computer.

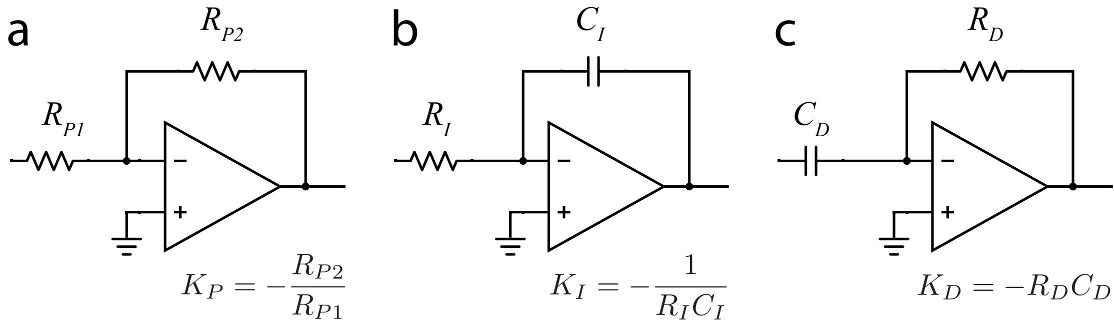

Figure 4.1: PID controller gains realized in analog design using operational amplifiers: **a)** Proportional gain stage **b)** Integrator gain stage **c)** Derivative gain stage

The gain values are then communicated to the PID controller through a digital interface. The digitally controlled analog PID controller is presented in Figure 4.2.

In order to achieve higher frequency range of the integral and the derivative gain stage, these stages were realized in combination of two gain stages: coarse and fine. In the coarse gain stage a single integrator or differentiator was chosen to set the coarse gain, by choosing one of the eight capacitor values. Afterwards, the gain value is fine-tuned by the fine gain stage, through an amplifier with a digitally controlled resistor ladder network in the input (see Figure 4.3). A schematic of the digitally controlled analog PID controller is presented in Figure 4.4a.

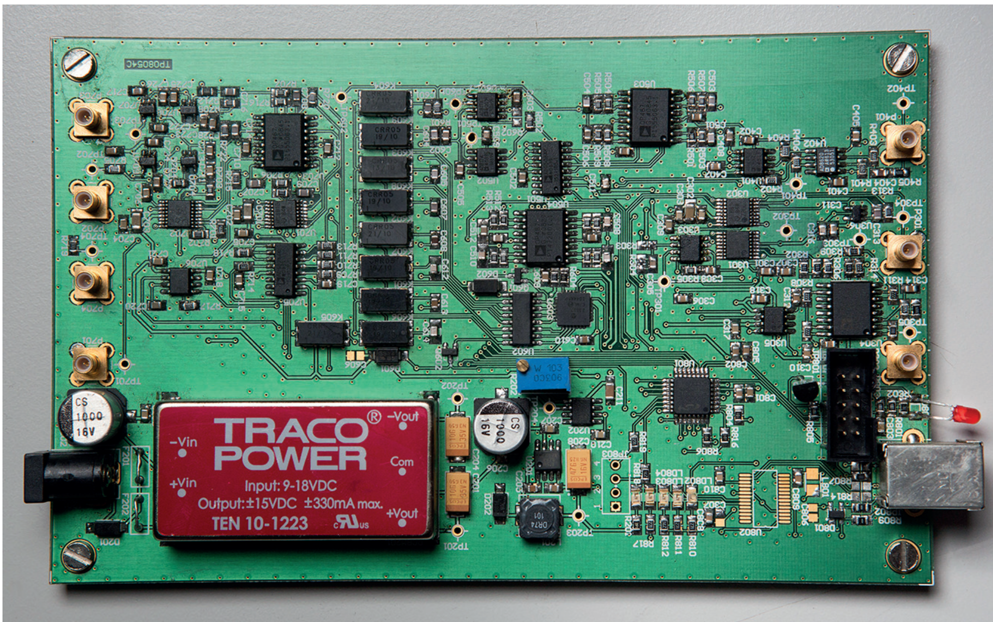

Figure 4.2: A photo of the digitally controlled analog PID controller.

4.2.1 Proportional part

The proportional part has only fine gain stage implemented. All fine gain stages are implemented using an inverting operational amplifier (OP467GS, Analog Devices, USA). The fine gain is tuned by changing the value of the amplifier input resistor, which is done through a digitally controlled R-2R resistor ladder network (DAC8812, Texas Instruments, USA) (see Figure 4.3). The proportional gain can be tuned up to 1×. The system response of the proportional gain stage, at maximum gain setting, is presented in Figure 4.4b. The arrow indicates the direction how gain level can be decreased through the fine gain tuning.

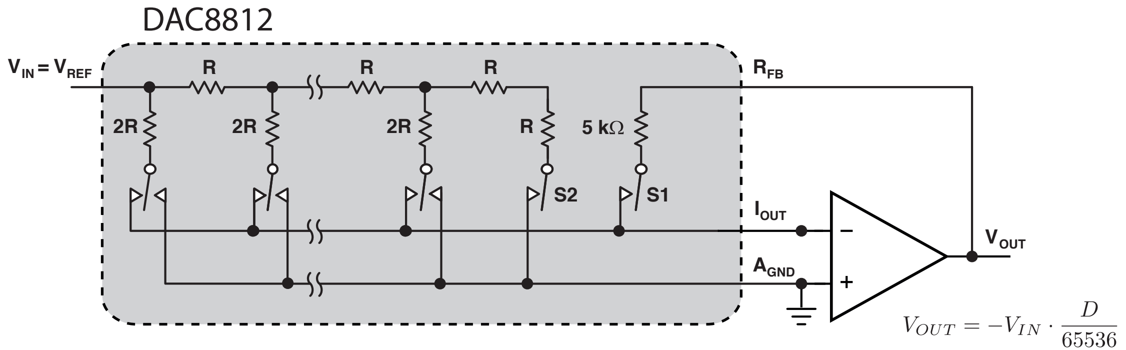

Figure 4.3: A schematic of the fine gain stage

4.2.2 Integral part

The coarse gain in the integral part is defined by an operational amplifier integrator (AD811JR, Analog Devices, USA). The coarse integrator gain is set by choosing the value of the capacitor in the feedback loop. Only one feedback capacitor is closing the feedback at one time, which is set by an array of reed relay switches (CRR05-1A, Meder electronic Inc, USA), as shown in Figure 4.4a. Such implementation of the integral part was chosen, rather than implementing an array of operational amplifier integrators, in order to avoid overheating problem that could appear due to saturation of faster integrators. Reed relay switches are controlled through a parallel I/O expander with serial peripheral interface (SPI) (MCP23S17T, Microchip, USA) and a Darlington transistor array (ULN2003AD, Texas instruments, USA). The system responses of the 8 coarse integrator gain stages are presented in Figure 4.4c. Dashed lines and arrows show how the fine gain stage can be used to tune the integral gain, in the range from one dashed line to another.

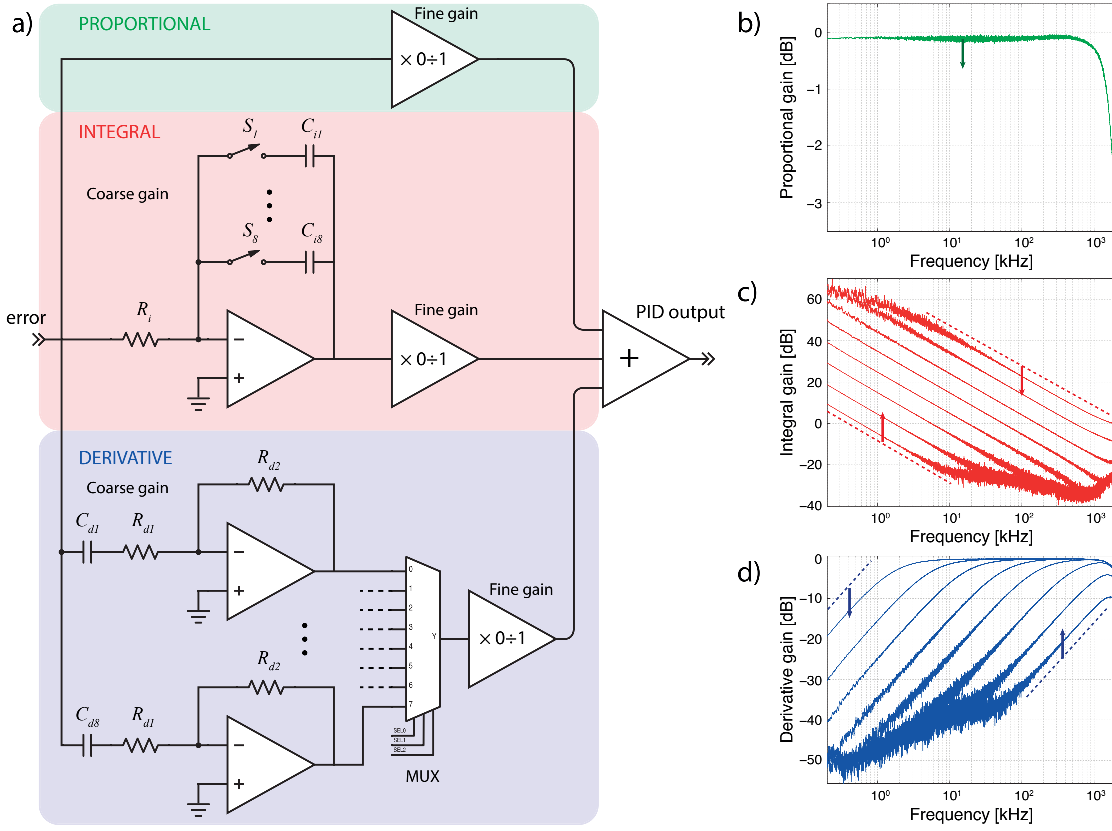

Figure 4.4: **a)** Schematic of the PID controller, presenting coarse and fine gain stages. **b)** Proportional gain bandwidth, maximum gain is around 1×. **c)** Responses of 8 coarse integrator gain stages. Dashed lines and arrows show how fine gain stage can be used to tune the integral gain, in the range from one dashed line to another. **d)** Responses of 8 differentiator gain stages. Dashed lines and arrows show how fine gain stage can be used to tune the derivative gain, in the range from one dashed line to another.

4.2.3 Derivative part

Saturation is not an issue in operational amplifier differentiators. For this reason, the coarse gain in the derivative part is implemented as an array of 8 operational amplifier differentiators (OP467GS, Analog Devices, USA), with each having different time constant e.g. different capacitor value at the input. Further, the coarse gain is set by passing the output of the chosen differentiator, through an analog multiplexer (ADG508, Analog Devices, USA), as presented in Figure 4.4a. The system responses of 8 coarse differentiator gain stages are presented in Figure 4.4d. Again, the dashed lines and arrows show how the fine gain stage can be used to tune the derivative gain, in the range from one dashed line to another. Due to the fact that the gain of a derivative part increases with frequency, an additional resistor is placed in the amplifier input to limit the gain at higher frequencies and hence limit a potential amplification of the high frequency noise.

4.2.4 User interface implementation

The user interface was developed in LabVIEW software (National Instruments, USA). The application provides user to set the overall gain on an error signal, and to set the proportional, integral and derivative gain value. It also allows setting of a DC setpoint voltage (in the range of $\pm 10\,\mathrm{V}$) or to input a certain external signal to be used as a setpoint. The communication with the PCB board is realized by using universal serial bus (USB) interface. Instructions are sent to the microcontroller unit (MCU, C8051F343, Silicon Labs) which supports USB communication. Afterwards the microcontroller communicates with other parts of the system either through SPI protocol or through digital signal lines.

In standard AFM imaging, gains of the PID controller differ for each imaging experiment and each time need to be tuned. It is a common routine to start imaging and then increase each gain, until visible oscillations in the feedback loop occur. Each gain is then set to the maximum value at which no oscillations are visible. As it would be impractical to separately adjust coarse and fine gains during PID operation, gradual increase of the integral and derivative gain was implemented in the software. Both gains are exponentially increased, such as to provide fine gain steps at lower gain values and large gain steps at higher gain values.

4.3 Characterization

We characterized the PID controller in terms of the electrical bandwidth, the output noise and the sinusoidal disturbance rejection when the PID controller is placed in an AFM feedback loop. The electrical bandwidth was measured by sweeping the frequency of the input signal, while the PID output was fed back to the external setpoint input (see Figure 4.5a). Gains of the PID controller were increased just until the point where the frequency response peaking would start to show. The amplitude and the phase frequency response of the PID controller, measured under such set gains are presented in Figure 4.5b. $-3\,\mathrm{dB}$ point is located at around $834\,\mathrm{kHz}$.

From the phase diagram presented in Figure 4.5b one could notice that at $-3\,\mathrm{dB}$ point, the phase loss is around 180° which is quite significant. The reason for this is that the current implementation has a large array of operational amplifiers and switches on the signal path, each of them contributing a certain phase delay. Such design was implemented in order to provide more options for testing of the circuit and various functionalities such

as an inversion of the input signal, amplification of an error signal, choice to switch off individual gain parts etc. If we simplify the system design in the future version, a decreased number of components would lead to a reduction of the phase loss and a faster feedback of the controller.

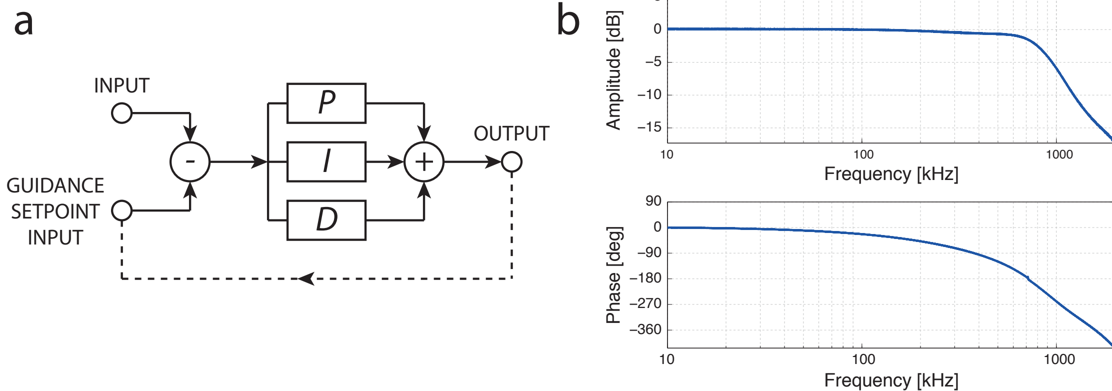

Figure 4.5: The electrical bandwidth measurement of the PID controller: **a)** Schematic of the measurement setup. **b)** Frequency response of the PID output (up: amplitude, down: phase).

We also measured the voltage noise spectral density on the PID controller output. The PID controller was connected as in Figure 4.5a, and gains were increased just up to the point where the frequency response peaking starts to show. The input of the PID controller was terminated with a $50\,\Omega$ resistance and the setpoint was set to $0\,\mathrm{V}$. Noise level above $100\,\mathrm{Hz}$ was typically around $0.2 - 0.3\,\mu\mathrm{V}/\sqrt{\mathrm{Hz}}$.

We measured a disturbance rejection of the PID controller in an AFM feedback loop. We performed a comparison between our analog PID controller and the digital PI controller, that is an integral part of the commercial AFM system (Nanoscope 8 controller, Bruker), see Figure 4.6a-b. A sinusoidal height modulation (disturbance) at variable frequency was applied to z piezoelectric actuator and resulting deflection of the cantilever in the contact mode was measured (see Figure 4.6a for measurement setup). A custom-built fast z scanner with flat response up to $200\,\mathrm{kHz}$ and a custom made AFM head [119, 164] were used in the measurements. The gains of both PID controllers were increased just until the point where the visible oscillations of the system would start to show in the AFM image or until the point where there was no visible response peaking above the response curve taken with no feedback. Figure 4.6b shows a deviation of the cantilever deflection from the defined setpoint depending on the height disturbance frequency, for both cases.

As the frequency of the height disturbance increases, at certain point the PID controller will stop reacting fast enough to produce an appropriate signal to cancel the cantilever

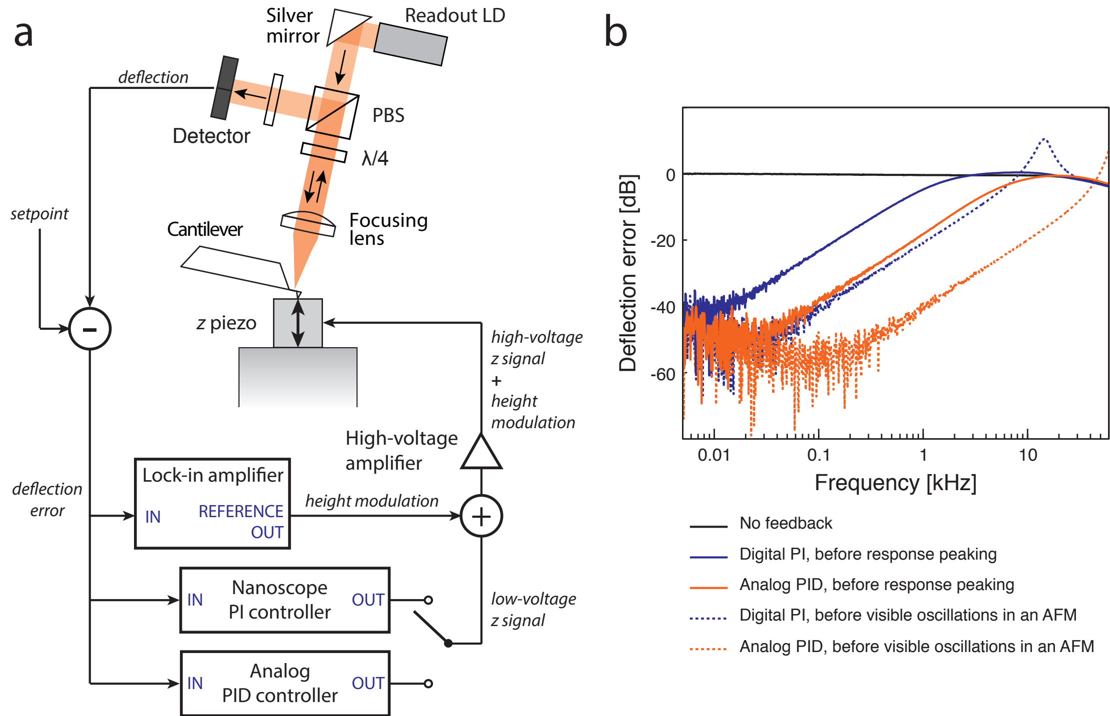

Figure 4.6: A closed-loop comparison between the analog PID and the commercial digital PI controller (Nanoscope 8, Bruker) in cantilever surface tracking: **a)** Measurement setup, **b)** Lock-in amplifier measurement of the cantilever deflection deviation from the defined setpoint. One can notice that the analog PID is almost one order of magnitude faster in surface tracking that the digital PID.

deflection error. At that point the cantilever deflection error starts to rise. Finally, at certain frequencies the PID controller will not track the surface at all and the entire hight disturbance will be present in the cantilever deflection error. From Figure 4.6b we can notice that the analog PID controller can reject the height disturbances up to almost to one order of magnitude higher frequencies than the digital PID controller.

4.4 Imaging results

We used the analog PID controller to perform high-speed AFM imaging in contact mode. The imaging was performed with a custom made AFM high-speed scanner, similar to the one published in [14, 162] and a custom made AFM head [119]. The AFM image acquisition was performed with a custom made data acquisition system [14, 165]. We used a silicon calibration grating (1 µm × 1 µm, 200 nm deep, platinum coated, Digital Instruments, Veeco) as an imaging sample to test the performance of the PID controller.

The imaging was performed in contact mode with SCANASYST-AIR (Bruker, USA) cantilever probes. The AFM images presented in Figure 4.7a-b are taken at 0.514 kHz line rate (2 images per second, ∼ 3.6 mm/s) and 0.723 kHz line rate (2.8 images per second, ∼ 5 mm/s speed). A combination of 3 sine waves was sent to the fast axis scanner, to avoid fast axis resonance excitation. The slow axis signal was amplified with a commercial high voltage amplifier (High speed AFM piezo power amplifier, TechProject Company, Austria). The fast axis signal was amplified using a custom designed high voltage amplifier (manuscript in preparation, S. Andany et al.). AFM images show that the analog PID can be used for very fast AFM imaging. Distortions in the images are related to the scanner, which had resonance issues at such high scanning speeds.

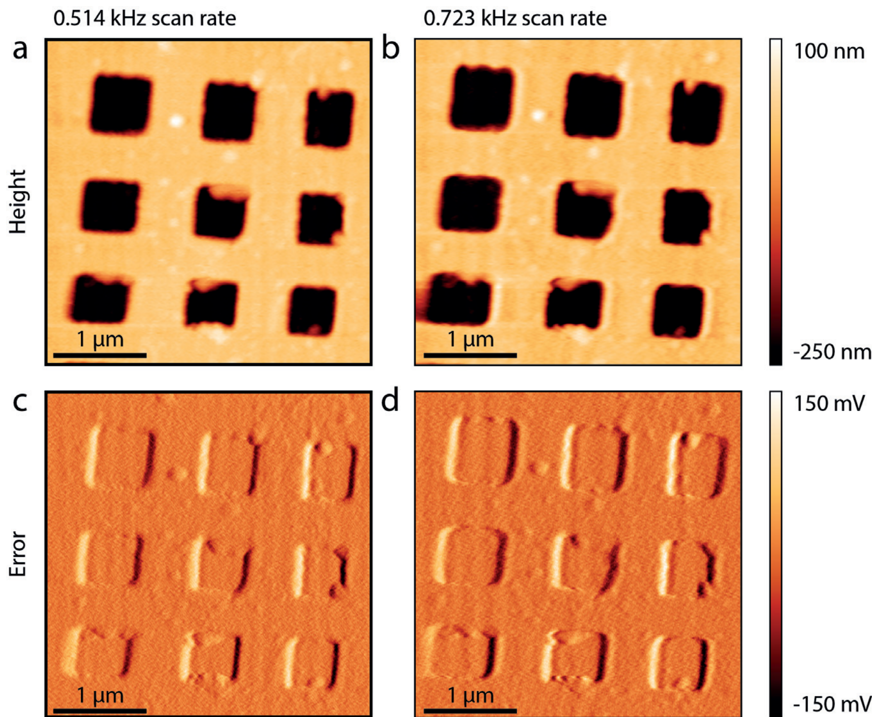

Figure 4.7: AFM images of a silicon calibration grating obtained in air at 0.514 kHz (**a)** and **c)**) and 0.723 kHz (**b)** and **d)**). Images **a)** and **b)** are height images, and images **c)** and **d)** are deflection error images. Scan size was around 3.5 µm and images were taken at 256 lines by 512 pixels. Waves that can be noticed on images **b)** and **d)** are artefacts coming from the fact that we are starting to excite the x scanner resonance.

4.5 Conclusion

Due to signal sampling and aliasing issues, digital PID controllers must operate at frequencies that are 10-20 times higher than the closed loop bandwidth of the control system. On the other hand, analog controllers do not face such issues and should be able to provide much faster response.

However, due of the lack of dynamic adaptation of control parameters, analog PID controllers were mostly used in control of invariable processes, where the desired control gains were determined and set by fixed components to never or rarely change. Implementing digital control of the analog controller parameters opens up new possibilities for the use of analog PID controllers, which can be especially beneficial for the control of the fast processes.

One of the benefits of digital controllers is that they can be easily reconfigured (e.g. to include or exclude some gain parameters or to change the PID configuration from parallel to serial). In our analog PID controller we enabled a user to include or exclude some of the PID gains, by using analog switches. However, the switches introduce additional phase loss on the signal path and limit the controller bandwidth.

We developed a digitally controlled analog PID controller and successfully demonstrated that it can be used in high-speed AFM imaging at several hundreds Hz line rates and several mm/s speeds. The current design of the PID controller could be improved in terms of bandwidth and phase loss, by simplifying the design and removing some of the components on the signal path, and by replacing some components for the ones that have a faster performance. We think that the noise of the system could also be improved with some redesign, for instance by replacing the switching DC/DC converter power supply, currently used.

Chapter 5

Conclusion

5.1 Why self-sensing techniques?

Since the invention of AFM, atomic force microscopy has evolved in many aspects and various parts of the system were upgraded. This finally led to a development of HS-AFM in the last decade and enabled significant scientific discoveries [16–36]. However, while scanners and electronic systems are constantly improved, there was a hold-up in the cantilever sensor and readout technique development (see Figure 5.1). The very latest AFM systems still rely on the OBD readout and SiN cantilevers, which both limit the cantilever mechanical bandwidth and AFM imaging speed. That being said, some of the smallest cantilevers detectable with the OBD readout were used already more than a decade ago [40, 166].

Although, using lower wavelength lasers would theoretically provide smaller focused beam area and allow the use of smaller-sized higher-bandwidth cantilevers, in practice that is not an option for several reasons: standard optically reflective materials used to coat cantilevers (e.g. such as Au) become highly absorbent at lower wavelengths; a lower wavelength light can damage the solid states samples by ionization; a lower wavelength light also has a fatal effect on the biological samples (as it destroys nucleic acids and disrupts their DNA) and is often used as a disinfection method; On the other hand, AFM is one of the rare tools that allows us to inspect biological processes on a molecular level and perform real-time imaging of living matter.

To advance the HS-AFM further, novel sensing techniques and/or alternative cantilever materials are necessary. Various optical readout techniques were proposed in recent

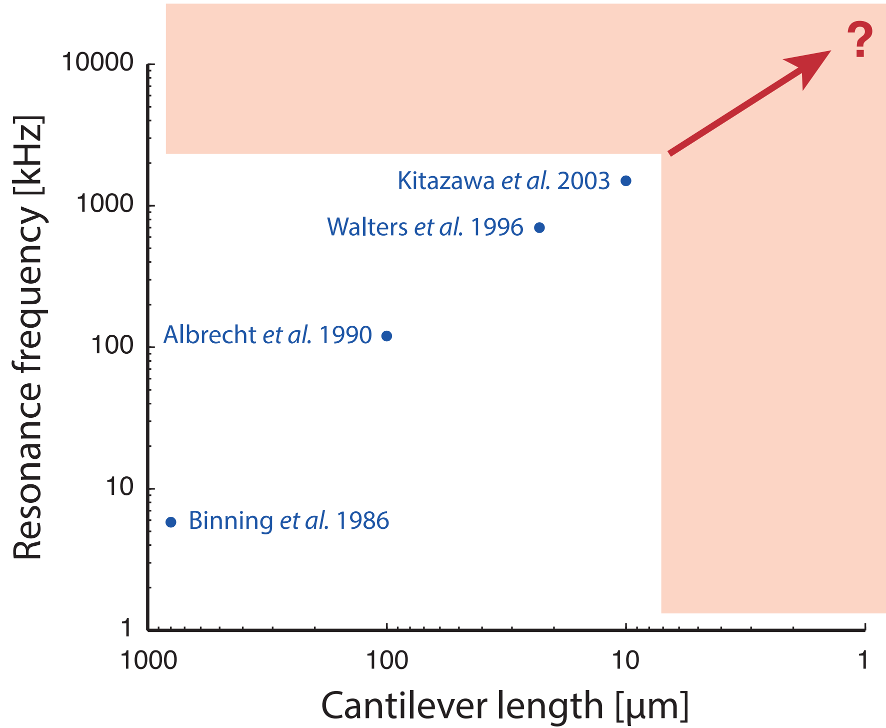

Figure 5.1: Cantilever development since the AFM discovery: The first AFM cantilevers were $\sim$ 1 mm long and had $\sim$ 6 kHz resonance frequency [3]. In the following years cantilever size was constantly decreased by the use and perfecting of microfabrication techniques [167, 168]. The smallest cantilevers, still detectable by OBD were developed more than a decade ago by Olympus [40, 166], having length of around 10 µm and frequency of $\sim 1.3 - 1.8$ MHz.

years, which demonstrated sensing of the cantilevers with dimensions below the optical diffraction limit [108–110]. However, such optical techniques demand very complicated and/or space consuming measurement setups and were not yet shown to work for AFM.

On the other hand, self-sensing techniques incorporating deflection sensor on the cantilever, offer many advantages that can not be achieved with optical readout, as was discussed in Section 1.4. One of the main advantages is their potential to detect submicron-sized cantilevers [91]. However, it is still very challenging to fabricate small-sized fully-released self-sensing cantilevers, that could match AFM imaging performance of an OBD readout [81, 87, 91]. Therefore, the NTR strain-sensors, with their ability to be 3D printed in 10s of nm sized structures and having reasonably high gauge factors, promised a great potential for the use in AFM.

In this thesis we presented the research related to two self-sensing techniques for cantilever deflection measurement in AFM. The NTR sensing technique was applied in AFM for the first time. We have also demonstrated that the NTRs could be used for sensing of the sub-micron sized cantilevers, showing a potential for NTR sensing to be used in the

next generation high-bandwidth cantilevers for HS-AFM or in various nanoelectromechanical systems (NEMS) sensors. Future research in NTR cantilevers would involve development of a fully released sub-micron sized NTR cantilevers with a sharp tip. In addition, alternative metal precursors would be very interesting to investigate, to potentially achieve higher gauge factors.

In the scope of this thesis we have also reviewed silicon doped piezoresistors for deflection sensing of AFM cantilevers. Although such self-sensing cantilevers were present since the early days of AFM, we showed both theoretically and experimentally that their real potential lies in the miniaturization of the cantilever and piezoresistor. While such cantilevers would generally have higher spring constants they are still suitable for low-noise imaging of various samples in air. Such miniaturized self-sensing high-speed cantilevers could, for instance find their use in high quality metrology applications for the semiconductor industry, where OBD readout usually introduces artefacts coming from the stray light reflectance.

5.1.1 Beyond Si/SiN cantilevers

We have already mentioned that a higher mechanical bandwidth of the cantilever, and hence a higher imaging speed, can be achieved either by increasing its resonance frequency (that is by decreasing its size) or by decreasing the cantilever Q factor. Latter can be accomplished either by imaging in a high damping environment (such as liquid) or by decreasing the intrinsic Q factor of the cantilever by making it out of a high damping material such as polymer [41].

The highest scanning speed could be achieved in the combination of the two conditions, by developing small-sized self-sensing polymer cantilevers. Such cantilevers would be especially beneficial for scanning in a vacuum environment, where Q factor is several orders of magnitude higher than in the air and the scanning speed is impractically low. However, in development of such cantilevers there are certain challenges to be solved: polymer tips are very soft and prone to breaking; also integration of the strain-sensing element on a polymer cantilever is not trivial. Some of the research in a development of such cantilevers is currently being done in our laboratory. Both of the above-mentioned problems can be solved by encapsulating a polymer layer between two thin Si-based layers. We have developed the first trilayer self-sensing cantilever (see Figure 5.2a), and such trilayer cantilevers were successfully used in AFM imaging (see Figure 5.2b). By using trilayer polymer cantilevers, we envision a possibility to perform HS-AFM imaging in vacuum, which would allow for a variety of novel analytical methods such as

FIB/AFM tomography. In an application where AFM imaging is to be performed in a SEM chamber, self-sensing cantilevers are almost a requisite as OBD readout requires a lot of space, which is not available in a standard SEM chamber. Moreover, strain-sensing element in such cantilever is fully encapsulated which could allow use of these cantilevers in liquids.

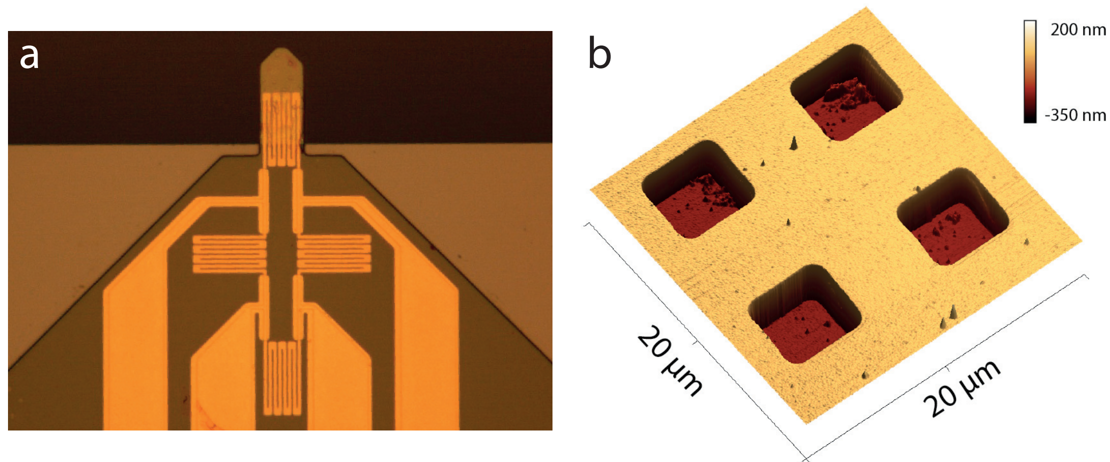

Figure 5.2: Trilayer SiN-parylene-SiN cantilever: **a)** An optical microscope image of $100 \times 50 \times 3.9\,\mu m^3$ sized cantilever. An active thin Au film resistor integrated on the cantilever body and three passive thin Au film resistors integrated on the cantilever chip formed a Wheatstone bridge used for strain-sensing readout. **b)** An AFM image of a silicon calibration grating obtained in air using a trilayer cantilever.

5.2 The return to the analog electronics

All the signals in an AFM feedback loop are analog in nature: an output of the deflection sensing readout which is sent to the input of the feedback controller, the feedback controller output signal which is sent to the high voltage amplifier, and the high voltage signal which is finally used to move the z piezoelectric actuator. However, some parts of the AFM system are most often implemented in digital electronics, such as the feedback controller and the system for data acquisition and presentation. One of the reasons why the feedback controller is mainly realised in a digital implementation is because such implementation provides great control of the system and reproducibility of the gain parameters. However, by using an analog feedback controller, one could significantly reduce delays in the feedback loop (such as ones coming from the ADCs and DACs), which would increase the AFM scanning speed and which would simplify the overall AFM design.

During this thesis research we have developed a fast analog feedback controller for HS-AFM. We designed a digitally controlled analog PID controller and successfully demonstrated that it can be used in high-speed AFM imaging at several hundreds Hz line rates and several mm/s speeds. The analog design of the PID controller allowed tunability of the PID gains over large amplification and frequency range, while the digital input of the controller parameters provided higher control of the system parameters, inherent to a digital implementation. With this example, we have shown that with a relatively simple analog design one could potentially implement much faster feedback controllers, than the ones realized using digital design and DSPs.

5.3 AFM: future outlook

Future development in AFM can be divided in several areas: novel imaging and sample characterization techniques; the next generation of HS-AFMs with upgrades of each of the individual system components such as the cantilever, the scanner and the feedback electronics; and novel applications of AFM, including the new devices and protocols for immobilization of living matter, and integration of AFM with other characterization instruments (such as super resolution microscopes and SEM).

5.3.1 Novel imaging techniques

Novel imaging techniques that are constantly developed allow characterization of the various mechanical properties of the sample at the real-time, higher imaging speeds, less invasive imaging of samples and higher spatial resolution. For instance, PeakForce quantitative nanoscale mechanical (PF-QNM) characterization technique can supply real-time information about the sample Young's modulus, adhesion, dissipation, deformation etc. while keeping the peak force applied to the sample constant [169]. Drive-amplitude-modulation AFM (DAM-AFM) technique [170] allows stable AFM imaging in various environments, ranging from liquid to vacuum, while keeping the dissipation constant. Once used in vacuum, DAM-AFM can achieve higher imaging speeds, close to the ones achieved in FM-AFM, while it overcomes the instability issues present in FM-AFM. Various multi-frequency techniques, where the cantilever is excited to oscillate at multiple frequencies, allow simultaneous imaging of topography and other sample properties (mechanical, magnetic or electrical) [171–173], achieving higher spatial resolution of the sample [174] and faster imaging [164, 175]. An increase of the electrical bandwidth of the AFM electronics in combination with the photothermal actuation, which can excite high

frequency resonance modes, will probably enable many improvements in multi-frequency AFM imaging [164]. Generally, in the future we can expect many novel imaging techniques and improvement of the existing ones.

5.3.2 The next generation of HS-AFM

With the further development of the cantilevers and deflection readout techniques, cantilever resonance excitation techniques, scanners and feedback electronics (the feedback controllers and the lock-in amplifiers) we can envision the emergence of the next generation HS-AFMs, which would achieve imaging rates of several 10s of frames per second at several µm scan ranges. The necessity for the novel cantilever deflection sensing techniques and/or alternative cantilever materials was already discussed in Section 5.1. As we go smaller in size additional techniques to excite cantilever resonances will need to be investigated. While photothermal excitation can excite higher frequency modes in 10s of MHz, its efficient excitation is highly dependent on the laser position along the cantilever length. Therefore, we will again encounter an optical diffraction limit challenge. We can expect novel scanner designs having higher resonances and scanner drivers capable to excite piezoelectric actuators at higher bandwidths. As previously mentioned, we can expect a return to the analog electronics to achieve lower feedback loop times and lock-in amplifiers or phase-locked loop (PLL) systems needing less oscillation cycle time to demodulate the signal [48, 50].

5.3.3 Novel AFM applications

Novel applications for AFM constantly arise [31–34,176,177]. While in the previous years much research was performed in inspecting fast changes in protein and cell dynamics, using HS-AFM [16–36], a novel time-lapse technique recently begin to be increasingly used to study long-term development and behaviour of bacteria [176]. In such AFM imaging, images are taken at moderate rates (few minutes per image) but imaging process takes from several hours to several days. If combined with optical microscopy, such technique can provide significant insight in bacteria growth, division processes, antibiotic resistance etc. Some of the main challenges in such imaging are development of the immobilization protocols, selection of appropriate imaging technique and parameters such as not to disrupt the sample and design of the fluidic system needed for constant supply of cell culture medium to the AFM fluid cell. Integration of AFM with different characterization instruments became increased trend in the last years. In studying of

biological samples, such as cell or bacteria, combining optical microscopes with AFM enable simultaneous displaying of the high-resolution 3D topography and stiffness images, while correlating them to cell or bacteria structural elements [31–34]. AFM combined with SEM can also provide some interesting analytical methods for sample inspection, as was previously mentioned.

5.4 A closing note

We envision that progress in all of these areas should lead to significant scientific discoveries, helping us to better understand the world that we live in. We hope that the research performed in the scope of this thesis opened the door for the future development of the sub-micron sized cantilevers and the next generation of high-speed atomic force microscopes.

Bibliography

[1] A. Bogner, P.-H. Jouneau, G. Thollet, D. Basset, and C. Gauthier, "A history of scanning electron microscopy developments: Towards "wet-STEM" imaging," *Micron*, vol. 38, pp. 390–401, jun 2007.

[2] M. Knoll and E. Ruska, "Das Elektronenmikroskop," *Zeitschrift fur Phys.*, vol. 79, pp. 699–699, sep 1932.

[3] G. Binnig, C. F. Quate, and C. Gerber, "Atomic force microscope," *Phys. Rev. Lett.*, vol. 56, no. 9, pp. 930–933, 1986.

[4] E. Betzig, G. H. Patterson, R. Sougrat, O. W. Lindwasser, S. Olenych, J. S. Bonifacino, M. W. Davidson, J. Lippincott-Schwartz, and H. F. Hess, "Imaging Intracellular Fluorescent Proteins at Nanometer Resolution," *Science (80-.).*, vol. 313, pp. 1642–1645, sep 2006.

[5] S. T. Hess, T. P. Girirajan, and M. D. Mason, "Ultra-High Resolution Imaging by Fluorescence Photoactivation Localization Microscopy," *Biophys. J.*, vol. 91, pp. 4258–4272, dec 2006.

[6] M. J. Rust, M. Bates, and X. Zhuang, "Sub-diffraction-limit imaging by stochastic optical reconstruction microscopy (STORM)," *Nat. Methods*, vol. 3, no. 10, pp. 793–796, 2006.

[7] G. Binnig, H. Rohrer, C. Gerber, and E. Weibel, "Surface Studies by Scanning Tunneling Microscopy," *Phys. Rev. Lett.*, vol. 49, pp. 57–61, jul 1982.

[8] G. Friedbacher and H. Fuchs, "Classification of scanning probe microscopies," Tech. Rep. 7, 1999.

[9] P. Eaton and P. West, *Atomic Force Microscopy.* New York: Oxford University Press, 2010.

[10] Y. Martin, C. C. Williams, and H. K. Wickramasinghe, "Atomic force microscope–force mapping and profiling on a sub 100-Å scale," *J. Appl. Phys.*, vol. 61, no. 10, p. 4723, 1987.

[11] J. Tamayo and R. García, "Deformation, Contact Time, and Phase Contrast in Tapping Mode Scanning Force Microscopy," *Langmuir*, vol. 12, pp. 4430–4435, jan 1996.

[12] T. R. Albrecht, P. Grütter, D. Horne, and D. Rugar, "Frequency modulation detection using high-Q cantilevers for enhanced force microscope sensitivity," *J. Appl. Phys.*, vol. 69, no. 2, p. 668, 1991.

[13] A. Aliano and G. Cicero, *Encyclopedia of Nanotechnology.* 2012.

[14] G. E. Fantner, G. Schitter, J. H. Kindt, T. Ivanov, K. Ivanova, R. Patel, N. Holten-Andersen, J. Adams, P. J. Thurner, I. W. Rangelow, and P. K. Hansma, "Components for high speed atomic force microscopy," *Ultramicroscopy*, vol. 106, pp. 881–887, jun 2006.

[15] P. K. Hansma, G. Schitter, G. E. Fantner, and C. Prater, "High-speed Atomic Force Microscopy," *Science (80-.).*, vol. 314, no. 5799, pp. 601–602, 2006.

[16] A. Miyagi, Y. Tsunaka, T. Uchihashi, K. Mayanagi, S. Hirose, K. Morikawa, and T. Ando, "Visualization of Intrinsically Disordered Regions of Proteins by High-Speed Atomic Force Microscopy," *ChemPhysChem*, vol. 9, pp. 1859–1866, sep 2008.

[17] H. Yamashita, K. Voïtchovsky, T. Uchihashi, S. A. Contera, J. F. Ryan, and T. Ando, "Dynamics of bacteriorhodopsin 2D crystal observed by high-speed atomic force microscopy," *J. Struct. Biol.*, vol. 167, no. 2, pp. 153–158, 2009.

[18] P.-E. Milhiet, D. Yamamoto, O. Berthoumieu, P. Dosset, C. Le Grimellec, J.-M. Verdier, S. Marchal, and T. Ando, "Deciphering the structure, growth and assembly of amyloid-like fibrils using high-speed atomic force microscopy.," *PLoS One*, vol. 5, p. e13240, oct 2010.

[19] N. Kodera, D. Yamamoto, R. Ishikawa, and T. Ando, "Video imaging of walking myosin V by high-speed atomic force microscopy.," *Nature*, vol. 468, pp. 72–76, nov 2010.

[20] M. Shibata, H. Yamashita, T. Uchihashi, H. Kandori, and T. Ando, "High-speed atomic force microscopy shows dynamic molecular processes in photoactivated bacteriorhodopsin," *Nat. Nanotechnol.*, vol. 5, pp. 208–212, mar 2010.

[21] T. Uchihashi, R. Iino, T. Ando, and H. Noji, “High-speed atomic force microscopy reveals rotary catalysis of rotorless F1-ATPase.,” *Science*, vol. 333, pp. 755–8, aug 2011.

[22] M. Shibata, T. Uchihashi, H. Yamashita, H. Kandori, and T. Ando, “Structural Changes in Bacteriorhodopsin in Response to Alternate Illumination Observed by High-Speed Atomic Force Microscopy,” *Angew. Chemie Int. Ed.*, vol. 50, pp. 4410–4413, may 2011.

[23] M. Hashimoto, N. Kodera, Y. Tsunaka, M. Oda, M. Tanimoto, T. Ando, K. Morikawa, and S.-i. Tate, “Phosphorylation-Coupled Intramolecular Dynamics of Unstructured Regions in Chromatin Remodeler FACT,” *Biophys. J.*, vol. 104, pp. 2222–2234, may 2013.

[24] N. Yilmaz, T. Yamada, P. Greimel, T. Uchihashi, T. Ando, and T. Kobayashi, “Real-time visualization of assembling of a sphingomyelin-specific toxin on planar lipid membranes,” *Biophys. J.*, vol. 105, pp. 1397–1405, sep 2013.

[25] H. Yamashita, K. Inoue, M. Shibata, T. Uchihashi, J. Sasaki, H. Kandori, and T. Ando, “Role of trimer–trimer interaction of bacteriorhodopsin studied by optical spectroscopy and high-speed atomic force microscopy,” *J. Struct. Biol.*, vol. 184, pp. 2–11, oct 2013.

[26] M. Imamura, T. Uchihashi, T. Ando, A. Leifert, U. Simon, A. D. Malay, and J. G. Heddle, “Probing Structural Dynamics of an Artificial Protein Cage Using High-Speed Atomic Force Microscopy,” *Nano Lett.*, vol. 15, pp. 1331–1335, feb 2015.

[27] I. Casuso, P. Sens, F. Rico, and S. Scheuring, “Experimental Evidence for Membrane-Mediated Protein-Protein Interaction,” *Biophys. J.*, vol. 99, pp. L47–L49, oct 2010.

[28] A. Suzuki, T. Hori, T. Nishino, J. Usukura, A. Miyagi, K. Morikawa, and T. Fukagawa, “Spindle microtubules generate tension-dependent changes in the distribution of inner kinetochore proteins,” *J. Cell Biol.*, vol. 193, pp. 125–140, apr 2011.

[29] A. J. Katan, R. Vlijm, A. Lusser, and C. Dekker, “Dynamics of Nucleosomal Structures Measured by High-Speed Atomic Force Microscopy,” *Small*, vol. 11, pp. 976–984, feb 2015.

[30] G. E. Fantner, R. J. Barbero, D. S. Gray, and A. M. Belcher, “Kinetics of antimicrobial peptide activity measured on individual bacterial cells using high-speed atomic force microscopy.,” *Nat. Nanotechnol.*, vol. 5, no. March, pp. 280–285, 2010.

[31] A. Colom, I. Casuso, F. Rico, and S. Scheuring, “A hybrid high-speed atomic force–optical microscope for visualizing single membrane proteins on eukaryotic cells,” *Nat. Commun.*, vol. 4, pp. 1–8, jul 2013.

[32] Y. Suzuki, N. Sakai, A. Yoshida, Y. Uekusa, A. Yagi, Y. Imaoka, S. Ito, K. Karaki, and K. Takeyasu, “High-speed atomic force microscopy combined with inverted optical microscopy for studying cellular events,” *Sci. Rep.*, vol. 3, pp. 1–7, jul 2013.

[33] S. Fukuda, T. Uchihashi, R. Iino, Y. Okazaki, M. Yoshida, K. Igarashi, and T. Ando, “High-speed atomic force microscope combined with single-molecule fluorescence microscope,” *Rev. Sci. Instrum.*, vol. 84, no. 7, p. 073706, 2013.

[34] P. D. Odermatt, A. Shivanandan, H. Deschout, R. Jankele, A. P. Nievergelt, L. Feletti, M. W. Davidson, A. Radenovic, and G. E. Fantner, “High-Resolution Correlative Microscopy: Bridging the Gap between Single Molecule Localization Microscopy and Atomic Force Microscopy,” *Nano Lett.*, vol. 15, pp. 4896–4904, aug 2015.

[35] H. Watanabe, T. Uchihashi, T. Kobashi, M. Shibata, J. Nishiyama, R. Yasuda, and T. Ando, “Wide-area scanner for high-speed atomic force microscopy,” *Rev. Sci. Instrum.*, vol. 84, no. 5, p. 053702, 2013.

[36] M. Shibata, T. Uchihashi, T. Ando, and R. Yasuda, “Long-tip high-speed atomic force microscopy for nanometer-scale imaging in live cells,” *Sci. Rep.*, vol. 5, p. 8724, mar 2015.

[37] T. Ando, N. Kodera, D. Maruyama, E. Takai, K. Saito, and A. Toda, “A high-speed atomic force microscope for studying biological macromolecules in action,” *Japanese J. Appl. Physics, Part 1 Regul. Pap. Short Notes Rev. Pap.*, vol. 41, no. 7 B, pp. 4851–4856, 2002.

[38] A. D. L. Humphris, M. J. Miles, and J. K. Hobbs, “A mechanical microscope: High-speed atomic force microscopy,” *Appl. Phys. Lett.*, vol. 86, no. 3, p. 034106, 2005.

[39] D. Sarid, *Scanning Force Microscopy With Applications to Electric, Magnetic and Atomic Forces*. 1994.

[40] M. Kitazawa, K. Shiotani, and A. Toda, “Batch Fabrication of Sharpened Silicon Nitride Tips,” *Jpn. J. Appl. Phys.*, vol. 42, pp. 4844–4847, jul 2003.

[41] J. D. Adams, B. W. Erickson, J. Grossenbacher, J. Brugger, A. Nievergelt, and G. E. Fantner, “Harnessing the damping properties of materials for high-speed atomic force microscopy,” *Nat. Nanotechnol.*, vol. in press, pp. 1–6, nov 2015.

[42] C. Braunsmann and T. E. Schäffer, "High-speed atomic force microscopy for large scan sizes using small cantilevers.," *Nanotechnology*, vol. 21, p. 225705, jun 2010.

[43] D. J. Burns, K. Youcef-Toumi, and G. E. Fantner, "Indirect identification and compensation of lateral scanner resonances in atomic force microscopes," *Nanotechnology*, vol. 22, no. 31, p. 315701, 2011.

[44] S. R. Manalis, S. C. Minne, and C. F. Quate, "Atomic force microscopy for high speed imaging using cantilevers with an integrated actuator and sensor," *Appl. Phys. Lett.*, vol. 67, no. 9, pp. 871–873, 1996.

[45] T. Sulchek, R. Hsieh, J. D. Adams, S. C. Minne, C. F. Quate, and D. M. Adderton, "High-speed atomic force microscopy in liquid," *Rev. Sci. Instrum.*, vol. 71, no. 5, p. 2097, 2000.

[46] D. Alsteens, V. Dupres, S. Yunus, J.-P. Latgé, J. J. Heinisch, and Y. F. Dufrêne, "High-Resolution Imaging of Chemical and Biological Sites on Living Cells Using Peak Force Tapping Atomic Force Microscopy," *Langmuir*, vol. 28, pp. 16738–16744, dec 2012.

[47] A. P. Nievergelt, B. W. Erickson, N. Hosseini, J. D. Adams, and G. E. Fantner, "Studying biological membranes with extended range high-speed atomic force microscopy," *Sci. Rep.*, vol. 5, p. 11987, 2015.

[48] T. Ando, N. Kodera, E. Takai, D. Maruyama, K. Saito, and A. Toda, "A high-speed atomic force microscope for studying biological macromolecules," *Proc. Natl. Acad. Sci.*, vol. 98, pp. 12468–12472, oct 2001.

[49] R. Enning, D. Ziegler, A. Nievergelt, R. Friedlos, K. Venkataramani, and A. Stemmer, "A high frequency sensor for optical beam deflection atomic force microscopy," *Rev. Sci. Instrum.*, vol. 82, no. 4, p. 043705, 2011.

[50] B. Schlecker, M. Dukic, B. Erickson, M. Ortmanns, G. Fantner, and J. Anders, "Single-Cycle-PLL Detection for Real-Time FM-AFM Applications," *IEEE Trans. Biomed. Circuits Syst.*, vol. 8, pp. 206–215, apr 2014.

[51] A. J. Fleming and S. O. R. Moheimani, "Improved Current and Charge Amplifiers for Driving Piezoelectric Loads, and Issues in Signal Processing Design for Synthesis of Shunt Damping Circuits," *J. Intell. Mater. Syst. Struct.*, vol. 15, pp. 77–92, feb 2004.

[52] A. Fleming and K. Leang, "Charge drives for scanning probe microscope positioning stages," *Ultramicroscopy*, vol. 108, pp. 1551–1557, nov 2008.

[53] A. J. Fleming, "A megahertz bandwidth dual amplifier for driving piezoelectric actuators and other highly capacitive loads," *Rev. Sci. Instrum.*, vol. 80, no. 10, p. 104701, 2009.

[54] A. J. Fleming, "Precision charge drive with low frequency voltage feedback for linearization of piezoelectric hysteresis," *Proc. Am. Control Conf.*, pp. 6022–6026, 2013.

[55] K. Miyata, S. Usho, S. Yamada, S. Furuya, K. Yoshida, H. Asakawa, and T. Fukuma, "Separate-type scanner and wideband high-voltage amplifier for atomic-resolution and high-speed atomic force microscopy," *Rev. Sci. Instrum.*, vol. 84, no. 4, p. 043705, 2013.

[56] G. Schitter, F. Allgöwer, and A. Stemmer, "A new control strategy for high-speed atomic force microscopy," *Nanotechnology*, vol. 15, pp. 108–114, jan 2004.

[57] T. Uchihashi, N. Kodera, H. Itoh, H. Yamashita, and T. Ando, "Feed-Forward Compensation for High-Speed Atomic Force Microscopy Imaging of Biomolecules," *Jpn. J. Appl. Phys.*, vol. 45, pp. 1904–1908, mar 2006.

[58] N. Kodera, M. Sakashita, and T. Ando, "Dynamic proportional-integral-differential controller for high-speed atomic force microscopy," *Rev. Sci. Instrum.*, vol. 77, no. 8, p. 083704, 2006.

[59] G. Schitter, P. Menold, H. F. Knapp, F. Allgower, and A. Stemmer, "High performance feedback for fast scanning atomic force microscopes," *Rev. Sci. Instrum.*, vol. 72, no. 8, p. 3320, 2001.

[60] S. Salapaka, A. Sebastian, J. P. Cleveland, and M. V. Salapaka, "High bandwidth nano-positioner: A robust control approach," *Rev. Sci. Instrum.*, vol. 73, no. 9, p. 3232, 2002.

[61] N. Chuang, "Robust H-infinity control of variable-speed wind turbines in partial load," in *2014 Australas. Univ. Power Eng. Conf.*, no. 3, pp. 1–6, IEEE, sep 2014.

[62] Hiroshi Fujimoto and Takashi Oshima, "Nanoscale servo control of contact-mode AFM with surface topography learning observer," in *2008 10th IEEE Int. Work. Adv. Motion Control*, pp. 568–573, IEEE, mar 2008.

[63] Ying Wu, Qingze Zou, and Chanmin Su, "A current cycle feedback iterative learning control approach to AFM imaging," in *2008 Am. Control Conf.*, vol. 8, pp. 2040–2045, IEEE, jun 2008.

[64] U. Aridogan, Y. Shan, and K. K. Leang, "Design and Analysis of Discrete-Time Repetitive Control for Scanning Probe Microscopes," *J. Dyn. Syst. Meas. Control*, vol. 131, no. 6, p. 061103, 2009.

[65] S. Necipoglu, S. a. Cebeci, Y. E. Has, L. Guvenc, and C. Basdogan, "Robust Repetitive Controller for Fast AFM Imaging," *IEEE Trans. Nanotechnol.*, vol. 10, pp. 1074–1082, sep 2011.

[66] G. Meyer and N. M. Amer, "Novel optical approach to atomic force microscopy," *Appl. Phys. Lett.*, vol. 53, no. 12, p. 1045, 1988.

[67] T. Fukuma, M. Kimura, K. Kobayashi, K. Matsushige, and H. Yamada, "Development of low noise cantilever deflection sensor for multienvironment frequency-modulation atomic force microscopy," *Rev. Sci. Instrum.*, vol. 76, no. 5, p. 053704, 2005.

[68] D. Rugar, H. J. Mamin, and P. Guethner, "Improved fiber-optic interferometer for atomic force microscopy," *Appl. Phys. Lett.*, vol. 55, no. 25, p. 2588, 1989.

[69] B. W. Hoogenboom, P. L. T. M. Frederix, D. Fotiadis, H. J. Hug, and A. Engel, "Potential of interferometric cantilever detection and its application for SFM/AFM in liquids," *Nanotechnology*, vol. 19, p. 384019, sep 2008.

[70] J. Brügger, R. A. Buser, and N. F. de Rooij, "Micromachined atomic force microprobe with integrated capacitive read-out," *J. Micromech. Microeng.*, vol. 2, p. 218, 1992.

[71] N. Blanc, "Scanning force microscopy in the dynamic mode using microfabricated capacitive sensors," *J. Vac. Sci. Technol. B*, vol. 14, p. 901, 1996.

[72] E. Forsen, G. Abadal, S. Ghatnekar-Nilsson, J. Teva, J. Verd, R. Sandberg, W. Svendsen, F. Perez-Murano, J. Esteve, E. Figueras, F. Campabadal, L. Montelius, N. Barniol, and A. Boisen, "Ultrasensitive mass sensor fully integrated with complementary metal-oxide-semiconductor circuitry," *Appl. Phys. Lett.*, vol. 87, no. 4, p. 043507, 2005.

[73] J. U. N. Kim, *Electronic noise in nanostructures : limitations and sensing applications.* Phd thesis, Texas A&M University, Seoul National University, 2006.

[74] J. Verd, A. Uranga, G. Abadal, J. Teva, F. Torres, F. Perez-Murano, J. Fraxedas, J. Esteve, and N. Barniol, "Monolithic mass sensor fabricated using a conventional technology with attogram resolution in air conditions," *Appl. Phys. Lett.*, vol. 91, no. 1, p. 013501, 2007.

[75] M. Tortonese, R. C. Barrett, and C. F. Quate, "Atomic resolution with an atomic force microscope using piezoresistive detection," *Appl. Phys. Lett.*, vol. 62, no. 8, p. 834, 1993.

[76] R. Linnemann, T. Gotszalk, L. Hadjiiski, and I. Rangelow, "Characterization of a cantilever with an integrated deflection sensor," *Thin Solid Films*, vol. 264, p. 159, 1995.

[77] R. Jumpertz, A. Hart, O. Ohlsson, F. Saurenbach, and J. Schelten, "Piezoresistive sensors on AFM cantilevers with atomic resolution," *Microelectron Eng*, vol. 41-41, p. 441, 1998.

[78] J. Thaysen, "Atomic force microscopy probe with piezoresistive read-out and a highly symmetrical Wheatstone bridge arrangement," *Sensors Actuators A Phys.*, vol. 83, pp. 47–53, may 2000.

[79] X. Yu, J. Thaysen, O. Hansen, and A. Boisen, "Optimization of sensitivity and noise in piezoresistive cantilevers," *J. Appl. Phys.*, vol. 92, no. 10, pp. 6296–6301, 2002.

[80] G. Yoshikawa, H.-P. Lang, T. Akiyama, L. Aeschimann, U. Staufer, P. Vettiger, M. Aono, T. Sakurai, and C. Gerber, "Sub-ppm detection of vapors using piezoresistive microcantilever array sensors.," *Nanotechnology*, vol. 20, p. 015501, jan 2009.

[81] J. C. Doll and B. L. Pruitt, "High-bandwidth piezoresistive force probes with integrated thermal actuation," *J Micromech Microeng*, vol. 22, p. 095012, 2012.

[82] G. Tosolini, F. Scarponi, S. Cannistraro, and J. Bausells, "Biomolecule recognition using piezoresistive nanomechanical force probes," *Appl. Phys. Lett.*, vol. 102, no. 25, p. 253701, 2013.

[83] J. Bausells, "Piezoresistive cantilevers for nanomechanical sensing," *Microelectron. Eng.*, vol. 145, pp. 9–20, 2015.

[84] T. Itoh and T. Suga, "Development of a force sensor for atomic force microscopy using piezoelectric thin films," *Nanotechnology*, vol. 4, p. 218, 1993.

[85] J. H. Lee, K. S. Hwang, J. Park, K. H. Yoon, D. S. Yoon, and T. S. Kim, "Immunoassay of prostate-specific antigen (PSA) using resonant frequency shift of piezoelectric nanomechanical microcantilever," *Biosens. Bioelectron.*, vol. 20, no. 10 SPEC. ISS., pp. 2157–2162, 2005.

[86] R. B. Karabalin, M. H. Matheny, X. L. Feng, E. Defay, G. Le Rhun, C. Marcoux, S. Hentz, P. Andreucci, and M. L. Roukes, "Piezoelectric nanoelectromechanical

resonators based on aluminum nitride thin films," *Appl. Phys. Lett.*, vol. 95, no. 10, p. 103111, 2009.

[87] P. Ivaldi, J. Abergel, M. H. Matheny, L. G. Villanueva, R. B. Karabalin, M. L. Roukes, P. Andreucci, S. Hentz, and E. Defaÿ, "50 nm thick AlN film-based piezoelectric cantilevers for gravimetric detection," *J. Micromechanics Microengineering*, vol. 21, p. 085023, aug 2011.

[88] a. N. Cleland and M. L. Roukes, "Fabrication of high frequency nanometer scale mechanical resonators from bulk Si crystals," *Appl. Phys. Lett.*, vol. 69, no. 18, pp. 2653–2655, 1996.

[89] K. L. Ekinci, Y. T. Yang, and M. L. Roukes, "Ultimate limits to inertial mass sensing based upon nanoelectromechanical systems," *J. Appl. Phys.*, vol. 95, no. 5, p. 2682, 2004.

[90] A. Johansson, G. Blagoi, and A. Boisen, "Polymeric cantilever-based biosensors with integrated readout," *Appl. Phys. Lett.*, vol. 89, no. 17, p. 173505, 2006.

[91] A. Li, P. Y. Lee, B. Ho, J. L. Ding, and C. T. Lim, "Atomic force microscopy study of the antimicrobial action of Sushi peptides on Gram negative bacteria," *Biochim. Biophys. Acta*, vol. 1768, no. 3, pp. 411–418, 2007.

[92] A. Schneider, R. H. Ibbotson, R. J. Dunn, and E. Huq, "Arrays of SU-8 microcantilevers with integrated piezoresistive sensors for parallel AFM applications," *Microelectron. Eng.*, vol. 88, no. 8, pp. 2390–2393, 2011.

[93] G. Shekhawat, S.-H. Tark, and V. P. Dravid, "MOSFET-Embedded microcantilevers for measuring deflection in biomolecular sensors.," *Science*, vol. 311, pp. 1592–5, mar 2006.

[94] H. T. a. Brenning, S. E. Kubatkin, D. Erts, S. G. Kafanov, T. Bauch, and P. Delsing, "A single electron transistor on an atomic force microscope probe.," *Nano Lett.*, vol. 6, pp. 937–941, may 2006.

[95] P. J. Koppinen, J. T. Lievonen, M. Ahlskog, and I. J. Maasilta, "Strain sensing with submicron Al-AlO(x)-Al tunnel junctions.," *Rev. Sci. Instrum.*, vol. 81, p. 023901, feb 2010.

[96] G. Tosolini, G. Villanueva, F. Perez-Murano, and J. Bausells, "Silicon microcantilevers with MOSFET detection," *Microelectron. Eng.*, vol. 87, no. 5-8, pp. 1245–1247, 2010.

[97] M. Huth, F. Porrati, C. Schwalb, M. Winhold, R. Sachser, M. Dukic, J. Adams, and G. Fantner, "Focused electron beam induced deposition: A perspective.," *Beilstein J. Nanotechnol.*, vol. 3, pp. 597–619, jan 2012.

[98] J. L. Arlett, J. R. Maloney, B. Gudlewski, M. Muluneh, and M. L. Roukes, "Self-Sensing Micro- and Nanocantilevers with Attonewton-Scale Force Resolution," *Nano Lett.*, vol. 6, pp. 1000–1006, may 2006.

[99] R. Enning, *High Frequency Atomic Force Microscopy.* PhD thesis, ETH Zürich, 2011.

[100] Y. Xiao-mei, J. Xing-liu, J. Thaysen, O. Hansen, and A. Boisen, "Noise and sensitivity in polysilicon piezoresistive cantilevers," *Chinese Physics*, vol. 10, p. 918, 2001.

[101] G. Villanueva, J. Bausells, J. Montserrat, and F. Pérez-Murano, "Polysilicon piezoresistive cantilevers for intermolecular force detection," in *2005 Spanish Conf. Electron Devices, Proc.*, vol. 2005, pp. 495–498, 2005.

[102] R. Katragadda, Z. Wang, W. Khalid, Y. Li, and Y. Xu, "Parylene cantilevers integrated with polycrystalline silicon piezoresistors for surface stress sensing," *Appl. Phys. Lett.*, vol. 91, no. 8, p. 083505, 2007.

[103] N. S. Kale, S. Nag, R. Pinto, and V. R. Rao, "Fabrication and characterization of a polymeric microcantilever with an encapsulated hotwire CVD polysilicon piezoresistor," *J. Microelectromechanical Syst.*, vol. 18, no. 1, pp. 79–87, 2009.

[104] J. C. Doll and B. L. Pruitt, "Design of piezoresistive versus piezoelectric contact mode scanning probes," *J. Micromechanics Microengineering*, vol. 20, p. 095023, sep 2010.

[105] S. P. Beeby, G. Ensel, M. Kraft, and N. White, *MEMS Mechanical Sensors*. Artech House, Inc., 2004.

[106] N. Kodera, D. Yamamoto, R. Ishikawa, and T. Ando, "Video imaging of walking myosin V by high-speed atomic force microscopy.," *Nature*, vol. 468, pp. 72–6, nov 2010.

[107] P. K. Hansma, B. Drake, J. Thompson, J. H. Kindt, and D. Hale, "United States Patent: Measurement head for atomic force microscopy and other applications," 2005.

[108] M. Antognozzi, A. Ulcinas, L. Picco, S. H. Simpson, P. J. Heard, M. D. Szczelkun, B. Brenner, and M. J. Miles, "A new detection system for extremely small vertically mounted cantilevers.," *Nanotechnology*, vol. 19, p. 384002, sep 2008.

[109] B. Sanii and P. D. Ashby, “High Sensitivity Deflection Detection of Nanowires,” *Phys. Rev. Lett.*, vol. 104, p. 147203, apr 2010.

[110] K. Srinivasan, H. Miao, M. T. Rakher, M. Davanco, and V. Aksyuk, “Optomechanical transduction of an integrated silicon cantilever probe using a microdisk resonator,” *Nano Lett.*, vol. 11, pp. 791–797, sep 2010.

[111] C. H. Schwalb, C. Grimm, M. Baranowski, R. Sachser, F. Porrati, H. Reith, P. Das, J. Müller, F. Völklein, A. Kaya, and M. Huth, “A tunable strain sensor using nanogranular metals.,” *Sensors*, vol. 10, pp. 9847–56, jan 2010.

[112] B. Ilic, “Attogram detection using nanoelectromechanical oscillators,” *J. Appl. Phys.*, vol. 95, no. 7, p. 3694, 2004.

[113] D. Rugar, R. Budakian, H. J. Mamin, and B. W. Chui, “Single spin detection by magnetic resonance force microscopy.,” *Nature*, vol. 430, pp. 329–332, 2004.

[114] F. Huber, H. P. Lang, N. Backmann, D. Rimoldi, and C. Gerber, “Direct detection of a BRAF mutation in total RNA from melanoma cells using cantilever arrays.,” *Nat. Nanotechnol.*, vol. 8, no. 2, pp. 125–9, 2013.

[115] F. Huber, H. P. Lang, and C. Gerber, “Nanomechanical sensors: Measuring a response in blood.,” *Nat. Nanotechnol.*, vol. 9, pp. 165–7, mar 2014.

[116] R. Sachser, F. Porrati, C. H. Schwalb, and M. Huth, “Universal Conductance Correction in a Tunable Strongly Coupled Nanogranular Metal,” *Phys. Rev. Lett.*, vol. 107, p. 206803, nov 2011.

[117] G. Anetsberger, O. Arcizet, Q. P. Unterreithmeier, R. Rivière, A. Schliesser, E. M. Weig, J. P. Kotthaus, and T. J. Kippenberg, “Near-field cavity optomechanics with nanomechanical oscillators,” *Nat. Phys.*, vol. 5, pp. 909–914, oct 2009.

[118] J. D. Adams, C. H. Schwalb, M. Winhold, M. Đukić, M. Huth, and G. E. Fantner, “Analysis of local deformation effects in resistive strain sensing of a submicron-thickness AFM cantilever,” in *Proc. SPIE Microtechnologies, Smart Sensors, Actuators, MEMS*, vol. 8763, p. 876327, may 2013.

[119] J. D. Adams, A. Nievergelt, B. W. Erickson, C. Yang, M. Dukic, and G. E. Fantner, “High-speed imaging upgrade for a standard sample scanning atomic force microscope using small cantilevers.,” *Rev. Sci. Instrum.*, vol. 85, p. 093702, sep 2014.

[120] M. Dukic, M. Winhold, C. H. Schwalb, J. Adams, M. Huth, V. Stavrov, and G. E. Fantner, “Self-sensing cantilevers for AFM using nano granular tunneling resistors for deflection readout,” in *Abstr. 40th Int. Conf. Micro Nano Eng.*, 2014.

[121] M. Dukic, M. Winhold, C. H. Schwalb, J. D. Adams, V. Stavrov, M. Huth, and G. E. Fantner, "Additive rapid prototyping of nanogranular strain sensors for micro- and nanomechanical resonators,"

[122] I. Utke, P. Hoffmann, and J. Melngailis, "Gas-assisted focused electron beam and ion beam processing and fabrication," *J. Vac. Sci. Technol. B*, vol. 26, no. 4, p. 1197, 2008.

[123] I. Beloborodov, a. Lopatin, V. Vinokur, and K. Efetov, "Granular electronic systems," *Rev. Mod. Phys.*, vol. 79, pp. 469–518, apr 2007.

[124] M. Huth, "Granular metals: From electronic correlations to strain-sensing applications," *J. Appl. Phys.*, vol. 107, no. 11, p. 113709, 2010.

[125] J. Zhang and B. Shklovskii, "Density of states and conductivity of a granular metal or an array of quantum dots," *Phys. Rev. B*, vol. 70, p. 115317, sep 2004.

[126] I. Bargatin, E. B. Myers, J. Arlett, B. Gudlewski, and M. L. Roukes, "Sensitive detection of nanomechanical motion using piezoresistive signal downmixing," *Appl. Phys. Lett.*, vol. 86, no. 13, p. 133109, 2005.

[127] H. J. Butt and M. Jaschke, "Calculation of thermal noise in atomic force microscopy," *Nanotechnology*, vol. 6, pp. 1–7, jan 1995.

[128] O. Hansen and A. Boisen, "Noise in piezoresistive atomic force microscopy," 1999.

[129] B. Schultrich, H.-J. Scheibe, G. Grandremy, and D. Schneider, "Elastic Modulus of Amorphous Carbon Films," *Phys. Status Solidi*, vol. 145, pp. 385–392, oct 1994.

[130] S. Cho, I. Chasiotis, T. a. Friedmann, and J. P. Sullivan, "Young's modulus, Poisson's ratio and failure properties of tetrahedral amorphous diamond-like carbon for MEMS devices," *J. Micromechanics Microengineering*, vol. 15, pp. 728–735, apr 2005.

[131] Y. Cui, Q. Wei, H. Park, and C. M. Lieber, "Nanowire nanosensors for highly sensitive and selective detection of biological and chemical species.," *Science*, vol. 293, no. 5533, pp. 1289–1292, 2001.

[132] S. Alexander, L. Hellemans, O. Marti, J. Schneir, V. Elings, P. K. Hansma, M. Longmire, and J. Gurley, "An atomic-resolution atomic-force microscope implemented using an optical lever," *J. Appl. Phys.*, vol. 65, no. 1, pp. 164–167, 1989.

[133] M. Dukic, J. D. Adams, and G. E. Fantner, "Piezoresistive AFM cantilevers surpassing standard optical beam deflection in low noise topography imaging," *Sci. Rep.*, vol. 5, p. 16393, nov 2015.

[134] S. C. Minne, S. R. Manalis, and C. F. Quate, *Bringing Scanning Probe Microscopy Up to Speed.* Springer US, 1999.

[135] D. Sarid, *Scanning force microscopy.* New York: Oxford University Press, 1994.

[136] T. Fukuma and S. P. Jarvis, "Development of liquid-environment frequency modulation atomic force microscope with low noise deflection sensor for cantilevers of various dimensions," *Rev. Sci. Instrum.*, vol. 77, no. 4, p. 043701, 2006.

[137] R. Lévy and M. Maaloum, "Measuring the spring constant of atomic force microscope cantilevers: thermal fluctuations and other methods," *Nanotechnology*, vol. 13, p. 33, 2002.

[138] B. Ohler, "Cantilever spring constant calibration using laser Doppler vibrometry.," *Rev. Sci. Instrum.*, vol. 78, p. 063701, jun 2007.

[139] M. Shusteff, T. P. Burg, and S. R. Manalis, "Measuring Boltzmann's constant with a low-cost atomic force microscope: An undergraduate experiment,"*Am. J. Phys.*, vol. 74, p. 873, 2006.

[140] R. Garcia, *Amplitude modulation atomic force microscopy.* WILEY-VCH, 2010.

[141] T. Ando, T. Uchihashi, and T. Fukuma, "High-speed atomic force microscopy for nano-visualization of dynamic biomolecular processes," *Prog. Surf. Sci.*, vol. 83, pp. 337–437, nov 2008.

[142] P. C. D. Hobbs, "Photodiode Front Ends: The Real Story," *Opt. Photonics News*, vol. 12, no. 4, pp. 42–45, 2001.

[143] S.-J. Park, J. C. Doll, and B. L. Pruitt, "Piezoresistive Cantilever Performance-Part I: Analytical Model for Sensitivity.," *J. Microelectromech. Syst.*, vol. 19, pp. 137–148, feb 2010.

[144] D. Nečas and P. Klapetek, "Gwyddion: an open-source software for SPM data analysis," *Open Phys.*, vol. 10, p. 181, 2012.

[145] "Bruker MultiMode 8 Atomic Force Microscope Brochure."

[146] R. García and R. Pérez, "Dynamic atomic force microscopy methods,"*Surf. Sci. Rep.*, vol. 47, p. 197, 2002.

[147] R. García and A. San Paulo, "Attractive and repulsive tip-sample interaction regimes in tapping-mode atomic force microscopy," *Phys. Rev. B*, vol. 60, p. 4961, 1999.

[148] J. Kokavecz, Z. L. Horvath, and A. Mechler, "Dynamical properties of the Q-controlled atomic force microscope," *Appl. Phys. Lett.*, vol. 85, no. 15, pp. 3232–3234, 2004.

[149] American Society for Testing and Materials, "Standard Practice for Conversion Between Resistivity and Dopant Density for Boron-Doped, Phosphorous-Doped, and Arsenic-Doped Silicon," *Annu. B. ASTM Stand.*, vol. F 723-99, pp. 1–7, 1999.

[150] J. Harley and T. Kenny, "1/f noise considerations for the design and process optimization of piezoresistive cantilevers," *J. Microelectromechanical Syst.*, vol. 9, pp. 226–235, jun 2000.

[151] H. Hosaka, K. Itao, and S. Kuroda, "Damping characteristics of beam-shaped micro-oscillators," *Sensor Actuat A-Phys*, vol. 49, p. 87, 1995.

[152] J. Lübbe, M. Temmen, H. Schnieder, and M. Reichling, "Measurement and modelling of non-contact atomic force microscope cantilever properties from ultra-high vacuum to normal pressure conditions," *Meas. Sci. Technol.*, vol. 22, p. 055501, may 2011.

[153] F. Giessibl, "Atomic resolution on Si(111)-(7×7) by noncontact atomic force microscopy with a force sensor based on a quartz tuning fork," *Appl. Phys. Lett.*, vol. 76, no. 111, pp. 1470–1472, 2000.

[154] G. E. Fantner, W. Schumann, R. J. Barbero, A. Deutschinger, V. Todorov, D. S. Gray, A. M. Belcher, I. W. Rangelow, and K. Youcef-Toumi, "Use of self-actuating and self-sensing cantilevers for imaging biological samples in fluid.," *Nanotechnology*, vol. 20, p. 434003, oct 2009.

[155] L. Aeschimann, A. Meister, T. Akiyama, B. W. Chui, P. Niedermann, H. Heinzelmann, N. F. De Rooij, U. Staufer, and P. Vettiger, "Scanning probe arrays for life sciences and nanobiology applications," *Microelectron. Eng.*, vol. 83, no. 4-9 SPEC. ISS., pp. 1698–1701, 2006.

[156] V. Aggarwal, Meng Mao, and U.-M. O'Reilly, "A Self-Tuning Analog Proportional-Integral-Derivative (PID) Controller," in *First NASA/ESA Conf. Adapt. Hardw. Syst.*, vol. 2006, pp. 12–19, IEEE, 2006.

[157] Yifan Sun, Y. Fang, Yudong Zhang, and Xiaokun Dong, "Field programmable gate array (FPGA) based embedded system design for AFM real-time control," in *2010 IEEE Int. Conf. Control Appl.*, pp. 245–250, IEEE, sep 2010.

[158] I. Lita, D. A. Visan, and I. B. Cioc, "FPAA based PID controller with applications in the nuclear domain," in *2009 32nd Int. Spring Semin. Electron. Technol.*, no. 1, pp. 1–4, IEEE, may 2009.

[159] Y. K. Yong, B. Bhikkaji, and S. O. R. Reza Moheimani, "Design, Modeling, and FPAA-Based Control of a High-Speed Atomic Force Microscope Nanopositioner," *IEEE/ASME Trans. Mechatronics*, vol. 18, pp. 1060–1071, jun 2013.

[160] G. Schitter and N. Phan, "Field Programmable Analog Array (FPAA) based control of an Atomic Force Microscope," in *2008 Am. Control Conf.*, pp. 2690–2695, IEEE, jun 2008.

[161] Anadigm, "AnadigmDesigner®2: User manual," 2004.

[162] G. Schitter, K. J. Astrom, B. E. DeMartini, P. J. Thurner, K. L. Turner, and P. K. Hansma, "Design and Modeling of a High-Speed AFM-Scanner," *IEEE Trans. Control Syst. Technol.*, vol. 15, pp. 906–915, sep 2007.

[163] R. Ugodzi, R. Szewczyk, and M. Nowicki, *Intelligent Systems 2014: Analog PID Controller with the Digitally Controled Parameters*, vol. 323 of *Advances in Intelligent Systems and Computing.* Cham: Springer International Publishing, 2015.

[164] A. P. Nievergelt, J. D. Adams, P. D. Odermatt, and G. E. Fantner, "High-frequency multimodal atomic force microscopy," *Beilstein J. Nanotechnol.*, vol. 5, pp. 2459–2467, dec 2014.

[165] G. E. Fantner, P. Hegarty, J. H. Kindt, G. Schitter, G. a. G. Cidade, and P. K. Hansma, "Data acquisition system for high speed atomic force microscopy," *Rev. Sci. Instrum.*, vol. 76, no. 2, p. 026118, 2005.

[166] T. Ando, N. Kodera, Y. Naito, T. Kinoshita, K. Furuta, and Y. Y. Toyoshima, "A High-speed Atomic Force Microscope for Studying Biological Macromolecules in Action," *ChemPhysChem*, vol. 4, pp. 1196–1202, nov 2003.

[167] T. R. Albrecht, "Microfabrication of cantilever styli for the atomic force microscope," *J. Vac. Sci. Technol. A Vacuum, Surfaces, Film.*, vol. 8, p. 3386, jul 1990.

[168] D. a. Walters, J. P. Cleveland, N. H. Thomson, P. K. Hansma, M. a. Wendman, G. Gurley, and V. Elings, "Short cantilevers for atomic force microscopy," *Rev. Sci. Instrum.*, vol. 67, no. 10, p. 3583, 1996.

[169] L. Picas, F. Rico, and S. Scheuring, "Direct Measurement of the Mechanical Properties of Lipid Phases in Supported Bilayers," *Biophys. J.*, vol. 102, pp. L01–L03, jan 2012.

[170] M. Jaafar, D. Martínez-Martín, M. Cuenca, J. Melcher, A. Raman, and J. Gómez-Herrero, "Drive-amplitude-modulation atomic force microscopy: From vacuum to liquids," *Beilstein J. Nanotechnol.*, vol. 3, pp. 336–344, apr 2012.

[171] R. W. Stark, N. Naujoks, and A. Stemmer, "Multifrequency electrostatic force microscopy in the repulsive regime," *Nanotechnology*, vol. 18, p. 065502, feb 2007.

[172] X. D. Ding, J. An, J. B. Xu, C. Li, and R. Y. Zeng, "Improving lateral resolution of electrostatic force microscopy by multifrequency method under ambient conditions," *Appl. Phys. Lett.*, vol. 94, no. 22, p. 223109, 2009.

[173] J. W. Li, J. P. Cleveland, and R. Proksch, "Bimodal magnetic force microscopy: Separation of short and long range forces," *Appl. Phys. Lett.*, vol. 94, no. 16, p. 163118, 2009.

[174] S. Kawai, T. Glatzel, S. Koch, B. Such, A. Baratoff, and E. Meyer, "Systematic Achievement of Improved Atomic-Scale Contrast via Bimodal Dynamic Force Microscopy," *Phys. Rev. Lett.*, vol. 103, p. 220801, nov 2009.

[175] A. X. Cartagena-Rivera, W.-H. Wang, R. L. Geahlen, and A. Raman, "Fast, multi-frequency, and quantitative nanomechanical mapping of live cells using the atomic force microscope," *Sci. Rep.*, vol. 5, p. 11692, jun 2015.

[176] H.-A. Eskandarian, P. D. Odermatt, J. Ven, J. McKinney, and G. E. Fantner, "TIME RESOLVED ATOMIC FORCE MICROSCOPY IMAGING OF BIOLOGICAL," in *Int. Scanning Probe Microsc. Conf.*, (Rio de Janeiro), 2015.

[177] "Nanosurf: Super-flat AFM for SEM."

[178] J. M. Gere and B. J. Goodno, *Mechanics of materials.* Cengage Learning, seventh ed ed., 2009.

Appendix A

Appendix

A.1 Relation between angle and free end deflection

A cantilever deflection Δz and bending angle θ along the cantilever length, coming from a point load F acting on the free end, are [178]

$$\Delta z\left(x\right) = \frac{Fl^3}{6EI}\cdot\left[3\left(\frac{x}{l}\right)^2-\left(\frac{x}{l}\right)^3\right] \tag{A.1}$$

$$\theta\left(x\right) = \frac{Fl^2}{2EI}\cdot\left[2\left(\frac{x}{l}\right)-\left(\frac{x}{l}\right)^2\right] \tag{A.2}$$

where l is the cantilever length, x is the position along the cantilever length (starting from the fixed end), E is Young's modulus of the cantilever material along its length and I is the moment of inertia of the cantilever cross section about its neutral axis. The laser beam used in OBD readout is a Gaussian beam, and it is common to define the laser beam diameter as a point where the laser intensity falls to a fraction $1/e^2$ of its initial intensity. We will denote l_b as the laser beam diameter along the cantilever length. In order to reflect most of the laser power off of the cantilever surface, the optimal position of the center of the laser beam spot, along the cantilever length is $x_0 \approx l-l_b/2$. Inputting x_0 in equation (A.2) and expressing it in terms of $\Delta z\left(l\right)$ we get the equation

$$\theta\left(l-\frac{l_b}{2}\right)=\frac{3}{2l}\left(1-\left(\frac{l_b}{2l}\right)^2\right)\cdot\Delta z\left(l\right) \tag{A.3}$$

A.2 Where NTRs outperform optical detection

Here we consider as the signal-to-noise ratio (SNR) the total thermomechanical peak height p_{tm} versus the baseline noise floor. Both NTR Johnson noise and optical beam deflection photodetector shot noise may be considered as white noise sources with noise floor n and ripple δ. The total peak height of the thermomechanical peak is the square root of the sum of the squared thermomechanical noise t_{tm} and the white noise

$$p_{tm} = \sqrt{t_{tm}^2 + n^2} \tag{A.4}$$

The SNR is then the height of the peak above the baseline, divided by the ripple in the noise floor

$$SNR = \frac{p_{tm} - n}{\delta} = \frac{\sqrt{\left(\frac{t_{tm}}{n}\right)^2 + 1} - 1}{\frac{\delta}{n}} \tag{A.5}$$

Assuming both optical and NTR deflection detection are measured with similar conditions (measurement bandwidth, averaging time) the ratio δ/n can be considered equal between optical and NTR detection; therefore the ratio of SNRs can be expressed as

$$\frac{SNR_{NTR}}{SNR_{OPT}} = \frac{\sqrt{\left(\frac{t_{tm}^{NTR}}{n_{NTR}}\right)^2 + 1} - 1}{\sqrt{\left(\frac{t_{tm}^{OPT}}{n_{OPT}}\right)^2 + 1} - 1} \tag{A.6}$$

In length units the Johnson noise density of the NTR sensor may be estimated from the Johnson noise density of the resistor scaled by the deflection sensitivity of the NTR Wheatstone bridge, which for small deflections may be expressed as [111]

$$\frac{dV_G}{d\Delta z} = \frac{3\kappa V_S \left(1 - \frac{l_g}{2l}\right) t}{8l^2} \tag{A.7}$$

where V_G is the Wheatstone bridge voltage, z is the cantilever end deflection, κ the NTR gauge factor, V_s the Wheatstone bridge supply voltage, l_g the length between contacts of the NTR sensor, l the cantilever length, and t the cantilever thickness. The Johnson noise of the NTR element is then

$$n_{NTR} = \frac{8l^2\sqrt{4k_B T R_{NTR}}}{3\kappa V_s \left(1 - \frac{l_g}{2l}\right) t} \tag{A.8}$$

where k_B is the Boltzmann constant, T the temperature of the sensor (assumed 298 K), and R_{NTR} the resistance of the NTR element. The noise floor of the optical beam

deflection system is given by [136]

$$n_{OPT} = \frac{la}{3s}\sqrt{\frac{2e}{SP}} \tag{A.9}$$

where a is the size of the laser spot on the photodetector, s the distance from the cantilever to the photodetector, e the electron charge, S the photosensitivity of the photodetector, and P the laser power at the photodetector. For practical geometrical parameters (see Table A.1), this noise floor is about $50\,\mathrm{fm}/\sqrt{\mathrm{Hz}}$ at $0.5\,\mathrm{mW}$ of laser power at the photodetector. The thermal peak for the optical deflection measurement is given by

$$t_{tm}^{OPT} = \sqrt{\frac{1.634 k_B T Q}{\pi k f_0}} \tag{A.10}$$

and for the NTR deflection by

$$t_{tm}^{NTR} = \sqrt{\frac{2 k_B T Q}{\pi k f_0}} \tag{A.11}$$

The difference is due to the optical system measuring an angle change as opposed to a displacement [127]. The cantilever resonance frequency f_0, spring constant k and quality factor Q are calculated from

$$f_0 = 0.1615\frac{t}{l^2}\sqrt{\frac{E}{\rho}}, \qquad k = \frac{Ewt^3}{4l^3}, \qquad Q = \frac{4\rho t w f_0}{6\eta + 3w\sqrt{\eta \frac{M}{RT}\pi f_0 p}} \tag{A.12}$$

where E is the cantilever Young's modulus, ρ the cantilever density, w the cantilever width, η the viscosity of the surrounding medium (air), M the molecular mass of air, R the universal gas constant and p the pressure of the surrounding medium (assumed $1\,\mathrm{atm}$).

In order to simplify the parameter space, we assume a cantilever planar shape such that $l = 3w$. Table A.1 lists values of the relevant parameters. Figure A.1 illustrates the regions where $SNR_{OPT} > SNR_{NTR}$ and where $SNR_{NTR} > SNR_{OPT}$. Starting below $3\,\mu\mathrm{m}$ length, there exists a broad range of cantilever geometries where the expected NTR signal to noise ratio is larger than the optical signal to noise ratio. This NTR performance advantage becomes especially prominent at submicron cantilever lengths, in addition to the extreme practical limitations of optically detecting these cantilevers.

Table A.1: Parameters used in calculation of the expected relative SNR performance of NTR sensors versus OBD detection

Parameter	**Value**
E (silicon nitride)	250 GPa
ρ (silicon nitride)	3100 kg/m^3
η (air)	18.6×10^{-6} Pa · s
M (air)	0.028 97 kg/mol
k	8
R_{NTR}	300 Ω
V_S	0.4 V
l_g	40 nm
a	2 mm
s	1 cm
l (for calculation of n_{OPT} only)	20 µm
S	0.45 A/W
P	0.5 m W

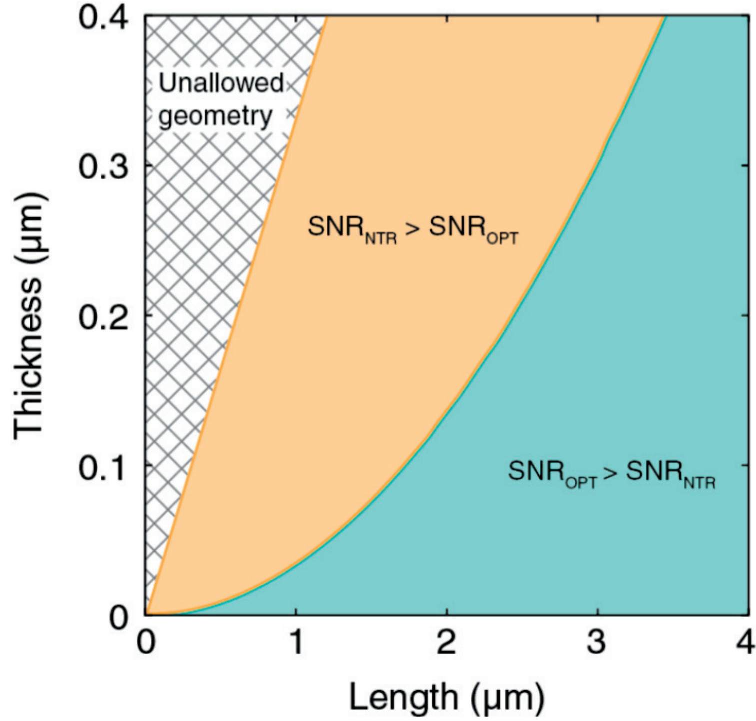

Figure A.1: Parameter space of cantilever length and thickness comparing the SNR of optical and NTR deflection detection. The region marked in green indicates expected geometries where optical sensing outperforms NTR sensing, if optical detection were practical to implement for these cantilever geometries. The region marked in yellow indicates where NTR sensing is expected to outperform optical sensing. Unallowed geometries are such that the cantilever thickness would exceed the width.

Maja Dukic Pjanic

Ch. de Champ-Fleuri 22
1022 Chavannes, Switzerland
maja.dukic.pjanic@gmail.com
+41 78 8982187

Electrical engineer, PhD in Microengineering (EPFL), specialized in MEMS/NEMS and AFM
Expert in measurements, sensors, electronics, signal processing and sensor communication.

Education

09/2011 – present (expect to finish 05/2016)	**EPFL, PhD in Microengineering** Laboratory for bio- and nano-instrumentation (LBNI)
09/2004 – 07/2010	**MSc in Electronics Engineering** School of Electrical Engineering, University of Belgrade, Serbia GPA **9.6/10 – top 10%** (full scale 1-10, passing grade 6-10)
2000 – 2004	**Mathematical Highschool**, Belgrade, Serbia Elite high school for children gifted in math, physics and programming

Work experience

09/2011 - present	**EPFL,** Researcher Laboratory for bio- and nano-instrumentation (LBNI) *Developed electrical readout and mechanical interface for various self-sensing AFM cantilevers, in collaboration with several SMEs. The first AFM application of nanogranular tunneling resistors.*
02/2011 – 04/2011	**EPFL** (2-month internship) Laboratory for bio- and nano-instrumentation (LBNI) *Developing PID controller for high speed AFM, both in FPGA and analog electronics design.*
01/2009 – 09/2011	**Centre of Microelectronic Technologies**, Researcher University of Belgrade, Serbia *Working on microcantilever sensors under the framework of EU FP7 project REGMINA.*

Technical Skills

Electrical engineering	Analog and digital electronics design, sensor interfacing, embedded systems, real-time systems, microcontroller programming (MSP430, PIC), network protocols, signal processing, FPGA programing (basic)
Mechanical engineering	FEM analysis, CAD design, CNC machining, microfabrication (basic)
Programming languages	C/C++, VHDL, Assembly (8086, MSP430), Prolog, Pascal

Packages	Matlab, Simulink, Eagle PCB Software, IAR Embedded Workbench, NI LabWindows/CVI, NI LabView, Xilinx ISE, LTSpice, Bruker Nanoscope, Gwyddion, COMSOL, Mach3 Mill, Mach3 Turn, SolidWorks, VisualMill, CleWin
General	Windows, Mac OS, MS Office, LaTeX, Adobe Illustrator, Prezi

Selected projects

M.Sc. Thesis: "Potential applications of microcantilevers in measurement systems" – study and simulation of microcantilever systems

Real-time Systems: Development and testing of real-time application for measuring and dispalying AD voltages for MSP430 microcontroller based on Emboss real-time OS

CNC machining: Construction of the custom CNC milling machine and upgrade of the old watch-makers lathe to CNC lathe machine.

B.Sc. Thesis: "Hardware and software basics of Web sensors" – implementation of temperature Web sensor on MSP430 EasyWeb development board

VLSI Systems Design: Design and implementation of PWM modulation on FPGA Xilinx Spartan-3E development board

Embedded Systems: System solution for acquisition and control hardware, as well as protocols and data format in petrochemical industry

Languages

Serbian – Native, **English** – Full professional proficiency (learned for 12 years),
French – A1, **Spanish** – A1, **Russian** – A1, **German** – introductory course

Scholarships and awards

- City of Belgrade:
  - For success in high school competitions (03/04)
  - As one of 100 best Belgrade students of University of Belgrade (06/07, 07/08)
- Ministry of Education (05/06, 06/07, 07/08, 08/09) for success in studies
- YU Point d.o.o Company (06/07, 07/08, 08/09) for success in studies

Highschool physics national competitions: several prizes on republic and national level

Certificates

PLLs: Advanced techniques, June 24-28, 2013
Swiss Federal Institute of Technology, EPFL, Lausane, Switzerland

Electromagnetic Compatibility of Integrated Circuits, November 18, 2014
Swiss Foundation for Reserach in Microtechnology, EPFL, Lausanne, Switzerland

Interests

Gadgets, applications and technology, skiing, singing, travelling

Personal information

Serbian nationality, married, 30 years old